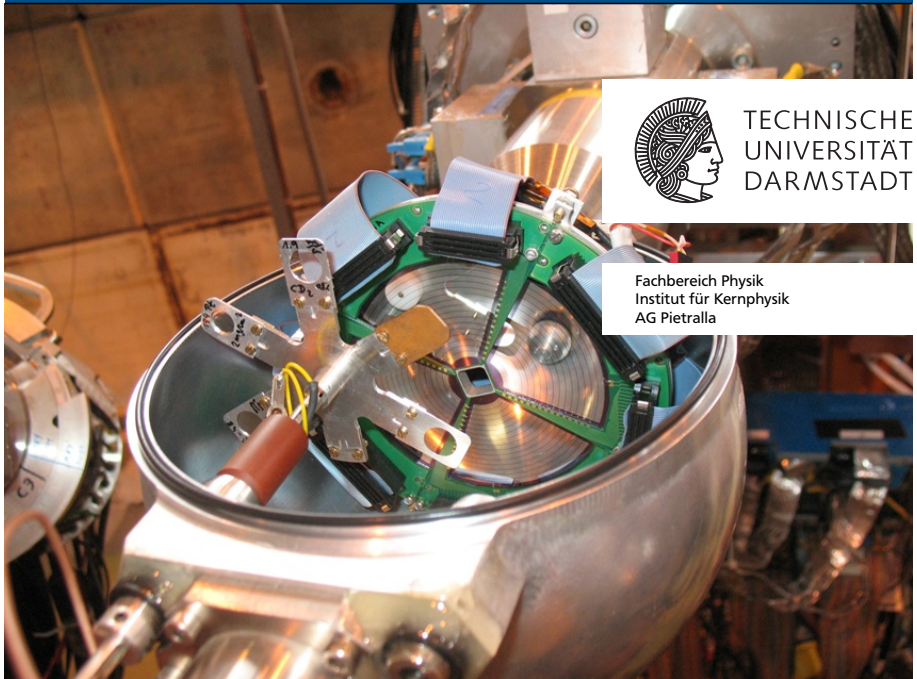


Level lifetimes and quadrupole moments from projectile Coulomb excitation of $A \approx 130$ nuclei

Lebensdauern und Quadrupolmomente in der Kernmassenregion $A \approx 130$ aus Projektil-Coulombanregung

Zur Erlangung des Grades eines Doktors der Naturwissenschaften (Dr. rer. nat.) genehmigte Dissertation von Christopher Bauer aus Hanau
Juni 2013 — Darmstadt — D 17



TECHNISCHE
UNIVERSITÄT
DARMSTADT

Fachbereich Physik
Institut für Kernphysik
AG Pietralla

supported by HIC4FAIR and the BMBF

Level lifetimes and quadrupole moments from projectile Coulomb excitation of $A \approx 130$ nuclei

Lebensdauern und Quadrupolmomente in der Kernmassenregion $A \approx 130$ aus Projektil-Coulombanregung

Genehmigte Dissertation von Christopher Bauer aus Hanau

1. Gutachten: Prof. Dr. Norbert Pietralla

2. Gutachten: Prof. Dr. Thorsten Kröll

Tag der Einreichung: 17. Mai 2013

Tag der Prüfung: 17. Juni 2013

Darmstadt – D 17



Für Anita





Abstract

The chain of experimentally accessible Barium isotopes represents a broad field regarding the evolution of nuclear quadrupole collectivity from the shell closure at $N=82$ towards and even beyond spherical-to-deformed shape transitions. Several isotopes ranging from stable $^{130,132}\text{Ba}$ towards radioactive $^{140,142}\text{Ba}$ have been studied with the projectile-Coulomb excitation technique including the application of the Doppler-shift attenuation method (DSAM). Thereby lifetimes of quadrupole-collective states of ^{132}Ba and ^{140}Ba could be determined for the first time. Furthermore the static electric quadrupole moments $Q(2_1^+)$ for $^{130,132}\text{Ba}$ and $^{140,142}\text{Ba}$ were determined. The results are compared to Monte Carlo Shell Model and Beyond-Mean-Field calculations.

Another interesting feature in this mass region is the effect of shell stabilization in the $N=80$ isotones. This is further investigated by a measurement of the $B(E2; 2_1^+ \rightarrow 0_1^+)$ values of ^{140}Nd and ^{142}Sm .

Zusammenfassung

Die Kette der Barium Isotope zeigt um den Schalenabschluss bei $N=82$ ein interessantes Verhalten hinsichtlich der Entwicklung von Quadrupol-Kollektivität, insbesondere bezüglich des Übergangs von sphärischer zu deformierter Gestalt des Kerns. Angefangen bei den stabilen Kernen $^{130,132}\text{Ba}$ bis hin zu den radioaktiven Isotopen $^{140,142}\text{Ba}$ wurden Messungen mit Hilfe von Projektil-Coulomb-Anregung durchgeführt und die DSA-Methode angewendet. Somit konnten Lebensdauern von quadrupol-kollektiven Zuständen in ^{132}Ba und ^{140}Ba zum ersten Mal bestimmt werden, ebenso wie elektrische Quadrupolmomente $Q(2_1^+)$ in $^{130,132}\text{Ba}$ und $^{140,142}\text{Ba}$. Die Ergebnisse werden mit Monte-Carlo Schalenmodell und Beyond-Mean-Field Rechnungen verglichen.

Ein anderes interessantes Phänomen in dieser Massenregion ist die Ausprägung des $Z=58$ Unterschalenabschlusses in den $N=80$ Isotonen. Diesbezüglich wurden die $B(E2; 2_1^+ \rightarrow 0_1^+)$ Stärken von ^{140}Nd und ^{142}Sm gemessen.



Contents

1. Introduction and motivation	7
2. Nuclear deformations	11
2.1. General aspects	12
2.2. The geometrical model	16
3. Distinct nuclear structure models	19
3.1. The shell model	20
3.1.1. Monte Carlo shell model	24
3.2. Quasiparticle-phonon model	28
3.3. Energy density functionals	31
4. Coulomb excitation theory	33
4.1. Semi-classical description	34
4.2. Connection to observables	37
4.3. Angular distribution of γ -radiation	42
4.4. Coulomb excitation codes: CLX and GOSIA	45
4.5. The DSA principle	49
5. Experimental setups	53
5.1. ATLAS & Gammasphere	54
5.1.1. Accelerator system and beam production	54
5.1.2. Spectrometer and target chamber	54
5.2. REX-ISOLDE & MINIBALL	58
5.2.1. Radioactive isotope production	58
5.2.2. Post-acceleration	60
5.2.3. Gamma spectroscopy	63
5.3. Conducted experiments	66
6. Data analysis and results	69
6.1. Kinematics and Doppler correction	70
6.2. Efficiency calibration	74
6.3. Software APCAD	77



6.4. Stable isotopes $^{130,132}\text{Ba}$	79
6.4.1. DSAM measurement of ^{130}Ba	82
6.4.2. Reorientation technique	85
6.5. Radioactive isotopes $^{140,142}\text{Ba}$	93
6.5.1. DSAM measurement of ^{140}Ba	93
6.5.2. Reorientation technique	95
6.6. Radioactive N=80 isotones $^{140}\text{Nd}, ^{142}\text{Sm}$	103
6.6.1. ^{140}Nd	103
6.6.2. ^{142}Sm	108
7. Discussion	111
7.1. Shape transitions in the Barium isotopic chain	112
7.2. Shell stabilization in the N=80 isotones	119
A. CLX input file	125
B. Gosia input file	127
C. C++ program for calculating correlated errors with Gosia2	131
D. Formalism of electromagnetic transitions strengths	135
Bibliography	137
List of publications	147
List of symbols	149
Acronyms	151
List of figures	153
List of tables	155
Acknowledgments	157
Lebenslauf	159

1 Introduction and motivation

The chart of the nuclides (see fig. 1.1) served as a playground for nuclear structure physics from the beginning of the field in the 1930s [Hei32a; Hei32b; Hei33; Fer34; YUK35] to this day. In order to understand the interplay of the strong interaction between nucleons (protons and neutrons) in the nucleus, scientists started to measure observables such as energies and transition strengths of excited nuclear states [BB30] and their electric and magnetic moments. With a growing number of nuclear models, each describing different phenomena sometimes even in the same nucleus, the necessity of experimental data covering the whole playground became obvious. Just with the possibility to compare different models systematically in chains of isotopes or isotones, *e.g.*, one is able to judge about the quality of those models. These comparisons are requirements on the route towards a universal the-

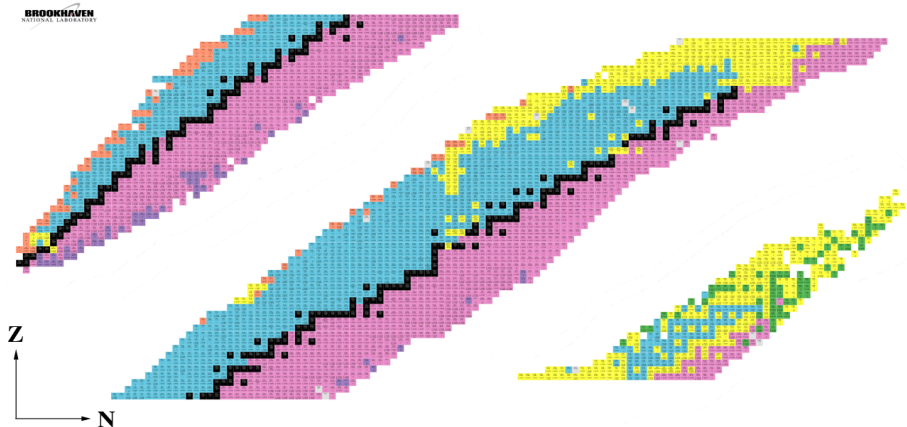


Figure 1.1.: The nuclear landscape as it is known today stretches up to nuclei with proton number $Z=118$ (element not yet named) and neutron number $N=177$.

oretical model that is able to explain the behavior of all nuclei in a consistent way so that we finally understand, *was die Welt im Innersten zusammenhält*¹.

The advent of radioactive ion beam (RIB) facilities (with an intensity and energy suitable to study nuclear reactions) in 1989 in Louvain-La-Neuve [Dar90] and 1990 at the GSI in Darmstadt [Mün90] started the extension of the systematics of many observables towards the unstable neutron- and very proton-rich parts of the chart. Thereby also many improvements regarding the theoretical description of nuclei have been triggered. The experimentalists had and have to develop new methods to meet the requirements of experiments with unstable nuclei but also traditional techniques, such as Coulomb excitation, can be used.

This work presents recent measurements of transition strengths and quadrupole moments in the chain of Barium isotopes ($Z=56$) as well as the $N=80$ isotones by exploiting the experimental possibilities of Coulomb excitation with stable and, in particular, unstable beams. The evolution of nuclear *quadrupole collectivity* from the shell closure at $N=82$ towards and even beyond spherical-to-deformed shape transitions is investigated in the Barium isotopes. The measured quadrupole moments $Q(2_1^+)$, in comparison with the Monte Carlo Shell Model (see subsec. 3.1.1) predictions, lead to a better understanding of the change of shape in those isotopes when adding or removing neutrons to or from the spherical, semi-magic nucleus ^{138}Ba . The shape of a certain nucleus, also in an excited state, remains one of the big questions in nuclear structure physics. The effect of *shell stabilization* [Rai06] is of major interest in the $N=80$ isotones. Is the subshell structure of the shell model (see sec. 3.1) still visible for nuclei of mass $A\approx 140$? For the filled $\pi(1g_{7/2})$ orbital at $Z=58$ this is investigated by the presented measurements of transition strengths in ^{140}Nd and ^{142}Sm . Two theoretical models, namely the shell model and the quasiparticle-phonon model (see sec. 3.2) serve as reference points.

¹ Johann Wolfgang von Goethe, Faust (I. Teil)

136Ba 3.8 s	137Ba 11 s	138Ba 12.1 s	139Ba 17.9 s	140Ba 1.51 s	141Ba 40.7 s	142Ba 2.34 s	143Ba 2.59 M	144Ba 10.2 s	145Ba 5.93 D	146Ba 4.61 D	147Ba 24.1 D	148Ba 54.5 D	149Ba 93.1 D	150Ba 36.9 Y
ε:100.00%	ε:100.00%	ε:100.00%	ε:100.00%	ε:100.00%	ε:100.00%	ε:100.00%	ε:100.00%	ε:100.00%	ε:100.00%	ε:100.00%	ε:100.00%	ε:100.00%	ε:100.00%	ε:100.00%
135Sm 10.3 s	136Sm 47 s	137Sm 45 s	138Sm 5.1 M	139Sm 2.57 M	140Sm 14.62 M	141Sm 10.2 M	142Sm 72.49 M	143Sm 8.75 M	144Sm STABLE 9.07%	145Sm 340 D	146Sm 10.3E+7 Y	147Sm 1.06E+11 Y	148Sm 7E+15 Y	149Sm STABLE 13.82%
ε:100.00%	ε:100.00%	ε:100.00%	ε:100.00%	ε:100.00%	ε:100.00%	ε:100.00%	ε:100.00%	ε:100.00%	ε:100.00%	ε:100.00%	ε:100.00%	ε:100.00%	ε:100.00%	ε:100.00%
134Pm 4.5 s	135Pm 49 s	136Pm 107 s	137Pm 2.4 M	138Pm 10 s	139Pm 4.15 M	140Pm 9.2 s	141Pm 20.90 M	142Pm 40.5 s	143Pm 295 D	144Pm 363 D	145Pm 17.7 Y	146Pm 5.53 Y	147Pm 2.92E4 Y	148Pm 5.38E D
ε:100.00%	ε:100.00%	ε:100.00%	ε:100.00%	ε:100.00%	ε:100.00%	ε:100.00%	ε:100.00%	ε:100.00%	ε:100.00%	ε:100.00%	ε:3E-07%	ε:6E.00%	β:-100.00%	β:-100.00%
133Nd 70 s	134Nd 8.5 M	135Nd 12.4 M	136Nd 50.65 M	137Nd 36.5 M	138Nd 5.04 H	139Nd 29.7 M	140Nd 3.37 D	141Nd 2.49 H	142Nd STABLE 27.2%	143Nd STABLE 12.2%	144Nd 2.29E+15 Y 23.8%	145Nd STABLE 8.2%	146Nd STABLE 17.2%	147Nd 10.9E D
ε:100.00%	ε:100.00%	ε:100.00%	ε:100.00%	ε:100.00%	ε:100.00%	ε:100.00%	ε:100.00%	ε:100.00%	ε:100.00%	ε:100.00%	ε:100.00%	ε:100.00%	ε:100.00%	β:-100.00%
132Pr 1.6 M	133Pr 6.5 M	134Pr 17 M	135Pr 24 M	136Pr 13.1 M	137Pr 1.28 H	138Pr 1.45 M	139Pr 4.41 H	140Pr 3.39 M	141Pr STABLE 100%	142Pr 19.12 H	143Pr 13.57 D	144Pr 17.28 M	145Pr 5.9E4 H	146Pr 24.15 M
ε:100.00%	ε:100.00%	ε:100.00%	ε:100.00%	ε:100.00%	ε:100.00%	ε:100.00%	ε:100.00%	ε:100.00%	ε:100.00%	β:-99.98%	β:-100.00%	β:-100.00%	β:-100.00%	β:-100.00%
131Ce 10.3 M	132Ce 3.51 H	133Ce 97 M	134Ce 3.16 D	135Ce 17.7 H	136Ce >0.7E+14 Y 0.16%	137Ce 9.0 H	138Ce >0.9E+14 Y 0.251%	139Ce 137.641 D	140Ce STABLE 86.453%	141Ce 32.50E D	142Ce >2.6E+17 Y 11.14%	143Ce 93.039 H	144Ce 284.91 D	145Ce 3.01 M
ε:100.00%	ε:100.00%	ε:100.00%	ε:100.00%	ε:100.00%	ε:100.00%	ε:100.00%	ε:100.00%	ε:100.00%	ε:100.00%	β:-100.00%	β:-100.00%	β:-100.00%	β:-100.00%	β:-100.00%
130La 8.7 M	131La 59 M	132La 4.8 H	133La 9.912 H	134La 6.45 M	135La 19.5 H	136La 9.67 M	137La 6E+4 Y	138La 1.02E+11 Y 0.09%	139La STABLE 99.910%	140La 1.67E55 D	141La 3.92 H	142La 91.1 M	143La 14.2 M	144La 40.8 s
ε:100.00%	ε:100.00%	ε:100.00%	ε:100.00%	ε:100.00%	ε:100.00%	ε:100.00%	ε:100.00%	ε:100.00%	ε:100.00%	β:-100.00%	β:-100.00%	β:-100.00%	β:-100.00%	β:-100.00%
129Ba 2.23 H	130Ba 3.3E+14 Y 0.106%	131Ba 11.50 D	132Ba 9.0E+21 Y 0.101%	133Ba 3841 D	134Ba STABLE 2.417%	135Ba STABLE 6.592%	136Ba STABLE 7.854%	137Ba STABLE 11.232%	138Ba STABLE 71.698%	139Ba 93.06 M	140Ba 12.7E27 D	141Ba 19.27 M	142Ba 10.6 M	143Ba 14.5 s
ε:100.00%	ε:100.00%	ε:100.00%	ε:100.00%	ε:100.00%	ε:100.00%	ε:100.00%	ε:100.00%	ε:100.00%	ε:100.00%	β:-100.00%	β:-100.00%	β:-100.00%	β:-100.00%	β:-100.00%
128Ce 3.6E M	129Ce 32.0E H	130Ce 29.21 M	131Ce 9.689 D	132Ce 6.480 D	133Ce STABLE 100%	134Ce 2.0E52 Y	135Ce 2.3E+6 Y	136Ce 13.04 D	137Ce 30.0E Y	138Ce 33.41 M	139Ce 9.27 M	140Ce 63.7 s	141Ce 24.84 s	142Ce 1.984 s
ε:100.00%	ε:100.00%	ε:98.40%	ε:100.00%	ε:98.15%	ε:100.00%	β:-100.00%	β:-100.00%	β:-100.00%	β:-100.00%	β:-100.00%	β:-100.00%	β:-100.00%	β:-100.00%	β:-100.00%

Figure 1.2.: The chart of the nuclides around the nuclei investigated in this work: ^{140}Nd and ^{142}Sm in the $N=80$ isotones, $^{130,132,140,142}\text{Ba}$ in the $Z=56$ chain.



2 Nuclear deformations

In this first theoretical chapter the general aspects of nuclear deformation shall be discussed and the basic variables will be introduced. Furthermore the generally acknowledged geometrical or collective model of nuclei with the description of vibrational and rotational motion is presented.

2.1 General aspects

In a simple description of the nucleus one would consider a homogeneous distribution of nucleons (protons and neutrons) and no preferred direction in space. The nucleus is then spherical, but in order to minimize its potential energy, the shape of the nucleus can deviate and adopt a "new" equilibrium with a deformed shape. For the magic numbers of the shell model (8, 20, 28, 50, 82, 126), see sec. 3.1, the shape of a nucleus is in general spherical. Measurements show that between these numbers most nuclei are deformed. The electrical potential V created by the distribution of charges in the nucleus at a distance R from the origin O (observer) can be expanded in multipoles

$$V(R) \propto \underbrace{\frac{1}{R} \int \rho(r) dr}_{\text{monopole}} + \underbrace{\frac{1}{R^2} \int z \rho(r) dr}_{\text{dipole}} + \underbrace{\frac{1}{R^3} \int (3z^2 - r^2) \rho(r) dr}_{\text{quadrupole}} + \dots \quad (2.1)$$

where r denotes the distance from one point in the nucleus to the origin O and ρ is the charge density. Spherical coordinates are used, while z is the coordinate of the longitudinal axis. The first term corresponds to the total charge of the nucleus. The second and third terms are the dipole and quadrupole terms respectively. Many nuclei are ellipsoidal and therefore have an axial symmetry. In this case the dipole term is zero and the nucleus has a static quadrupole deformation. Of course, there can also be octupole and hexadecapole shapes. Eisenberg and Greiner [EG70] introduced the collective coordinates $a_{\lambda\mu}$, defined by the expansion of the nuclear surface into spherical harmonics

$$R(\theta, \phi) = R_0 \left[1 + \sum_{\lambda=0} \sum_{\mu=-\lambda}^{\lambda} a_{\lambda\mu} Y_{\lambda\mu}(\theta, \phi) \right], \quad (2.2)$$

where R_0 is the radius of the spherical nucleus at the same volume. The charge distribution is usually smeared out at the surface of the nucleus (diffuseness) and therefore R_0 is defined as the mean radius of this diffuse range. The multipole order is given by λ in the following way:

- $\lambda = 0$: volume variations, *e.g.*, breathing modes
- $\lambda = 1$: trivial translation of the nucleus, usually excluded
- $\lambda = 2$: quadrupole deformation (first one of interest)
- $\lambda = 3$: octupole deformation (associated with 3^- states)

The size of the deformation can be defined in terms of the parameter β_λ :

$$\beta_\lambda^2 = \sum_{\mu} a_{\lambda\mu}^2 \quad (2.3)$$

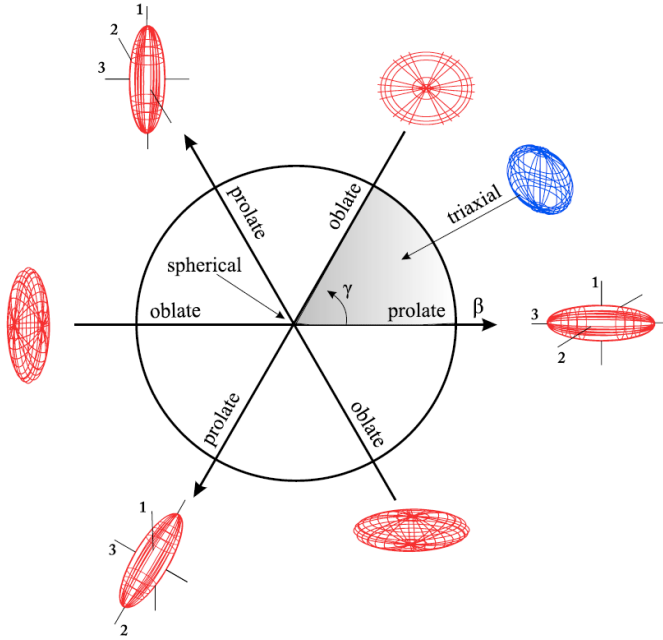


Figure 2.1.: Nuclear deformation from prolate to oblate in the (β, γ) plane using the Lund convention. The shaded area is sufficient to describe the possible deformations as explained in the text.

For the restriction of $\lambda = 2$ and transforming from the laboratory frame to the intrinsic frame of the nucleus, the five $a_{\lambda=2,\mu}$ parameters are reduced to two real parameters $a_{2,0}$ and $a_{2,2} = a_{2,-2}$ while $a_{2,1} = a_{2,-1} = 0$. It is convenient to change the notation here [BM69] and write

$$a_{2,0} = \beta \cos \gamma \quad (2.4)$$

$$a_{2,2} = a_{2,-2} = \frac{1}{\sqrt{2}} \beta \sin \gamma \quad (2.5)$$

to specify the nuclear shape in terms of β and γ . The parameter β represents the extent of the quadrupole deformation and is equivalent with the general definition of eq. 2.3 for $\lambda = 2$:

$$\beta_2^2 = \sum_{\mu} a_{2,\mu}^2 = \beta^2 \cos^2 \gamma + 2 \cdot \frac{1}{2} \beta^2 \sin^2 \gamma = \beta^2 \quad (2.6)$$

The second parameter γ denotes the degree of axial asymmetry. Most nuclei are axially symmetric, or close to it, at least in their ground states. For an axially symmetric nucleus, the potential has a minimum at $\gamma = 0^\circ$. A common convention (Lund convention) for the ranges of β and γ variables is that $\beta > 0, \gamma = 0^\circ$ for an axially symmetric prolate nucleus (American football, cigar) and that $\beta > 0, \gamma = 60^\circ$ gives an axially symmetric oblate nucleus (disc). If γ is not a multiple of 60° the nucleus is triaxial, what means no axial symmetry at all. The different configurations are shown in fig. 2.1. An alternate convention would be $\beta > 0$ for prolate and $\beta < 0$ for oblate deformation and $\gamma \in [0^\circ, 30^\circ]$.

When one tries to measure the deformation experimentally the two important quantities to describe a quadrupole-deformed nucleus are the moment of inertia J and the quadrupole moment of the ellipsoidal shape. Both can be written in terms of β for axially symmetric nuclei. For an ellipsoid, the so-called rigid body moment of inertia is

$$J_{sph} = \int \rho_{mat}(r) r_{\perp}^2 dV = \frac{2}{5} M R^2. \quad (2.7)$$

Integrating the radius over the nuclear surface gives to first order in β

$$J = \frac{2}{5} A M R_0^2 (1 + 0.31\beta). \quad (2.8)$$

The electric multipole operators $Q_{\lambda\nu}$ are defined as [EG70]

$$Q_{\lambda\nu} = \sum_{k=1}^Z r_k^{\lambda} Y_{\lambda\nu}(\theta, \phi), \quad (2.9)$$

where the sum goes over all protons in the nucleus, because they carry the charge. The electric quadrupole moment Q of a nucleus in the state ψ_{jM} is then defined as the expectation value Q_{20} in the nuclear state $|jM\rangle = |jj\rangle$ up to a conventional factor $\sqrt{\frac{16}{5}}\pi$:

$$Q = \sqrt{\frac{16}{5}}\pi \langle \psi_{jj} | Q_{20} | \psi_{jj} \rangle = \sqrt{\frac{16}{5}}\pi \int \psi_{jj}^* Q_{20} \psi_{jj} dx \quad (2.10)$$

The *intrinsic quadrupole moment* is a measure for the deviation of the nuclear density from spherical symmetry. One can estimate the number of particles contributing by considering the beforehand described model of a uniformly charged spheroid

in spherical coordinates through the radius $R = R_0(1 + \beta Y_{20})$ for no triaxial deformation. One obtains [EG70; Cas00]

$$Q_0 = \sqrt{\frac{16}{5}} \pi \frac{3Z}{4\pi R_0^3} \int Y_{20}^* \left(\int_0^R r^4 dr \right) d\Omega \quad (2.11)$$

$$= \sqrt{\frac{16}{5}} \pi \frac{3Z}{4\pi R_0^3} \int \frac{1}{5} R_0^5 (1 + \beta Y_{20})^5 Y_{20}^* d\Omega \quad (2.12)$$

$$\approx \frac{3}{\sqrt{5}\pi} R_0^2 Z \beta (1 + 0.16\beta). \quad (2.13)$$

The last line is derived using the common normalization conditions of the spherical harmonics and the given accuracy is of second order in β .

The collective rotational model defines the following connection between the matrix elements for an $E2$ transition and the intrinsic quadrupole moment Q_0 :

$$M_{if} = \langle I_f || E2 || I_i \rangle = \sqrt{2I_i + 1} \begin{pmatrix} I_i & 2 & I_f \\ K & 0 & K \end{pmatrix} \sqrt{\frac{5}{16\pi}} Q_0 = M_{fi} \quad (2.14)$$

$$Q = Q_0 \frac{3K^2 - I(I+1)}{(I+1)(2I+3)} \quad (2.15)$$

Here Q is the *spectroscopic quadrupole moment* that can be observed in experiments only (see sec. 4.2). If one calculates Q_0 from a measured experimental or theoretical transition strength or lifetime it is often referred to Q_0 as the "transitional" quadrupole moment, which is model-dependent.

2.2 The geometrical model

The observation of several general properties for all nuclei, such as a low-lying 2_1^+ state for even-even nuclei, led to the development of the *geometrical* or *collective model* [KH87] by Bohr and Mottelson [BM69]. The origin of those collective properties lies in the nuclear collective motion, in which many nucleons contribute coherently to the nuclear properties. *Vibrations* and *rotations* are the two major types of collective nuclear motion considered in this model, often also called "liquid drop" model because the description of such a system can be done with a similar mathematical analysis.

Vibrations

The vibration of a nucleus can be expressed by the same parametrization of the radius as in eq. 2.2 for a shape deformation. However, in the case of a vibration it is not static anymore. In the vibrational model the $\lambda = 2$ excitation is seen as one (quadrupole) phonon carrying 2 units of angular momentum \hbar . This leads to the first excited 2^+ state when adding a quadrupole phonon to the 0^+ ground state of an even-even nucleus. A 2-phonon coupling creates a triplet consisting of a 0^+ , 2^+ and 4^+ state while a 3-phonon excitation results in a quintuplet with the angular momenta 0^+ , 2^+ , 3^+ , 4^+ and 6^+ [Cas00]. The pure harmonic vibrational model predicts equal energy gaps between the multiplets, see fig. 2.2. Therefore the ratio $R_{4/2} = E(4_1^+)/E(2_1^+) = 2.0$ is a signature for vibrational nuclei while in reality this ratio is typically $2.0 \dots 2.5$. Those so-called "vibrators" are located near closed shells in the nuclide chart. In the IBM framework [IA06] this class of nuclei can be described within the $U(5)$ dynamical symmetry.

Rotations

The second type of collective motion, the rotational motion, can be observed only in nuclei with non-spherical equilibrium shapes, often called *deformed nuclei*. They are typically found in the mass ranges $150 < A < 190$ and $A > 220$ (rare-earth elements and actinides). Then the nucleus is seen as an axially symmetric rigid rotating system along an axis perpendicular to the symmetry axis. The rotational energy of such a system with angular momentum quantum number I is defined as

$$E(I) = \frac{\hbar^2}{2J} I(I + 1). \quad (2.16)$$

Here J denotes the moment of inertia and only even nuclear spins I are allowed in the ground state band. By increasing the quantum number I stepwise more and

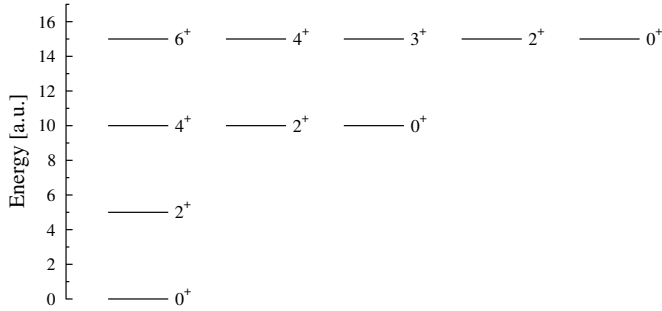


Figure 2.2.: The schematic vibrational level scheme with 1 up to 3 Q-phonon excitations is shown. The energy is given in arbitrary units.

more rotational energy is added to the nucleus. It is rotating faster in the classical picture. Considering the energy sequence a *rotational band* is built with

$$\begin{aligned}
 E(2^+) &= \frac{6\hbar}{2J} \\
 E(4^+) &= \frac{20\hbar}{2J} \\
 E(6^+) &= \frac{42\hbar}{2J} \\
 E(8^+) &= \dots
 \end{aligned}
 \tag{2.17}$$

The $R_{4/2}$ ratio serves again as a fingerprint for this collective motion giving $R_{4/2} = E(4_1^+)/E(2_1^+) = 3.33$ for the so-called "(rigid) rotors" as can be seen in fig. 2.3. In the IBM framework [IA06] they correspond to the $SU(3)$ dynamical symmetry. At high angular momentum I the effect of "centrifugal stretching" [KH87, sec. 11.13] can be observed in experiments by an increase of the moment of inertia. It shows that also the *rigid rotor* is a simplified picture and real nuclei cannot be considered to be completely rigid. Generally there are fluctuations of the quadrupole deformation of nuclei. Here the hybrid confined β -soft (CBS) rotor model [PG04] comes with a more realistic approach. It uses the infinite square-well potential over a confined range of values for the quadrupole deformation parameter β . An analytical solution of the Bohr-Hamiltonian eigenvalue problem exists for this case and interpolates between the phase-transitional point and the rigid-rotor limit, and thereby

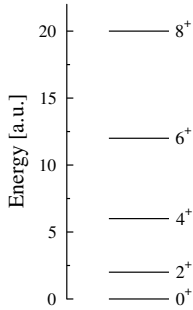


Figure 2.3.: The schematic rotational level scheme up to $I = 8$ is shown. The energy is given in arbitrary units.

accounts well for energies and E2 rates observed in such nuclei [PG04]. The introduced infinite square-well potential $u(\beta)$ with boundaries $0 \leq \beta_m < \beta_M$ allows for $\beta_m \neq 0$, outside the usual ansatz. The ratio $r_\beta = \beta_m/\beta_M$ parametrizes the stiffness of the potential and hence the structural evolution from the transitional point ($r_\beta=0$, large fluctuations in β) to the rigid rotor ($r_\beta \rightarrow 1$, no fluctuations in β).

Beside the aforementioned interacting boson model (IBM) [IA06] the particle-hole (ph) random-phase approximation (RPA) and its quasiparticle (qp) version (QRPA) are perhaps the most widely adopted microscopic approaches to collective motion in nuclei [Row10; RS05]. A microscopic extension of the QRPA treating a separable Hamiltonian in a multiphonon basis is the quasiparticle-phonon model (QPM) [Iud12]. The basics of this approach are covered in sec. 3.2 while experimental results are compared to the QPM in sec. 7.2.

3 Distinct nuclear structure models

Various theoretical models have been established to calculate properties of nuclei all over the nuclear landscape (see fig. 1.1). *Ab-initio models* like the No-core Shell Model, Quantum Monte Carlo or Coupled Cluster have limited capabilities to calculate properties of very light nuclei up to $A \approx 10-12$. For larger numbers of A the system becomes too complex, calculations are mainly limited by the available computational power. With *configuration interaction* (interacting shell model) one can cover a larger range of nuclei from roughly $A=10$ to $A=100$ or more, depending on the number of valence protons or neutrons outside closed shells. The original nuclear **shell model** will be explained in sec. 3.1 as well as its powerful expansion, the **Monte Carlo Shell Model**.

With the **quasiparticle-phonon model** another microscopic model is presented in sec. 3.2 but it is also limited to nuclei which are not too far away from closed shells. Using **energy density functionals** (sec. 3.3) and self-consistent mean fields it is possible to calculate properties over the entire chart without any limitation on the size of nuclei.

The three specific models explained in this chapter are just a selection of available theories and not meant to be representative. They have been chosen because they are suited to compare some of their theoretical predictions to the extracted experimental observables in this work.

3.1 The shell model

The first observation that led to the development of the shell model was the fact that when adding protons or neutrons to a nucleus, there are certain points where the binding energy of the next nucleon is significantly less than the last one. One found certain magic numbers of nucleons (2, 8, 20, 28, 50, 82, 126) which are more tightly bound than the next higher number. With more and more observables, e.g., excitation energies $E(2_1^+)$, accessible for more and more nuclei, also the evidence for the significance of these numbers was growing. In this work certain systematics of transitions strengths $B(E2; 2_1^+ \rightarrow 0_1^+)$ and quadrupole moments $Q(2_1^+)$ are investigated to draw conclusions about the shell and subshell structure in the mass region $A \approx 130$.

In 1949 M. Göppert-Mayer and J.H.D. Jensen introduced a successful microscopic description of the atomic nucleus [MJ55]. They modified the known atomic shell model to be able to describe the atomic nucleus as well. The main difference between both types of shell models is the underlying fundamental interaction. The atomic shell model is based on the *Coulomb interaction* between the positively charged protons of the atomic nucleus and the negatively charged electrons, which acts as a central-force. The Coulomb interaction plays only a minor role in nuclear physics. Here, the dominant interaction is the *strong interaction* between the nucleons.

The framework of the independent particle model is the basis for the multiparticle shell model, which then provides the standard for other models and builds the microscopic basis for further macroscopic, collective models [Cas00, ch. 3]. In that terminology the nucleus is described in terms of noninteracting particles in the orbits of a spherically symmetric potential $U(r)$, which is itself generated by all the nucleons. The concept of a central potential arises from the interaction between nucleons and can be derived for simplicity (as a very good approximation) from the Hamiltonian of a 2-body interaction:

$$H = T + V = \sum_{i=1}^A \frac{\vec{p}_i^2}{2m_i} + \sum_{i>k=1}^A V_{ik}(\vec{r}_i - \vec{r}_k) \quad (3.1)$$

The interaction V has the form of a nucleon-nucleon potential with a repulsive core and a strongly attractive part extending over the range where the nuclear force acts. To achieve the transformation from a *nucleon-nucleon* interaction to a common *nuclear* potential a 1-body potential $U_i(\vec{r})$ is added and subtracted:

$$H = \sum_{i=1}^A \left[\frac{\vec{p}_i^2}{2m_i} + U_i(\vec{r}) \right] + \left[\sum_{i>k=1}^A V_{ik}(\vec{r}_i - \vec{r}_k) - \sum_{i=1}^A U_i(\vec{r}) \right] \equiv H_0 + H_{residual} \quad (3.2)$$

The complex goal is then to determine an appropriate central mean field potential V for this separation in such a way that H_0 describes the independent motion of the A nucleons in the central potential, which is created by the nucleons themselves, and $H_{residual}$ is the so-called residual interaction between the nucleons, that can be treated as a small perturbation on the Hamiltonian H_0 .

The harmonic oscillator potential is an appropriate choice due to the attractive and short-ranged nature of the strong interaction, although it has the wrong asymptotic behavior. Furthermore it is particularly easy to handle mathematically and given simply by

$$V(r) = \frac{1}{2}kr^2 = \frac{1}{2}m\omega^2r^2 \quad (3.3)$$

where k is the spring constant of the classical analogon. For a 3-dimensional harmonic oscillator, the eigenvalues E_{nl} can be written as $E_{nl} = (2n + l + 1/2)\hbar\omega$ where $n = 1, 2, 3, \dots$ is the radial quantum number and the orbital angular momentum equals $l = 0, 1, 2, 3, \dots$ (s,p,d,f,...) producing degenerate energies when $\Delta l = -2\Delta n$ as shown on the left of fig. 3.1. The typical number of oscillator quanta is given by $N = 2(n - 1) + l$.

The big achievement of Mayer and Jensen was, in fact, to introduce a simple modification to the harmonic oscillator potential to reproduce the empirically found *magic numbers* for protons and neutrons at $N, Z = 2, 8, 20, 28, 50, 82, 126$. This modification can be subdivided in an orbital \vec{l}^2 term and a spin-orbit term $\vec{l} \cdot \vec{s}$. The orbital term splits the degeneracy of the harmonic oscillator levels and lowers them with larger l :

$$V_{l^2} = -V_l \vec{l}^2 \quad (3.4)$$

The spin-orbit term stems from the fact that the nucleon has an intrinsic spin $s = \frac{1}{2}\hbar$ resulting in a total angular momentum $\vec{j} = \vec{l} + \vec{s}$ of a nucleon in an orbit l that has an absolute value of $l \pm 1/2$. The form of the spin-orbit potential is taken as

$$V_{l \cdot s} = -V_{ls} \vec{l} \cdot \vec{s} \quad (3.5)$$

in such a way that orbitals with $j = l + 1/2$ are lowered and orbitals with $j = l - 1/2$ are raised in energy compared to the degenerate level after the \vec{l}^2 correction. The basic potential for the original shell model then writes the following:

$$V(r) = \frac{1}{2}m\omega^2r^2 - V_l \vec{l}^2 - V_{ls} \vec{l} \cdot \vec{s} \quad (3.6)$$

The evolution of this scheme with the two subsequent corrections to the harmonic oscillator levels is illustrated in fig. 3.1. The correct gaps corresponding to the magic numbers are clearly visible on the right side of the picture.

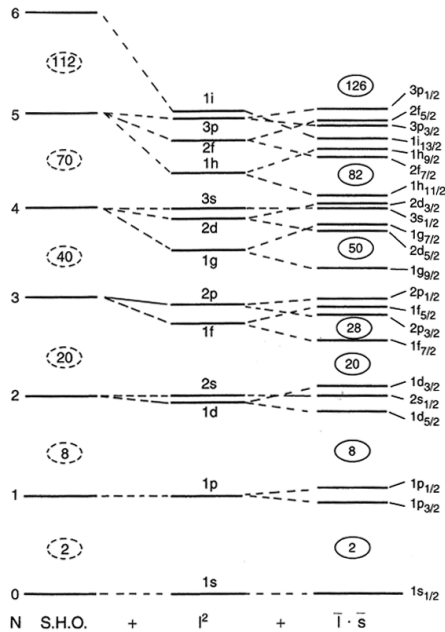


Figure 3.1.: The nuclear shell model can be derived from a simple harmonic oscillator (S.H.O.) by modifying it with a l^2 term and spin-orbit coupling $\vec{l} \cdot \vec{s}$ [Cas00].

There is also an important connection to the parity quantum number π that becomes visible in this picture. The parity of a certain orbit is defined as

$$\pi_{nlm} = (-1)^l \quad (3.7)$$

and the $2n + l$ degeneracy of the harmonic oscillator potential leads to shells just with levels of the same parity in the beginning. However, at higher shells, the spin-orbit term brings some $j = l + 1/2$ orbits down among the levels of the next lower shell, *e.g.*, in the case of the $1h_{11/2}$ orbit. Those orbits are called *intruder* or *unique parity orbits*. The importance of this intruder orbits becomes even more significant when considering further *residual interactions*. As long as there is just one *valence* nucleon in a shell outside a core with N,Z at magic numbers, the shell model can be applied straightforward. As soon as there is more than one valence nucleon the residual interactions between these nucleons have to be considered. Therefore shell model calculations become soon complex when moving away from closed shells and new concepts are necessary. Here, Monte Carlo shell model calculations play a major role in nuclear structure theory and are introduced in the following subsection 3.1.1.

3.1.1 Monte Carlo shell model

The Monte Carlo Shell Model (MCSM) stands for the application of the Quantum Monte Carlo Diagonalization (QMCD) method to the nuclear shell model [HMO95; Ots01a]. It can be considered as a breakthrough in shell-model calculations as it allows to study the structure of low-lying states with realistic interactions for a wide variety of nuclei, even with a large number of valence nucleons outside magic numbers (see sec. 3.1).

The crucial point in the many-body problem of the nuclear shell model is that the dimension of the full valence-nucleon Hilbert space grows rapidly as the particle number increases preventing from performing full model space calculations. The shell-model dimension is the number of Slater determinants, which can be generated in the valence shell. For the study of a many-body quantum system, the simplest and most precise method is the diagonalization of the Hamiltonian. A direct diagonalization of the Hamiltonian matrix can be carried out only for restricted systems because the maximum treatable dimension of the matrix is limited. At dimensions $\geq 10^8$ shell model codes reach their limits [HMO95; Ots01a]. The alternative approach of applying stochastic methods like the QMCD to many-body problems enables to overcome this difficulty. After suitable states are selected as basis states for the many-body system, the Hamiltonian can be diagonalized in a reasonable approximation within a subspace just spanned by such basis states (see fig. 3.2). The number of basis states can be much smaller, enabling practical calculations. The QMCD method of choosing the many-body states was proposed by Honma, Mizusaki and Otsuka first [HMO95] and then improved further as summarized in ref. [Ots01a].

Another, completely different, quantum Monte Carlo approach is the Shell Model Monte Carlo (SMMC) method, a term that can easily lead to confusion with the MCSM. The SMMC is basically restricted to ground-state properties and suffers from the so-called minus-sign problem for realistic interactions [Ots01a]. In contrast, the MCSM describes also excited states, including their energies, wave functions, and transition matrix elements.

Coming back to the QMCD method there are two major steps:

1. All basis states for the given many-body system are generated. The many-body system is comprised of valence protons and neutrons and only basis states important to the eigenstate to be obtained, are selected.
2. Having those selected basis states the matrix elements of the Hamiltonian are calculated and the Hamiltonian matrix is diagonalized. If all important

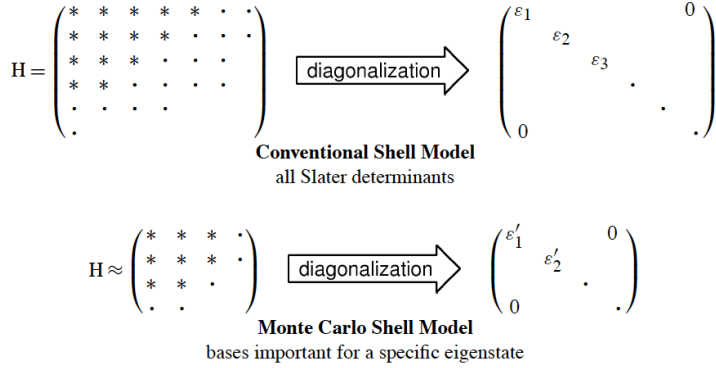


Figure 3.2.: The Hamiltonian matrices in the conventional shell model and in the Monte Carlo shell model. In the conventional shell model one calculates matrix elements of the Hamiltonian for all possible Slater determinants in the valence shell. After the calculation of all matrix elements the matrix needs to be diagonalized. Picture is taken from ref. [Ots01a].

basis states have been included, the result is a good approximation to the exact diagonalization in the entire Hilbert space.

Knowing that the question arises how to generate *important* basis states. Following the detailed explanations of ref. [HMO95] the equation for the generation of basis states is given by

$$|\Phi(\sigma)\rangle \propto e^{-\beta h(\sigma)} |\Psi^{(0)}\rangle, \quad (3.8)$$

where σ represents a set of random numbers to control the basis generation, $|\Phi(\sigma)\rangle$ is a basis state, and $|\Psi^{(0)}\rangle$ the initial state. The one-body Hamiltonian $h(\sigma)$ is a linear combination of various one-body operators with certain weights. Due to the one-body character both $|\Phi(\sigma)\rangle$ and $|\Psi^{(0)}\rangle$ are Slater determinants, just the generally deformed single-particle wave functions constituting the Slater determinants are varied in the operation of eq. 3.8.

Introducing a toy Hamiltonian

$$H = \frac{1}{2} V O^2 \quad (3.9)$$

one can clarify the concept even better. V shall be a coupling constant with $V < 0$ and O just an arbitrary one-body operator. The above-mentioned one-body Hamiltonian would then be given by

$$h(\sigma) = V \sigma O. \quad (3.10)$$

There is just one random variable σ because the toy Hamiltonian of eq. 3.9 consists of one term only. With different values of the random number σ one can generate different state vectors $|\Phi(\sigma)\rangle$ exploiting eq. 3.8. Then the Hamiltonian is diagonalized in a subspace spanned by those basis states. One evaluates each basis' contribution for lowering the energy eigenvalue being calculated. Only those with larger contributions are kept, the *important bases*, while the others are neglected. As an improvement one can generate more states by other values of σ and again only consider the important ones. This means basis states can be added until a certain convergence of the energy eigenvalue is reached. When one has such selected basis vectors, that are important for a specific eigenstate (can be also an excited state), its energy eigenvalue and wave functions are obtained as a result of the diagonalization of a small matrix with respect to these important basis vectors (see lower part of fig. 3.2).

In a realistic case, a general shell-model Hamiltonian can be written as

$$H = \sum_{\alpha=1}^{N_f} (E_{\alpha} O_{\alpha} + \frac{1}{2} V_{\alpha} O_{\alpha}^2) \quad (3.11)$$

with an index α , single-particle energies E_{α} , and interaction strengths V_{α} for one-body operators O_{α} . The one-body Hamiltonian is then given as a combination of terms in analogy to eq. 3.10:

$$h(\sigma) = \sum_{\alpha} (E_{\alpha} + s_{\alpha} V_{\alpha} \sigma_{\alpha}) O_{\alpha} \quad (3.12)$$

Here $s_{\alpha} = \pm 1$ ($\pm i$) if $V_{\alpha} < 0$ (> 0). Again the basis states are generated by using eq. 3.8 in the same way as for the toy Hamiltonian. The adopted basis states are the so-called *QMCD bases* and the number of QMCD bases is referred to as the *QMCD basis dimension*. Energies and wave functions are determined by the diagonalization. The ground state as well as excited states can be obtained by monitoring the energy eigenvalues of excited states in the basis generation process.

The described procedure is the first version of QMCD, that already works quite well for simpler systems [HMO95], but in order to carry out realistic large-scale shell-model calculations it has been improved over the years by three major concepts [Ots01a], that shall be just mentioned here:

- Basis generation around the mean-field solution
- Restoration of angular momentum
- Compression of QMCD basis space

The combination of all improvements builds the present version of the QMCD method and, as mentioned above, its application to the nuclear shell model is called the Monte Carlo shell model. Due to the *importance truncation* of basis vectors the QMCD basis dimension is usually 30-50, even if the original Hilbert space has $> 10^9$ dimensions.

It has been demonstrated by Shimizu, Otsuka and co-workers for the case of the Ba isotopes with $N \geq 82$ that, when changing the number of valence particles, the shape phase transition occurs quite prominently, while the Hamiltonian and the single-particle orbits are kept unchanged [Shi01]. Thus, it provides a first evidence, by means of microscopic calculations beyond mean-field approaches, that the shape-phase transition can occur due to the change of valence particle number with a realistic Hamiltonian and shell structure. The full major shells are taken into account: $50 \leq Z \leq 82$ for protons and $82 \leq N \leq 126$ for neutrons.

In this work results of MCSM calculations for the quadrupole moments $Q(2_1^+)$ are compared to measurements in the Barium isotopes on either side of the magic number at $N=82$ (see sec. 7.1). This means different valence shells are taken into account. The experimental data is interpreted in terms of a shape transition also in the region with $N \leq 82$.

3.2 Quasiparticle-phonon model

The quasiparticle-phonon model (QPM) is a microscopic approach going beyond the quasiparticle random-phase approximation (QRPA) [Row10; RS05] to describe collective motion in nuclei. Within the QPM a Hamiltonian of separable form is treated in a microscopic multiphonon basis. Therefore it is able to describe the anharmonic features of collective modes as well as the multiphonon states. An introduction is given by Solov'ev [Sol92] and a detailed description can be found in the review article by Lo Iudice et al. [Iud12] while the basic principles shall be presented here.

The adopted two-body Hamiltonian is a sum of several separable multipole-multipole potentials. This simplifying assumption allows the QPM to cover a large configuration space and to include up to 3-phonon basis states. The Hamiltonian is of the following form:

$$H = H_{sp} + V_{pair} + V_M^{ph} + V_{SM}^{ph} + V_M^{pp} \quad (3.13)$$

H_{sp} is a one-body Hamiltonian including a Woods-Saxon potential V_{WS} , while V_{pair} represents the monopole pairing. V_M^{ph} and V_{SM}^{ph} are the sums of separable multipole and spin-multipole interactions acting in the particle-hole (ph) channel and V_M^{pp} is the sum of particle-particle (pp) multipole potentials. The exact definitions of the different potentials can be found in ref. [Iud12].

The QPM procedure involves several steps. First the particle-hole operators a_q^\dagger (a_q) are transformed into quasiparticle operators α_q^\dagger (α_q) with the help of the Bogoliubov canonical transformation. This way a quasiparticle separable Hamiltonian is obtained and then adopted to generate QRPA energies ω_λ and the corresponding phonons

$$Q_\lambda^\dagger = \frac{1}{2} \sum_{qq'} \left\{ \psi_{qq'}^\lambda \left[\alpha_q^\dagger \alpha_{q'}^\dagger \right]_\lambda - \varphi_{qq'}^\lambda \left[\alpha_{q'} \alpha_q \right]_{\bar{\lambda}} \right\}. \quad (3.14)$$

The amplitudes $\psi_{qq'}^\lambda$ and $\varphi_{qq'}^\lambda$ fulfill the equations

$$\frac{1}{2} \sum_{qq'} \left[\psi_{qq'}^\lambda \psi_{qq'}^{\lambda'} - \varphi_{qq'}^\lambda \varphi_{qq'}^{\lambda'} \right] = \delta_{\lambda\lambda'}, \quad (3.15)$$

which are obtained from the normalization condition in the quasiboson approximation.

After the generation of the QRPA phonons it is possible to express the quasiparticle separable Hamiltonian into the phonon form:

$$H_{QPM} = \sum_{\lambda} \omega_{\lambda} Q_{\lambda}^{\dagger} Q_{\lambda} + H_{vq} \quad (3.16)$$

The first term is the unperturbed phonon Hamiltonian and H_{vq} is the phonon coupling part. The phonon Hamiltonian is diagonalized in a space spanned by states composed of one, two, and three QRPA phonons. Those yield the eigenfunction of a given spin JM :

$$\begin{aligned} \psi_{vJM} = & \sum_i R_i^{(vJ)} Q_{iJM}^{\dagger} |0\rangle + \sum_{\lambda_1 \lambda_2} P_{\lambda_1 \lambda_2}^{(vJ)} [Q_{\lambda_1}^{\dagger} \otimes Q_{\lambda_2}^{\dagger}]_{JM} |0\rangle \\ & + \sum_{\lambda_1 \lambda_2}^{\lambda_3 I} T_{\lambda_1 \lambda_2 \lambda_3 I}^{(vJ)} [[Q_{\lambda_1}^{\dagger} \otimes Q_{\lambda_2}^{\dagger}]_I \otimes Q_{\lambda_3}^{\dagger}]_{JM} |0\rangle \quad (3.17) \end{aligned}$$

In the following these wave functions are normalized and antisymmetrized exploiting certain commutation relations. More details can be found in ref. [Iud12] and refs. therein.

A crucial step in the QPM is the determination of the Hamiltonian parameters. They are determined, for a Woods-Saxon potential, *e.g.*, and yield single-particle spectra in overall agreement with the data. The single-particle space includes all shells below the Fermi energy as well as all bound states above in order to allow for the investigation of the properties of the excited states over a wider energy range. Furthermore a constant monopole pairing is used. The latter is obtained by a fit to odd-even mass differences. On the other hand the coupling strength parameters of the quadrupole-quadrupole and octupole-octupole particle-hole potential are fixed by a fit to the energies of the first 2^+ and 3^- state, respectively. The strengths of the multipole terms are adjusted in such a way that the energy of the computed lowest two-quasiparticle excitations (states) is left unchanged.

The quadrupole pairing turned out to be the dominant particle-particle interaction for low-energy excitations [Iud12]. In the QPM it is assumed to be equal for protons and neutrons. It plays a crucial role when determining the properties of the low-energy quadrupole modes. The parameters have to be adjusted for each investigated mass region by a comparison to basic experimental data such as the excitation energy of the 2_1^+ state. Then a unique set of parameters can be used throughout the nuclei of a given mass region to calculate the low-lying as well as high-lying spectra.

The selection of phonons to be included in the multiphonon basis (used for diagonalizing the Hamiltonian of eq. 3.13) is dictated by the properties of the states

to be determined. For low-lying positive parity QPM states only phonons of positive parity with multipolarities $\lambda = 1 - 6$ are included. For each multipolarity all phonons up to a given energy are included. Due to the fact that the QPM Hamiltonian mixes the multiphonon components differing by one phonon number, the fragmentation of the two-phonon states is sensitive to the number of one- and three-phonon configurations. To find the minimum dimensions of the multiphonon space to be used in the actual calculations, the number of two-phonon states is increased until it doesn't affect any longer the structure of the wavefunction (eq. 3.17). The onset of this saturation plateau determines the dimension to be used.

In this work experimental data of the $N=80$ isotones, presented in sec. 6.6, is compared to QPM predictions. The used set of QPM parameters was determined for this specific chain of nuclei [LIST08] (see sec. 7.2 for the discussion).

3.3 Energy density functionals

Self-consistent mean-field (SCMF) models for nuclear structure and excitations have shown to be very successful in describing and predicting properties of heavy nuclei [BHR03]. Because nuclear SCMF models are in many respects analogs of density functional theory, one refers to it as well as effective energy density functionals (EDF). In this work state-of-the-art EDF methods based on the Gogny D1S functional [DG80] have been applied to compute the level scheme and reduced transition probabilities of ^{140}Ba . These techniques are very suitable to study the intrinsic quadrupole deformations of a nuclear system (β, γ) because these degrees of freedom are taken into account explicitly in the calculations in a self-consistent manner. For an introduction of the parameters (β, γ) see sec. 2.1.

The method consists of producing first a set of many-body states with different intrinsic quadrupole deformations (β, γ) . The final many-body wave functions that describe the different states of an even-even nucleus with Z number of protons and N number of neutrons are written as [RE10]

$$|IM; NZ\sigma\rangle = \sum_{K\beta\gamma} f_{K\beta\gamma}^{I;NZ,\sigma} |IMK; NZ; \beta\gamma\rangle. \quad (3.18)$$

The levels for a given value of the angular momentum I and M are labeled $\sigma = 1, 2, \dots$ and K are the projections of \vec{I} on the laboratory and intrinsic z axes, respectively. The coefficients $f_{K\beta\gamma}^{I;NZ,\sigma}$ of the linear combination are obtained by minimizing the energy within the nonorthogonal set of wave functions $\{|IMK; NZ; \beta\gamma\rangle\}$. These states are found by using the variation after particle-number projection method (VAP-PN), which is well-suited to include properly pairing correlations in the system. A simultaneous projection of the intrinsic mean-field states $|\phi(\beta, \gamma)\rangle$ onto good particle number and angular momentum is performed:

$$|IMK; NZ; \beta\gamma\rangle = \frac{2I+1}{8\pi^2} \int D_{MK}^{I*}(\Omega) \hat{R}(\Omega) \hat{P}^N \hat{P}^Z |\phi(\beta, \gamma)\rangle d\Omega \quad (3.19)$$

The neutron and proton number projectors are given by $\hat{P}^{N,Z}$, $\hat{R}(\Omega)$ denotes the rotation operator and $D_{MK}^{I*}(\Omega)$ the Wigner matrices in the Euler angles Ω , respectively.

In dealing with effective forces such as Gogny, a natural separation of the interaction into the two-body Hamiltonian \hat{H}_{2b} on the one hand and the density-dependent part $\epsilon_{DD}^{N,Z}[\phi]$ on the other, emerges. Here the Gogny D1S interactions is used and \hat{H}_{2b} corresponds to the kinetic energy plus the spin-orbit, Coulomb, and the finite-range central potentials. The VAP-PN principle provides

$$\delta E^{N,Z}[\bar{\Phi}(\beta, \gamma)]|_{\bar{\Phi}=\Phi} = 0, \quad (3.20)$$

where

$$E^{N,Z}[\Phi] = \frac{\langle \Phi | \hat{H}_{2b} \hat{P}^N \hat{P}^Z | \Phi \rangle}{\langle \Phi | \hat{P}^N \hat{P}^Z | \Phi \rangle} + \epsilon_{DD}^{N,Z}[\Phi] - \lambda_{q_{20}} \langle \Phi | \hat{Q}_{20} | \Phi \rangle - \lambda_{q_{22}} \langle \Phi | \hat{Q}_{22} | \Phi \rangle. \quad (3.21)$$

The minimization is performed under constraints on the quadrupole deformation operators $\hat{Q}_{2\mu}$. Here the Lagrange multipliers $\lambda_{q_{2\mu}}$ ensure that the following conditions are fulfilled in the intrinsic state [RE10]:

$$\lambda_{q_{20}} \rightarrow \langle \Phi | \hat{Q}_{20} | \Phi \rangle = q_{20} \quad (3.22)$$

$$\lambda_{q_{22}} \rightarrow \langle \Phi | \hat{Q}_{22} | \Phi \rangle = q_{22} \quad (3.23)$$

Finally the deformation parameters (β, γ) are directly connected to those multipliers by the following relations

$$q_{20} = \frac{\beta \cos \gamma}{C}, \quad q_{22} = \frac{\beta \sin \gamma}{\sqrt{2}C}, \quad C = \sqrt{\frac{5}{4\pi} \frac{4\pi}{3r_0^2 A^{5/3}}}, \quad (3.24)$$

with A being the mass number and a typical $r_0 = 1.2$ fm. These constraints allow to explore the (β, γ) plane to generate the wave functions to be used in the configuration mixing calculations.

The final states for each I are obtained by taking linear combinations of all projected states with different shapes and third components of the angular momentum in the intrinsic frame K . The coefficients of these linear combinations are given after solving the so-called Hill-Wheeler-Griffin equations within the Generator Coordinate Method (GCM) framework. More details about these methods can be found in refs. [BHR03; RE10] and references therein.

The two major limitations of the model are the conservation of parity and time-reversal symmetries of the intrinsic wave functions. The first one restricts the study to positive parity states and neglects the influence of the octupole degree of freedom that could play a role in the $A \approx 130$ region. The second restriction limits the description of the moments of inertia and, therefore, the quantitative precision of the energy levels [Zdu07; LRV04].

4 Coulomb excitation theory

The experimental technique of Coulomb excitation (Coulomb excitation) is used in nuclear physics to probe the electromagnetic aspects, especially the quadrupole collectivity, of nuclear structure. A nucleus is excited by an inelastic collision with another nucleus through the electromagnetic interaction. The mathematical description of the Coulomb excitation formalism was developed by Alder and Winther [Ald56; AW75] in the 1950s.

4.1 Semi-classical description

The experimental perception of Coulex is the excitation of a nucleus by an inelastic collision with another nucleus through the electromagnetic interaction. In order to ensure experimentally that the interaction is purely electromagnetic in nature (and not nuclear) "safe" conditions are chosen. In low-energy Coulomb excitation this is achieved by keeping the beam energy E of the projectiles (mass number A_1 , charge number Z_1) below the Coulomb barrier (in the center-of-mass system)

$$V_C = \frac{e^2}{4\pi\epsilon_0} \frac{Z_1 Z_2}{R_1 + R_2} \approx \frac{Z_1 Z_2}{A_1^{1/3} + A_2^{1/3}}. \quad (4.1)$$

A more safe requirement is the empirically found limit by Douglas Cline, the so called Cline's criterion [Cli12]:

$$E_{max} [MeV] = 1.44 \underbrace{\frac{A_1 + A_2}{A_2}}_{CMS \rightarrow LAB} \frac{Z_1 Z_2}{1.25(A_1^{1/3} + A_2^{1/3}) + 5} \quad (4.2)$$

In this formula +5 in the denominator indicates a safety margin of 5 fm. This can still be insufficient for light projectiles of carbon or oxygen, e.g., but has proven to be a good criterion for heavier projectiles as used in this work. The following description of the Coulex formalism can be found in great detail in the benchmark textbook of Alder and Winther [AW75] and a review article [Ald56].

During a collision between two heavy ions the electromagnetic interaction depends on the electromagnetic multipole moments of both nuclei. The great simplification in the semi-classical description of Coulex arises from the fact that only the Coulomb field can ensure that the projectile does not penetrate into the nucleus. That leads to the demand that the *Sommerfeld parameter*

$$\eta = \frac{Z_1 Z_2 e^2}{\hbar v_1} \quad (4.3)$$

must be large compared to unity ($\eta \gg 1$). This is at the same time the condition for the applicability of classical physics for the description of the relative motion of nuclei. The hyperbola (see fig. 4.1) is completely defined by the charge numbers Z_1, Z_2 of projectile and target, the energy E and the center-of-mass scattering angle ϑ . Thereby the differential scattering cross-section is given by the classical Rutherford formula

$$\left(\frac{d\sigma}{d\Omega} \right)_{Rutherford}^{CMS} = \left(\frac{e^2}{4\pi\epsilon_0} \frac{Z_1 Z_2}{4E} \right)^2 \frac{1}{\sin^4 \left(\frac{\vartheta}{2} \right)}. \quad (4.4)$$

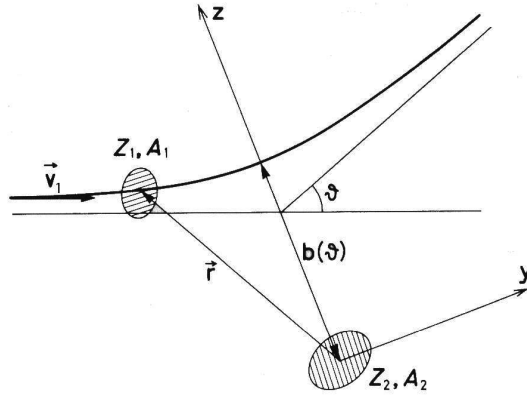


Figure 4.1.: The defining parameters of a Coulomb excitation process are the beam energy $E = \frac{1}{2} m_1 v_1^2$ in the laboratory frame, and the scattering angle ϑ .

Translated into for nuclear physics more convenient TORBEN¹ units (E in MeV, σ in millibarn) this can be written as

$$\left(\frac{d\sigma}{d\Omega} \right)_{Rutherford}^{CMS} [mb/sr] = 1.296 \left(\frac{Z_1 Z_2}{E} \right)^2 \frac{1}{\sin^4 \left(\frac{\vartheta}{2} \right)} \quad (4.5)$$

$$\left(\frac{d\sigma}{d\Omega} \right)_{Rutherford}^{LAB} [mb/sr] = 1.296 \left(\frac{Z_1 Z_2}{E} \right)^2 \frac{\sin^2 \vartheta}{\sin^4 \left(\frac{\vartheta}{2} \right) \sin^2 \theta_1 |\cos(\vartheta - \theta_1)|}, \quad (4.6)$$

where θ_1 is the scattering angle of the projectile in the laboratory frame (θ_2 in analogy for the target nucleus).

Sometimes it is not clear in literature if a certain formula is expressed in the center-of-mass system (CMS) or the laboratory system (LAB) and in which units some variables are meant to be used. To avoid confusion in this work either it is explicitly stated what the formula contains or one can check in the table of symbols at the end of the work, where all variables used throughout the work are explained.

In the collision none (elastic scattering), one or even both nuclei may be excited. The differential cross-section for the Coulomb excitation of a nucleus to a state $|n\rangle$ is expressed by a certain probability P_n relative to the Rutherford cross-section:

$$\left(\frac{d\sigma}{d\Omega} \right)_n = P_n \left(\frac{d\sigma}{d\Omega} \right)_R \quad (4.7)$$

¹ Theoretical Observables Rewritten for the Benefit of Experimental Nucleists as suggested by Alder and Winther [AW75, p. 268]

This excitation probability P_{if} from the initial nuclear state i to the final state f can be expressed in terms of the amplitudes a_{if} for a transition by

$$P_{if} = |a_{if}|^2. \quad (4.8)$$

The excitation is caused by the time-dependent electromagnetic field which sweeps over the nucleus as the projectile moves along the hyperbolic orbit. So to calculate the excitation amplitudes a_{if} it is mandatory to solve the time-dependent Schrödinger equation for the nucleus

$$i\hbar \frac{\partial}{\partial t} |\psi(t)\rangle = (H_0 + V(t)) |\psi(t)\rangle, \quad (4.9)$$

where $|\psi(t)\rangle$ is the time-dependent state, H_0 is the Hamiltonian of the free nucleus, and $V(t)$ is the electromagnetic interaction. One may formulate the Schrödinger equation as a system of coupled differential equations by expanding the nuclear state vector $|\psi(t)\rangle$ as a complete set of the orthogonal eigenstates of the time independent free nuclear Hamiltonian H_0 . The free nucleus eigenstate wave functions $|n\rangle$ of H_0 satisfy the time-independent Schrödinger equation

$$H_0 |n\rangle = E_n |n\rangle \quad (4.10)$$

with eigenvalues E_n and the time-dependent excitation amplitudes $a_n(t)$ are introduced as the corresponding coefficients:

$$|\psi(t)\rangle = \sum_n a_n(t) |n\rangle e^{-iE_n t/\hbar} \quad (4.11)$$

The excitation amplitudes become time independent before and after collision ($t \rightarrow \pm\infty$), when the interaction $V(t)$ vanishes. Substituting eq. (4.11) in the Schrödinger equation (4.9) results in the following set of linear differential equations taking into account the orthonormality of the eigenstates:

$$i\hbar \dot{a}_n = \sum_m \langle n | V(t) | m \rangle e^{i(E_n - E_m)t/\hbar} a_m(t) \quad (4.12)$$

This quantum-mechanical treatment of the nucleus in the time-dependent electric field together with the classical behavior of the projectile in a hyperbolic orbit, resulting in a set of coupled differential equations, is called the *semi-classical approximation* in Coulomb excitation theory. The equations can be solved by first and second order perturbation theory, treating the potential $V(t)$ as a time-dependent perturbation.

4.2 Connection to observables

For a transition from an initial state $|i\rangle$ to a final state $|f\rangle$ one obtains for the transition amplitudes in first order perturbation theory

$$a_{if} = \frac{1}{i\hbar} \int_{-\infty}^{\infty} \langle f|V(t)|i\rangle e^{i(E_f - E_i)t/\hbar} dt. \quad (4.13)$$

For electric excitations the main interaction $V(t)$ in the aforementioned eqs. (4.12) and (4.13) is the Coulomb energy. In order to evaluate the matrix elements in eq. (4.13) an expansion of $V(t)$ in multipole components can be done:

$$\begin{aligned} V(t) &= \int \rho_n(\vec{r}) \varphi(\vec{r}, t) d\tau \\ &= \sum_{\lambda=1}^{\infty} \sum_{\mu=-\lambda}^{\lambda} \frac{4\pi Z_1 e}{2\lambda + 1} r_1^{-\lambda-1}(t) Y_{\lambda\mu}(\theta_1, \phi_1) \mathfrak{M}(E\lambda, \mu) \end{aligned} \quad (4.14)$$

This holds true if the projectile remains outside the nucleus. The electrical multipole moments of the nucleus are defined by

$$\mathfrak{M}(E\lambda, \mu) = \int \vec{r}^{\lambda} Y_{\lambda\mu}(\theta, \phi) d^3\vec{r} \quad (4.15)$$

with polar coordinates in a system with origin in the nuclear center of mass and $Y_{\lambda\mu}(\theta, \phi)$ being the normalized spherical harmonics.

It is convenient to replace the multipole operator matrix elements by reduced matrix elements $M_{if} = \langle I_i || \mathfrak{M}(\lambda) || I_f \rangle$ using the Wigner-Eckart theorem:

$$\langle I_i m_i | \mathfrak{M}(\lambda, \mu) | I_f m_f \rangle = (-1)^{I_i - m_i} \underbrace{\begin{pmatrix} I_i & \lambda & I_f \\ -m_i & \mu & m_f \end{pmatrix}}_{3j\text{-symbol}} \langle I_i || \mathfrak{M}(\lambda) || I_f \rangle \quad (4.16)$$

In this work the phase convention is used that the phases of the nuclear wavefunctions are chosen in such a manner that the reduced matrix elements are real. In this convention the up- and down-going matrix elements are connected in the following way:

$$\langle I_i || \mathfrak{M}(\lambda) || I_f \rangle = (-1)^{I_f - I_i} \langle I_f || \mathfrak{M}(\lambda) || I_i \rangle \quad (4.17)$$

At this point the reduced transition probability for a radiative transition of multipole order $\pi\lambda$ can be introduced:

$$\begin{aligned} B(\pi\lambda; I_i \rightarrow I_f) &= \sum_{M_f \mu} | \langle I_i M_i | \mathfrak{M}(\pi\lambda, \mu) | I_f M_f \rangle |^2 \\ &= \frac{1}{(2I_i + 1)} | \langle I_i || \mathfrak{M}(\pi\lambda) || I_f \rangle |^2. \end{aligned} \quad (4.18)$$

For a one-step excitation from the ground state the differential excitation cross-section of order $E\lambda$ is given by

$$d\sigma_{E\lambda} = \left(\frac{Z_1 e}{\hbar v_1} \right)^2 a^{-2\lambda+2} B(E\lambda) df_{E\lambda}(\vartheta, \xi), \quad (4.19)$$

with

$$df_{E\lambda}(\vartheta, \xi) = \frac{4\pi^2}{(2\lambda + 1)^3} \sum_{\mu} |Y_{\lambda\mu} \left(\frac{\pi}{2}, 0 \right)|^2 |I_{\lambda\mu}(\vartheta, \xi)|^2 \sin^{-4} \left(\frac{\vartheta}{2} \right) d\Omega. \quad (4.20)$$

Again, $Y_{\lambda\mu}$ denotes the normalized spherical harmonics and $I_{\lambda\mu}$ are orbital integrals describing the orbit in hyperbolic coordinates in a convenient way. The exact definitions and tabulated values can be found in [Ald56]. Here the differential Coulomb excitation function $df_{E\lambda}(\vartheta, \xi)$ depends through the orbital integrals $I_{\lambda\mu}$ on the adiabaticity parameter ξ , rewritten with eq. 4.3 to

$$\xi = \frac{Z_1 Z_2 e^2}{\hbar v_1} \frac{\Delta E}{2E} = \eta \frac{\Delta E}{2E}. \quad (4.21)$$

Selection rules and transition properties

The excitation processes considered so far are subject to the standard parity selection rules for electromagnetic multipole radiation. An electric excitation of order λ involves a parity change of $(-1)^\lambda$, whereas for magnetic excitation $\pi_\gamma = (-1)^{\lambda+1}$ is valid. In summary:

$$\begin{aligned} E_\gamma &= E_i - E_f \\ |I_i - I_f| &\leq \lambda \leq I_i + I_f \\ \pi_i \cdot \pi_\gamma &= \pi_f \end{aligned}$$

The complete formalism of electromagnetic transitions strengths is outlined in appendix D.

This section so far just considered electric excitations in first order (one-step). For the description of magnetic excitations $V(t)$ in eq. (4.14) has to be expressed as the magnetic interaction. Then eqs. (4.15, 4.19) and (4.20) can be rewritten analogously for magnetic transitions yielding a differential cross-section

$$d\sigma_{M\lambda} = \left(\frac{Z_1 e}{\hbar v_1} \right)^2 a^{-2\lambda+2} B(M\lambda) df_{M\lambda}(\vartheta, \xi). \quad (4.22)$$

For small EM interactions $V(t) \ll H_0$, such as, e.g., at low energies or light projectiles $Z \ll 1/\alpha = 137$, first order perturbation is valid for Coulomb excitation experiments. However, corrections arise for the conducted experiments with heavy ions at the Coulomb barrier from higher order perturbations that have to be accounted for as well. Those effects can be summarized as *multi-step Coulomb excitation*. Introducing an intermediate state $|z\rangle$ the transition amplitude a_{if} consists of two components

$$a_{if} = a_{if}^{(1)} + a_{if}^{(2)}, \quad (4.23)$$

where $a_{if}^{(1)}$ is the first order amplitude (see eq. 4.13) and $a_{if}^{(2)}$ takes care of the second order effects stemming from the intermediate state(s) $|z\rangle$:

$$a_{if}^{(2)} = \frac{1}{i\hbar} \sum_z \int_{-\infty}^{\infty} \langle f | V(t) | z \rangle e^{i(E_f - E_z)t/\hbar} dt \int_{-\infty}^{\infty} \langle z | V(t') | i \rangle e^{i(E_z - E_i)t'/\hbar} dt' \quad (4.24)$$

Thereby the cross-sections and excitation probabilities, eq. (4.8), must be modified as well, e.g., by inserting eq. (4.23) the excitation amplitude is defined as

$$P_{if} = P_{if}^{(1)} + P_{izf}^{(1,2)} + P_{izf}^{(2)}, \quad (4.25)$$

with the following meaning of the 3 terms:

$P_{if}^{(1)}$ This is the first order excitation probability as derived in the beginning of this section without any intermediate state as can be seen in fig. 4.2(a).

$P_{izf}^{(2)}$ For the case of one intermediate state the second order excitation probability can either be a double excitation or a reorientation.

$P_{izf}^{(1,2)}$ The interference of excitation amplitudes from first and second order excitations means the final state $|f\rangle$ is excited on both ways.

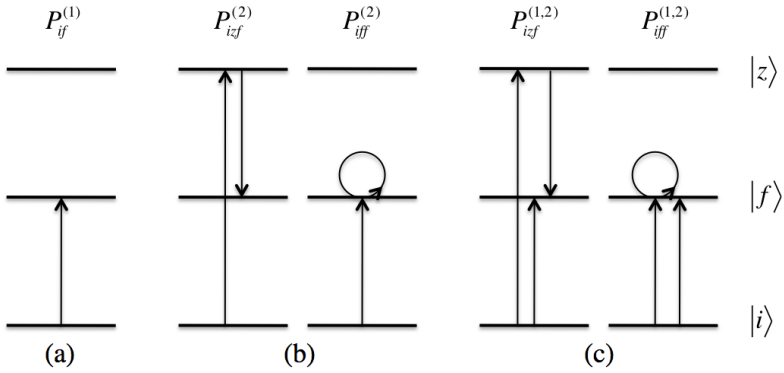


Figure 4.2.: The different excitation mechanisms are illustrated with an exemplary 3-state system where the intermediate state $|z\rangle$ lies above the final state $|f\rangle$: (a) first order excitation, (b) second order double excitation (left) and reorientation effect (right), (c) interference effects of (a) and (b).

While the double excitations can be understood as two single excitations, one following the other before the excited state de-excites, the reorientation effect is somehow more complex. In this case the intermediate and final state are identical and it is the transition between two degenerated levels. In terms of quantum mechanics it has to be understood as a redistribution of the population of the magnetic substates of the final state. The excitation probability of the second step is directly proportional to the *intrinsic electric quadrupole moment* Q_0 of the final state. That is used in this work to determine the quadrupole moments of excited 2_1^+ states, where the connection to the quadrupole moment, derived from eq. (2.14), is the following:

$$M_{22} = \langle 2_1^+ || \mathcal{M}(E2) || 2_1^+ \rangle = -\sqrt{\frac{1}{14\pi}} \frac{5}{2} Q_0 \approx -0.377 Q_0 \quad (4.26)$$

However, in a Coulex experiment an ensemble of nuclei is measured, that's the reason why only the *spectroscopic quadrupole moment* Q can be determined. Q_0 refers to the symmetry axis of one particular nucleus. From eq. 2.15 the following transformation results for the case of a 2_1^+ state:

$$Q = -\frac{2}{7} Q_0 \quad \text{and inserted in eq. (4.26):} \quad M_{22} = 1.319 Q \quad (4.27)$$

In an actual experiment it is only possible to measure the excitation cross-section $\sigma(2_1^+)$ depending on beam energy and scattering angle. From the theoretical

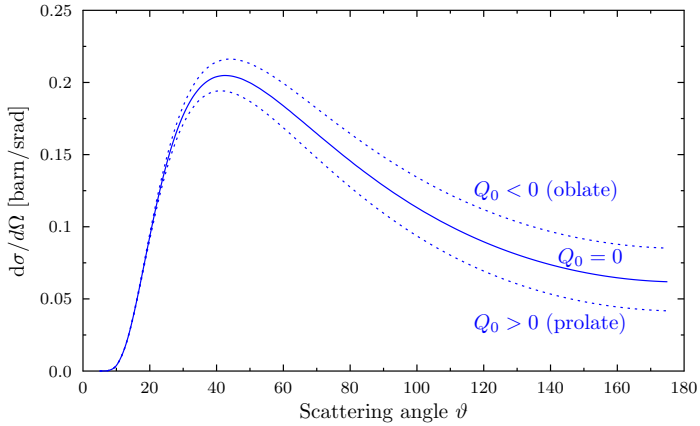


Figure 4.3.: The Coulex cross-section $\sigma(2_1^+)$ depends on the center-of-mass scattering angle ϑ and the quadrupole moment.

Coulex point of view $\sigma(2_1^+)$ depends directly on two matrix elements (beside feeding states), in first order on the transitional matrix element M_{20} and in second order also on the diagonal matrix element M_{22} . Therefore, the Coulomb excitation yield can be used for extracting information on the quadrupole moment $Q(2_1^+)$. Figure 4.3 shows a typical form of the cross-section as a function of the center-of-mass scattering angle ϑ for various quadrupole moments.

4.3 Angular distribution of γ -radiation

An angular distribution function describes in general the relative probability for the γ radiation in a transition (de-excitation) from a final state $|f\rangle$ back to the initial state $|i\rangle$ to be emitted into a direction $(\theta_\gamma, \phi_\gamma)$:

$$\frac{dW_\gamma^{if}(\theta_\gamma, \phi_\gamma)}{d\Omega_\gamma} \quad (4.28)$$

The distribution depends on the excitation process and thereby again on the transition amplitudes a_{if} of eq. (4.13). The dependence on the angle ϕ_γ vanishes either if the orientation of the reaction plane is entirely ignored (no particle detector) or for a particle detector, which is symmetric around ϕ , when integrating over the azimuthal particle angle ϕ_1 or ϕ_2 . This is valid for the circular detectors used in all experiments of this work. The final distribution then simplifies to

$$W(\vartheta_\gamma) = \sum_k a_k^\lambda(\xi) A_k^{(\lambda)} P_k(\cos \theta_\gamma), \quad (4.29)$$

where the range of k is limited by the multipole order λ , $P_k(\cos \theta_\gamma)$ are the Legendre polynomials and the coefficients $a_k^\lambda(\xi)$ and $A_k^{(\lambda)}$ are given below. The variable ξ is defined in eq. (4.21) and θ_γ is the angle between incident beam and emitted γ ray. The coefficients $a_k^\lambda(\xi)$ are given by

$$a_k^\lambda(\xi) = \frac{b_k^\lambda(\xi)}{b_0^\lambda(\xi)}. \quad (4.30)$$

For the relevant case of electric transitions $b_k^\lambda(\xi)$ is defined as follows:

$$\begin{aligned} b_k^{E\lambda}(\xi) = & -(2k+1)^{-\frac{1}{2}} \begin{pmatrix} \lambda & \lambda & k \\ 1 & -1 & 0 \end{pmatrix}^{-1} \\ & \times \sum_{\mu\mu'\kappa} (-1)^\mu \begin{pmatrix} \lambda & \lambda & k \\ \mu & -\mu' & \kappa \end{pmatrix} Y_{\lambda\mu} \left(\frac{\pi}{2}, 0 \right) Y_{\lambda\mu'} \left(\frac{\pi}{2}, 0 \right) \\ & \times \int_0^\pi I_{\lambda\mu}(\vartheta, \xi) I_{\lambda\mu'}(\vartheta, \xi) Y_{k\kappa} \left(\frac{\pi}{2}, \frac{\pi + \vartheta}{2} \right) \frac{\cos \left(\frac{\vartheta}{2} \right)}{\sin^3 \left(\frac{\vartheta}{2} \right)} d\vartheta \end{aligned} \quad (4.31)$$

Here $I_{\lambda\mu}$ are the orbital integrals and $Y_{\lambda\mu}$ the spherical harmonics as introduced in sec. 4.2. The angle ϑ denotes the scattering angle in the center-of-mass system and

by changing the integration interval (which in eq. (4.31) is the complete region from 0 to π) one can adjust it to the settings of a certain experiment, e.g., ranging over the scattering angles covered by the particle detector. The coefficients $A_k^{(\lambda)}$ are defined with the help of the geometrical factors F_k to

$$A_k^{(\lambda)} = F_k(\lambda I_i I_f) \sum_{LL'} F_k(LL' I_i I_f). \quad (4.32)$$

The geometrical factors F_k themselves are defined by

$$F_k(LL' I_i I_f) = (-1)^{I_i + I_f - 1} \sqrt{(2k+1)(2I_f+1)(2L+1)(2L'+1)} \\ \times \underbrace{\begin{pmatrix} L & L' & k \\ 1 & -1 & 0 \end{pmatrix}}_{3j\text{-symbol}} \underbrace{\left\{ \begin{matrix} L & L' & k \\ I_2 & I_2 & I_1 \end{matrix} \right\}}_{6j\text{-symbol}}. \quad (4.33)$$

A more detailed derivation of the angular distributions can be found in [AW75; Ald56]. For an explicit calculation beam energy E , excitation energy ΔE , charge and mass numbers of projectile and target are included in the parameter ξ . For a given multipole order λ the calculation can be performed with the software Mathematica, e.g., as presented in ref. [Bau07]. The experimental measurement of the angular distribution allows to draw conclusions about the multipolarity of the observed transition or under certain conditions even of the g-factor of the excited state [Bau07].

Regarding angular distributions two effects have to be taken into account when comparing to experimental data. Both effects result in an attenuation of the distribution, which can be mathematically described by multiplying the attenuation coefficients Q_k and G_k with $0 \leq Q_k, G_k \leq 1$ to eq. 4.29:

$$W(\vartheta_\gamma) = \sum_k a_k^\lambda(\xi) A_k^{(\lambda)} Q_k G_k P_k(\cos \theta_\gamma) \quad (4.34)$$

Finite detector size The used high-purity Germanium detectors as well as most of the other available detectors have a non-negligible physical extension. A finite solid angle is covered by the detector which results in an uncertainty in the angle of the detected γ ray. The resulting attenuation of the angular distribution is usually denoted by the Q_k coefficients.

Deorientation effect After excitation the aligned nuclear spin \vec{I} of a nucleus can, during its lifetime, couple with the randomly oriented spin \vec{J} of the surrounding electrons to a total angular momentum $\vec{F} = \vec{I} + \vec{J}$ due to the atomic

hyperfine interaction. This happens when the nuclei recoil into vacuum. The hyperfine interaction changes the relative population of the magnetic substates and therefore attenuates the angular distribution. The standard notation of the factors is G_k , which can be even time-dependent depending on the model used for the hyperfine interaction.

4.4 Coulomb excitation codes: CLX and GOSIA

For the evaluation of a Coulex experiment a proper computer code to handle multiple excitations and solving the coupled differential equations as in eq. (4.12) is essential. The original Coulex code was developed by Alder and Winther in 1965 [AW66, p. 303ff] in Fortran, a fact that has endured to this date.

Phase convention

There is a possible source of confusion because at this time the reduced matrix elements were defined in the following way [AW66, p. 305, eq. (13)]:

$$M_{if} = \langle I_i || i^\lambda \mathfrak{M}(\lambda) || I_f \rangle \quad (4.35)$$

This convention coming with the original code was used in publications up to the eighties (e.g., see in [Par76; SV88]). In 1975 Alder and Winther suggested a new way using the phase convention

$$RPT |Im\rangle = |Im\rangle \quad (4.36)$$

where P is the parity operator, R a rotation of 180° around the y-axis and T the time-reversal operator [AW75, appendix E]. Then the reduced matrix element is defined such that it always becomes real:

$$M_{if} = \langle I_i || \mathfrak{M}(\lambda) || I_f \rangle \quad (4.37)$$

A mixing of both conventions becomes problematic especially when dealing with the quadrupole moment of the 2_1^+ state. While in the old convention one would obtain $M_{22} = -1.319Q$ it is actually $M_{22} = 1.319Q$ in the new one, without a change in sign between matrix element and quadrupole moment. A mistake would lead to a completely opposite assignment of deformation! I follow here the convention from eq. (4.36).

The experiments analyzed in this work represent a special case of Coulex analysis where the matrix elements connected to the 2_1^+ state of the projectile are the observables of interest and the beam intensities are not known. Therefore an independent normalization is necessary. Usually this is performed by simultaneously measuring the target excitation. Providing the experimental conditions (scattering angles, beam energy, beam purity) are known/measured and the properties of

the target (purity, matrix elements) are well-known the cross-section for projectile excitation σ^P can be normalized to the target excitation cross-section σ^T via

$$\sigma^P(M_{20}, M_{22}) = \frac{N_\gamma^P \epsilon_\gamma^T W(\theta)^T}{N_\gamma^T \epsilon_\gamma^P W(\theta)^P} \sigma^T \frac{1 - Q^T}{1 - Q^P}. \quad (4.38)$$

N_γ denotes the measured events (counts) for the transition $2_1^+ \rightarrow 0_1^+$ of the projectile or target nucleus, which, of course, have to be corrected for their relative efficiencies ϵ_γ and the angular distribution $W(\theta)$. The fraction of a possible contamination of the beam (Q^P) or the target material (Q^T) is considered as well. The determination of the efficiency is described in great detail in sec. 6.2. The angular correction is taken into account by the Coulex codes. In this case the projectile cross-section σ^P depends solely on the transitional matrix element M_{20} and the diagonal matrix element M_{22} . The same is true for the target excitation but in this case the target is chosen in such a way that its 2_1^+ state is known very well with small errors of the lifetime (M_{20}) and the quadrupole moment (M_{22}).

To determine the transition strength and the quadrupole moment of the projectile's 2_1^+ state the experiment has to be divided in $i \geq 2$ sub-experiments regarding different ranges of scattering angles. That makes it possible to use the dependence of the cross-section on the scattering angle. Then eq. (4.38) has to be solved including all experimental and systematic errors for each sub-experiment i . A higher number of sub-experiments can improve the error of the final result as long as the statistics of each sub-experiment is sufficient. Therefore, a trade-off between number of sub-experiments and remaining statistics (accuracy of measured yields) in the sub-experiments has to be done.

CLX/DCY

The program package CLX and DCY [Owe80] works nicely together to describe the combined excitation and de-excitation process based on the original code but considering the new phase convention. A simple input file (see app. A) requires the following information:

- mass numbers A_1 and A_2 of projectile and target
- charge numbers Z_1 and Z_2 of projectile and target
- flag for projectile or target excitation
- beam energy E

-
- angular range in ϑ and stepsize in the CMS
 - list of nuclear states (spin, energy, parity, K quantum number)
 - list of transitions between those states (initial state, final state, matrix element, transition type)

The output provides a complete calculation of the statistical tensors for every angle as well as excitation probabilities and cross-sections. DCY requires the CLX output and is able to calculate cross-sections in arbitrary units. It is more appropriate to analyze experimental data and compare with experimental yields because more parameters regarding the experimental conditions can be taken into account. The complete input is summarized in the following list:

- output file `clxcdcy.dat` of the CLX calculation
- position file of the γ -ray detectors with angles θ_γ and ϕ_γ
- angular range in ϑ and ϕ of the scattered particles
- parametrization for the deorientation effect
- conversion coefficients

For the projectile's 2_1^+ state both the transitional and the diagonal matrix elements, M_{20} and M_{22} , affect the Coulomb excitation cross section σ^P . Using CLX and DCY these matrix elements are varied in such a way that the experimental γ -ray yields are reproduced. Due to the error propagation the mutual dependence of σ^P on M_{20} and M_{22} results in a Gaussian-shaped band in the two-dimensional (M_{22}, M_{20}) plane. The corresponding band for each sub-experiment i is restricted by the required reproduction of the observed Coulomb excitation cross-section. In the intersection area a maximum-likelihood analysis as used in this context by Ekström et al. [Eks09], determines a 1σ contour, which gives the experimental results for M_{20} and M_{22} , and thereby transition strength and quadrupole moment, when projected on the corresponding axis.

GOSIA

In contrast to CLX the program GOSIA [CCW83; Cli12] includes beside the excitation and de-excitation mechanism a fit routine that adjusts the matrix elements automatically to reproduce the experimental yields. Furthermore it is more convenient for the user to introduce the experimental conditions and known lifetimes,

branching ratios or mixing ratios in addition to the matrix elements in the input files. Beside the required input for a CLX calculation the following additional input is necessary (see app. B):

- energy loss of projectiles in the target
- efficiency corrected γ yields

The energy loss is necessary because GOSIA also integrates over the energy loss in the target for the calculations of the Coulomb excitation process. Efficiency corrected yields for projectile and target excitation have to be given because GOSIA adjusts the matrix elements during the fit process to meet the experimental yields while with CLX and DCY this has to be done by hand as described above. The aforementioned deorientation is taken into account by GOSIA through a modified version of the two-state model [BS77; Bre77; Cli12]. For the error estimation GOSIA is capable to perform a calculation for diagonal and correlated errors and thereby also to give a proper error estimation for each fitted matrix element.

For the special case of simultaneous excitation of projectile and target the use of the adjusted code GOSIA2 is comfortable. GOSIA2 fits matrix elements for the nucleus of interest (the "investigated nucleus"). It normalizes the Coulomb excitation γ -ray yields of the investigated nucleus to those of the collision partner. However, GOSIA2 only correlates errors among the measured matrix element(s) of each collision partner individually, *i.e.*, it does not perform a complete correlated error calculation including both the beam nucleus' and target nucleus' free parameters. Hence, using the present version of GOSIA2, in order to get a complete correlated error analysis, some brute-force hand-calculations are necessary. In general, GOSIA2 is used to measure only a few parameters for both collision partners, since the original GOSIA can be used to self-normalize for large data sets. Therefore, it is feasible to calculate the correlated errors by hand using GOSIA2 (comp. [Hay]) as it was done in ref. [Alb12]. In the context of this work a C++ program was written to provide an easy possibility for handling the process of many GOSIA2 calculations mapping the necessary area of the (M_{22}, M_{20}) plane. The source code of this program is attached in appendix C.

4.5 The DSA principle

For lifetime measurements of nuclear states of a few picoseconds (ps) down to some femtoseconds (fs), the Doppler-shift attenuation method (DSAM) can be applied [AF79]. In general the investigated state of a nucleus is populated while the nucleus is in motion (*e.g.*, the projectile in a Coulomb excitation experiment) and the de-excitation occurs during the deceleration of the ion in a thick target. A certain Doppler shift can be detected under forward or backward direction depending on magnitude and direction of the ion velocity vector according to

$$E_{\gamma}(\theta_{\gamma}, \beta(t)) = \frac{1 - \beta(t) \cos \theta_{\gamma}}{\sqrt{1 - \beta(t)^2}} E_{\gamma_0}. \quad (4.39)$$

Because the de-excitation occurs at different ion velocities during the slowing down procedure, a distribution of Doppler-shifted photon energies can be observed that is characteristic for the lifetime of the state.

Employing the DSA method, usually an excitation target layer is placed directly on top of the stopper material. Consequently, the de-excitation occurs during the ion is decelerated in the stopper material. In some experiments even a single layer target is used where the same material is responsible for excitation and slowing down of the ions (*cf.* subsec. 6.5.1). In contrast to other approaches like Recoil distance Doppler-shift (RDDS), *e.g.*, the DSA method includes de-excitations at all velocities at all times t after the populating process ($t=0$ being the time of projectile excitation), *i.e.* a continuous spectrum of Doppler-shifted γ -ray energies is observed.

The measurement of Doppler-shifted energies is equivalent with the measurement of the projectile velocity projected on the position of observation, *cf.* eq. (4.39), if the rest energy of the transition radiation is known. Furthermore, knowing the temporal evolution $\beta(t)$ of the deceleration process of the projectile, the distribution of times of de-excitation and thus the lifetime can be extracted from the distribution of projectile velocities at the time of de-excitation. The principle of the method is sketched in fig. 4.4. Because there are a large number of interactions and a slight variation of the initial conditions for every ion, the deceleration has to be described as a stochastic process. Only a statistical distribution $p(\vec{\beta}, t)$ of the ion velocity in both magnitude and direction for every time t after excitation can be specified. The four dimensional distribution function $p(\vec{\beta}, t)$ is also called *stopping matrix*. Every combination of beam species and target material requires a specific stopping matrix for every beam energy, calculated using Monte-Carlo simulations (*comp.* [Sta11]).

For the Doppler-shifted energy of the emitted γ radiation observed in a detector not the magnitude of the recoil velocity, but its projection to the direction of

observation $(\theta_\gamma, \phi_\gamma)$ is relevant. Therefore, the velocity vector of every simulated ion has to be projected on the unit vector of the direction of observation at every time t after excitation. The result is a time-resolved probability distribution for the projected ion velocity. The distribution of the Doppler-shifted γ rays emitted in the direction of the detector is calculated from applying the Doppler formula, eq. (4.39), to this distribution of projected velocities and weighting it with the assumed decay function $A(t, \tau)$. A realistic γ -ray spectrum is then obtained by convoluting the distribution of the Doppler-shifted γ rays emitted in the direction of the detector with the detector response function and integrating it over the detector solid angle.

The lifetime dependence of the peak's shape in the energy spectrum, the *line-shape*, is introduced by the lifetime dependence of the decay function $A(t)$. Connected via the stopping matrix, the shape of $A(t)$ determines the distribution of recoil velocities at the time of de-excitation and, thus, the distribution of Doppler shifts "seen" by the γ -ray detectors. A short lifetime causes a steep decay function, the emission of γ quanta preferably takes place at high recoil velocities and thus high Doppler shifts. In contrast, for larger lifetimes more de-excitations happen at low velocities and therefore more events with smaller Doppler shifts are registered in the detector. The expressions long/short for the lifetime refer to the duration of the stopping process of the projectiles in the target. This duration defines the

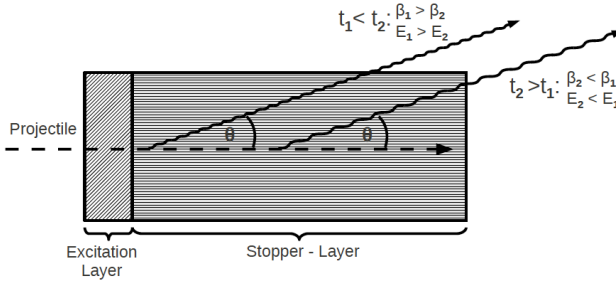


Figure 4.4.: Illustration of the formation of the spectrum of Doppler-shifted energies of γ quanta: Excited nuclei de-excite at different times t and thus after different propagation times in the stopper material. Consequently they emit their transition radiation while moving with different velocities. Therefore, different Doppler-shifted energies are registered in detectors placed under forward (as in this figure) or backward angles with respect to the beam axis. (Picture: Courtesy of C. Stahl)

range of lifetimes the DSA method is sensitive to. It can be influenced by the initial velocity of the recoiling nuclei and the stopping material.

Besides the history of the stopping process, also the shape of complex decay functions (feeding) affects the lineshape. In order to experimentally determine lifetimes from measured energy spectra, theoretical lineshapes calculated with the aid of computer codes are fitted to the experimentally determined lineshapes. Amongst others, the lifetime is the main parameter to be varied during the fitting procedure and extracted from it.

The newly developed Analysis Program for Continuous Angle DSAM (AP-CAD) [Sta11; Sta13] is introduced in sec. 6.3 and used for analysis of experimental data in this work (see subsecs. 6.4.1 and 6.5.1).



5 Experimental setups

Coulomb excitation experiments with beams of $^{130,132}\text{Ba}$ and $^{140,142}\text{Ba}$ for the measurement of lifetimes and quadrupole moments, as well as beams of ^{140}Nd and ^{142}Sm for the measurement of transition strengths, conducted at two different facilities, lay the groundwork of this thesis. Both experimental setups are presented in this chapter, on the one hand at the Argonne National Lab, on the other hand at CERN¹. The main reason for the choice of two locations lies in the usage of stable and unstable beams, each of them requiring a certain kind of accelerator system.

¹ Conseil Européen pour la Recherche Nucléaire

5.1 ATLAS & Gammasphere

The Argonne National Lab (ANL) near Chicago, IL, United States, is one of the U.S. Department of Energy's largest national laboratories for scientific and engineering research. For nuclear structure studies ATLAS, the Argonne Tandem Linac Accelerator System, is available.

5.1.1 Accelerator system and beam production

ATLAS was the world's first superconducting linear accelerator for heavy ions at energies in the vicinity of the Coulomb barrier. ATLAS can provide beams of essentially all stable isotopes from proton to uranium, and a variety of light radioactive beams through the in-flight production program as well as heavier neutron-rich isotopes from CARIBU (CALifornium Rare Isotope Breeder Upgrade).

The whole ATLAS consists of a sequence of machines (see fig. 5.1), each of them accelerates charged atoms and then feeds the beam into the next section for an additional energy gain. The beams are provided by one of two injector accelerators, either a 9MV electrostatic tandem Van de Graff, or a 12MV low-velocity linac and electron cyclotron resonance (ECR) ion source named Positive Ion Injector. The beam from these injectors is sent to the 20MV booster linac, before finally going into the 20MV ATLAS linac section (comp. [Sav]).

For the production of the $^{130,132}\text{Ba}$ beams the ECR source was used in conjunction with enriched source material in the form of Barium carbonate (BaCO_3). The enrichment to 3.9% (^{130}Ba) and 13.1% (^{132}Ba) was necessary due to the low natural abundance (0.1%) of both isotopes of interest.

5.1.2 Spectrometer and target chamber

The Gammasphere array [Lee90], consisting of up to 110 high-purity Compton-shielded Germanium detectors, is available for the detection of γ radiation. The photograph in fig. 5.2 shows the array in preparation for the experiments on $^{130,132}\text{Ba}$. All detectors have an efficiency of 82% compared to the NaI standard and a resolution of $\approx 2.5\text{keV}$ at the γ -ray energy of 1.3 MeV. The distance between the front of the detectors and the target position is about 25cm which results in an opening angle of 14.8° for a single detector. All detectors together cover up to 46% of the total solid angle, giving a photo peak efficiency of 9.4% at 1.3 MeV. The detectors are ordered in rings of 17 different polar angles θ . This is summarized in tab. 5.1.

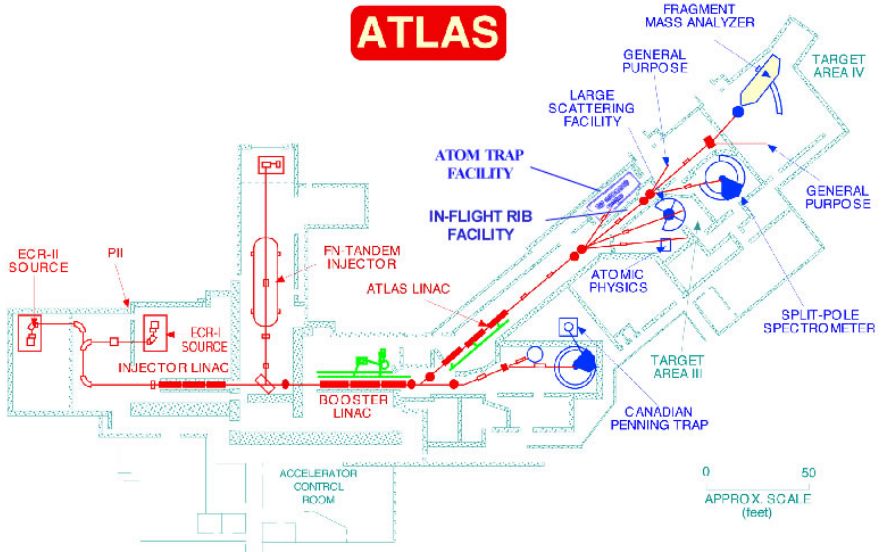


Figure 5.1.: Floorplan of the ATLAS accelerator complex. (taken from [Sav])

Ring no.	Polar angle θ	Ring no.	Polar angle θ
1	17.27	10	99.29
2	31.72	11	100.81
3	37.38	12	110.18
4	50.07	13	121.78
5	58.28	14	129.93
6	69.82	15	142.62
7	79.19	16	148.28
8	80.71	17	162.73
9	90.00		

Table 5.1.: The detectors of Gammasphere are ordered in rings of polar angle θ . (taken from [Lau])

For the purpose of the conducted Coulomb excitation experiments it was essential to place also a particle detector inside the target chamber as shown in fig. 5.3. The target is mounted on a movable ladder at the center of Gammasphere and the circular particle detector placed behind it. A double-sided silicon strip detector

(DSSD) in the shape of a CD with a total diameter of 96 mm and a hole of 48 mm in the middle is used. It is subdivided in 16 rings on the front, giving the θ angle of the scattered particles, and 16 wedges on the back for the azimuthal angle ϕ , respectively. In the chosen geometry with a distance $d=38.5\text{mm}$ between target and DSSD it covers a scattering angle ranging from $\theta = 31.9^\circ$ to 51.3° .

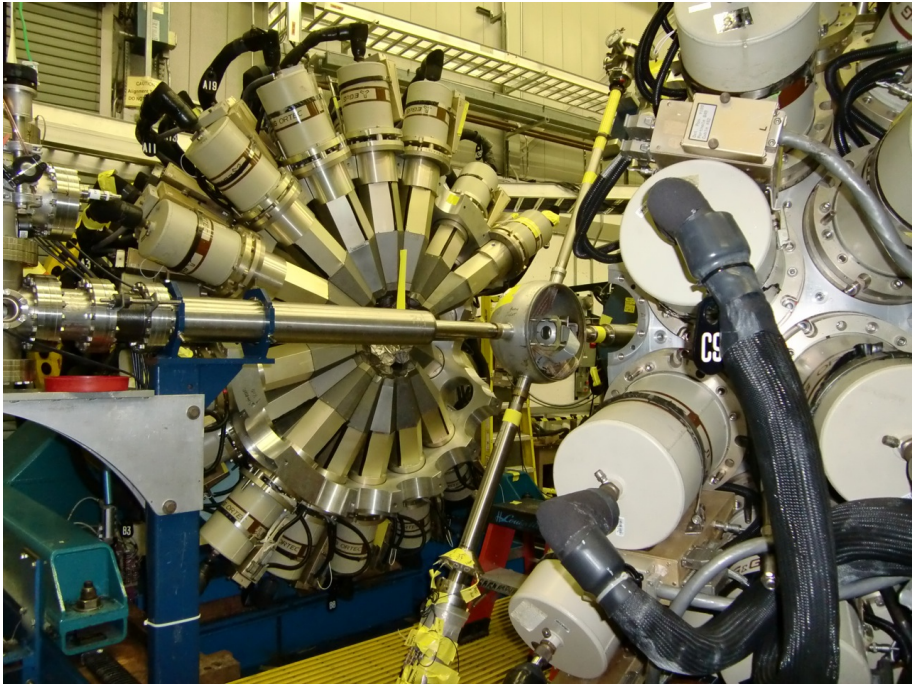


Figure 5.2.: The Gammasphere array is shown with its two hemispheres moved apart from each other and the opened target chamber in the middle. The beam is coming from the left.

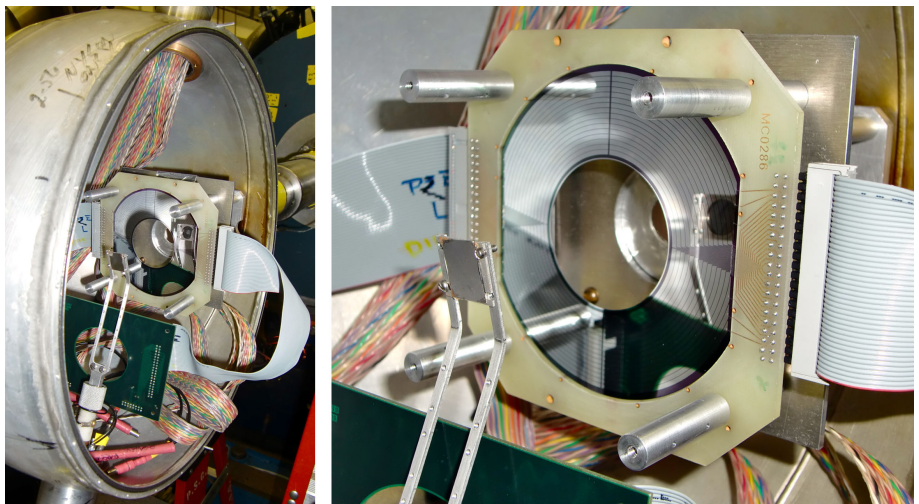


Figure 5.3.: The opened target chamber (left) and a close-up (right) show the setup with a fixed target position in front of the CD, a segmented, double-sided silicon-strip detector (DSSD).

5.2 REX-ISOLDE & MINIBALL

The European Organization for Nuclear Research, better known as CERN, is situated in the northwest suburbs of Geneva on the Franco-Swiss border. As the world's largest physics laboratory it consists of various facilities, one of it being ISOLDE, an on-line isotope mass separator, for experiments with radioactive ions. An overview of the main setup of beamlines and separators is given in the 3D sketch of fig. 5.4.

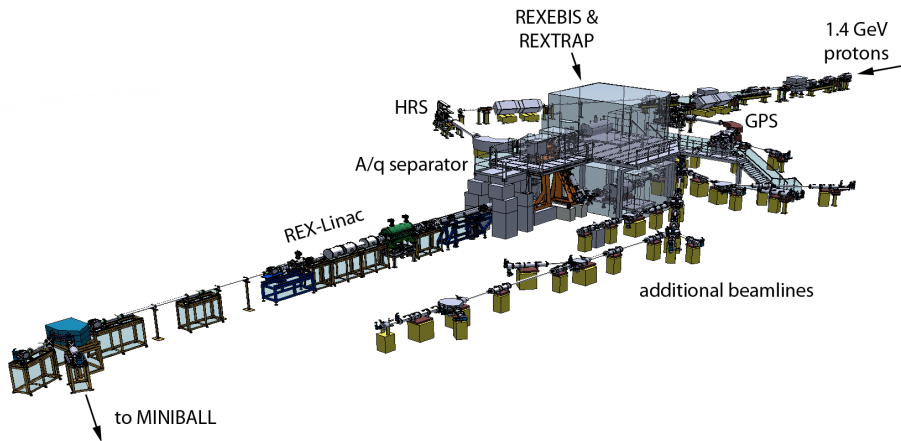


Figure 5.4.: Sketch of the main beam infrastructure of the ISOLDE facility at CERN. (3D drawing taken from [Iso])

5.2.1 Radioactive isotope production

At ISOLDE, radioactive nuclides are produced via spallation, fission, or fragmentation reactions in a thick target, irradiated with a pulsed proton beam from the PSB at an energy of 1.4 GeV and an intensity up to $2 \mu\text{A}$ on average. Pulses of up to 3×10^{13} protons can be delivered every 1-2 second. The target and ion source are fast physico-chemical devices. The volatile nuclear reaction products are released from the high temperature target into an ion source via chemically selective processes and are extracted as a radioactive ion beam. Laser ionization for selected chemical elements allows for further selection. This unique production device is coupled to two mass separators from which high intensity radioactive beams of high isotopic and often isobaric purity are extracted (comp. [Iso]).

Both isotope separators at ISOLDE are independent target-ion source systems that deliver 60 keV mass separated, single charged (1^+) radioactive ion beams. The General Purpose Separator (GPS) has one bending magnet and an electrostatic switchyard allowing the simultaneous extraction of three mass separated beams. The High Resolution Separator (HRS) consists of two bending magnets with an elaborate ion-optical system for higher order corrections. Both separators are connected to a common beamline system and feed the major experimental installations. Detailed information about the setup used for the presented experiments is summarized in tab. 5.2.

Isotope	^{140}Ba	^{142}Ba	^{140}Nd	^{142}Sm
Half-life	12.75d	10.7m	3.37d	72.4m
Year	2007	2007	2011	2012
Production target	#359	#359	#450	#479
Material	UC_x	UC_x	Ta	Ta
Ion source	Surface	Surface	RILIS	RILIS
Separator	HRS	HRS	HRS	GPS
Charge state	N/A	N/A	34+	34+
A/q	N/A	N/A	4.118	4.176
Beam energy	2.80MeV/u	2.80MeV/u	2.85MeV/u	2.85MeV/u

Table 5.2.: The list of produced isotopes for the relevant experiments shows the used devices and settings of the REX-ISOLDE facility.

The heart of ISOLDE is lying in its primary targets and ion sources. The production target should assure a fast liberation of the radioactive nuclei produced in large amounts of target material. In combination with the ion-source it produces an ion beam which preferably should only contain isotopes from one chemical element. The field of radiochemistry, which also involves metallurgy, high temperature chemistry and surface physics, determines the material and ion-source that has to be used for a certain beam. The ISOLDE group developed many different advanced target-ion-source combinations. The used target material is indicated in tab. 5.2 and two types of ion sources have been used in the presented experiments:

Surface Ion Source The surface ion source is a rather simple set-up for ionizing atoms (see fig. 5.5) produced in the target and was used to produce the Ba beams in 2007, more precisely BaF molecules. In the case of Barium the trick of starting with a molecular beam was used to suppress the strong contamination from Cs. A UC_x target was bombarded with the 1.4 GeV proton beam as usual but instead of Ba isotopes BaF^+ molecules were extracted

and cracked up at a later stage (see subsec. 5.2.2). In general the ionizer consists only of a metal tube, the so-called "line", for example tantalum or tungsten, which has a higher work function than the atom that should be ionized. Depending on the line's material it can be heated up to 2400°C.

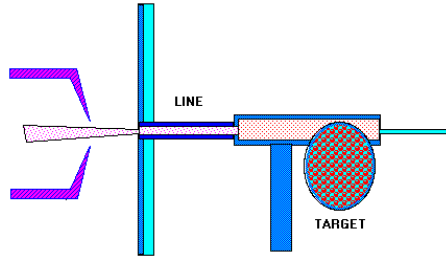


Figure 5.5.: Schematic view of the ISOLDE surface ion source. (picture taken from [Iso])

Resonance Ionization Laser Ion Source (RILIS) The RILIS [Fed08] creates ions inside a hot cavity surface ion source with the help of a laser system by an atomic physics technique: step-wise resonance photo-ionization. By exploiting the unique electronic structure of different atomic species the RILIS provides a rapid, efficient and highly Z-selective ionization process. This was exploited to produce the Nd and Sm beams in 2011/2012, where the ionization scheme was developed for the conducted experiments and the beams have been produced at ISOLDE for the first time. The target material was Tantalum. A sketch of the ion source is shown in fig. 5.6.

5.2.2 Post-acceleration

The post-accelerator complex REX-ISOLDE [Kes03] opens up new fields of research with radioactive ion beams of energies up to 3.0 MeV per nucleon. The REX section (see fig. 5.7) makes use of the variety of radionuclides that are extracted through the separators as explained in subsection 5.2.1. The singly-charged ions are first accumulated, bunched and cooled in a Penning trap, REXTRAP. The trap stores the ions during the breeding in the subsequent charge breeder. Bunches of ions are then transferred to an electron beam ion source, REXEBIS, where the ions are charge bred to a mass-to-charge ratio ≤ 4.5 . Finally, the ions are injected into a linear accelerator, the REX-Linac, via another mass separator. The aforementioned

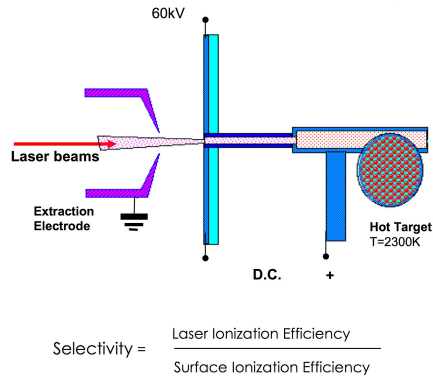


Figure 5.6.: Schematic view of the RILIS ion source. (picture taken from [Iso])

BaF^+ molecules were trapped in the REXTRAP and then cracked to proceed with Ba ions, which could be conventionally charge-bred in the REXEBIS.

REXTRAP In principle the ions are injected into a large Penning trap and slowed down by collisions with the atoms of a buffer gas (Neon or Argon). It accumulates, bunches and phase space cools the semi-continuous beam. For a typical 60 keV ISOLDE beam the energy loss in the buffer gas can be about 50 eV requiring a buffer gas pressure of 10^{-3} mbar. The trap efficiency varies between 40% and 60%. Bunching and accumulation of the semi-continuous radioactive beam is required to achieve an efficient ion injection into the EBIS. Furthermore, for the low-intensity radioactive beams it is advantageous to deal with bunches of particles instead of a continuous beam to increase the signal-to-background ratio in the experiments.

REXEBIS The Electron Beam Ion Source (EBIS) uses mono-energetic electrons from an electron gun to produce highly charged ions. The trapped low-charged ions will be stepwise ionized via electron impact until they are extracted when the outer barrier is lowered. This *charge-breeding* is necessary as the REX-Linac is designed to accelerate ions with a mass-over-charge ratio A/q of about 3.5 to 4.5. The REXEBIS delivers an electron current density of $\approx 150 \text{ A/cm}^2$ and electron beam currents of up to 0.4 A. The 1.5 m solenoid provides a trap length of 0.8 m with a magnetic field strength of 2 T. The electron beam energy is adjustable between 3 and 6 kV. Due to the fact that in the end only one specific charge state of the desired ions from the total

REX-ISOLDE

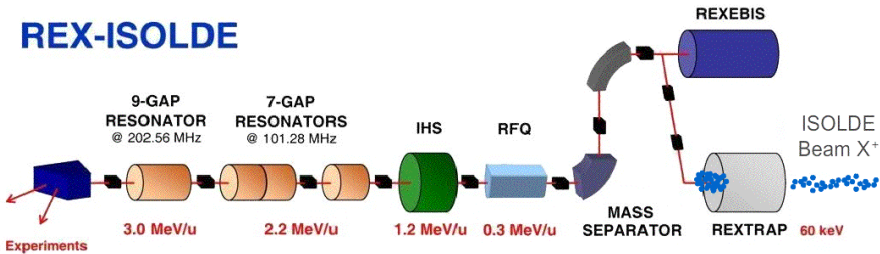


Figure 5.7.: Overview of the complete REX-ISOLDE setup [Iso].

charge state distribution from the EBIS is selected in the following A/q separator, the maximum breeding efficiency is about 30% in the $A \approx 140$ mass region. In contrast to the REXTRAP the EBIS requires a vacuum of better than 10^{-10} mbar. Despite the excellent vacuum inside the EBIS, the residual gas peaks, stemming from the buffer gas of the trap, can be of the same order of magnitude or even exceed the radioactive ion peaks.

A/q separator A mass separator is required, because the intensity of the radioactive ions extracted from the EBIS can be much smaller than the intensity of residual gas ions (Ne, Ar from REXTRAP and C, N, O, Ne, Ar from REXEBIS). A so-called Nier-spectrometer type is used, which consists of an electrostatic 90° cylinder deflector and a 90° magnetic bender arranged in a vertical S-shape. Analogous to GPS and HRS a A/q resolution of $\approx 1/150$ can be defined which helps to suppress the stable residual buffer gas ions, which are considered as a contamination of the radioactive beam of interest.

REX-Linac Different stages are used to accelerate the radioactive ions with the aim to deliver a pure and high-energetic beam to the experiments. In the first stage the ions are accelerated to 300 keV/u by a 4-rod radio-frequency quadrupole (RFQ) operated at 101.28 MHz. In order to match the beam from the RFQ into the acceptance of the IH (Interdigital-H-type)-structure a section of two magnetic quadrupole triplet lenses and a rebuncher is used. This feature of the REX-ISOLDE-IH resonator allows to vary the final energy between 0.8 and 1.2 MeV/u by adjusting the gap voltage distribution via two capacitive plungers and by adjusting the rf-power fed into the resonator. The lower final energy of the IH-structure is important for deceleration of the ions down to 0.8 MeV/u. Then the high-energy section (0.8 - 3.0 MeV/u) of the linac consists mainly of three 7-gap resonators. Each resonator has a

single resonance structure consisting of a copper half shell and three arms attached to both sides of the shell. All those structures are operated at 101.28 MHz and allow for acceleration of the ion beams up to 2.2 MeV/u. In 2004 an additional 9-gap IH structure, operating at a frequency of 202.56 MHz was installed in the high-energy section of the linac to finally provide ions up to 3.0 MeV/u.

The overall efficiency for trapping, beam transport, charge breeding and mass selection is normally between 5% and 15%. It is possible to handle sub-pA beams while the upper throughput limit is a few 10^9 ions per second. Refs. [Kes03; Iso] and references therein give a more detailed description of the REX-ISOLDE facility.

5.2.3 Gamma spectroscopy

For the detection of de-excitation γ rays the MINIBALL array [War13] is located at the target position behind the REX-Linac, see fig. 5.8. In contrast to Gammasphere (see sec. 5.1) it is a compact array, but mainly suited for the detection of events with low γ -ray multiplicities. MINIBALL consists of eight cluster detectors, each of them formed by three individually encapsulated six-fold segmented high purity germanium detectors. It covers about 2π of the solid angle in its standard configuration. The high granularity ($8 \times 3 \times 6 = 144$ segments) obtained by segmentation of the detectors is necessary to reduce the Doppler-broadening of γ rays emitted by nuclei with velocities of up to 10% of the speed of light.

For the detection and identification of particles an ancillary particle detector is required to determine the velocity of the γ -ray emitting nuclei. Therefore a double-sided silicon strip detector (DSSD) is mounted inside the MINIBALL target chamber in the shape of a compact disc (CD). The CD detector [Ost02], mounted in the target chamber in fig. 5.9, is a segmented DSSD device with an inner radius of 9.0 mm and an outer radius of 40.9 mm, composed of four separate quadrants. The front consists of 16 annular p+ strips per quadrant at 2 mm pitch, while the back consists of 24 sector n+ strips (wedges) at 3.5° pitch. The readout is usually done in such a way that 2 neighboring strips at the back are coupled together. This results in a total of $4 \times 16 \times 12 = 768$ pixels. Thereby information on the angular distribution of particles with a resolution of $\Delta\phi = 3.5^\circ$ and $\Delta\theta = 2.0^\circ$ can be extracted. In combination with the good energy resolution this is sufficient to account for the Doppler-shift broadening. The inter-strip distance ranges from $35 \mu\text{m}$ to $100 \mu\text{m}$. The total area of the CD detector is 5000 mm^2 , of which approximately 93% is active. The thickness of the silicon wafer can be different (between $50 \mu\text{m}$ and $1000 \mu\text{m}$) to measure either energy loss or total kinetic energy of the impinging particles.

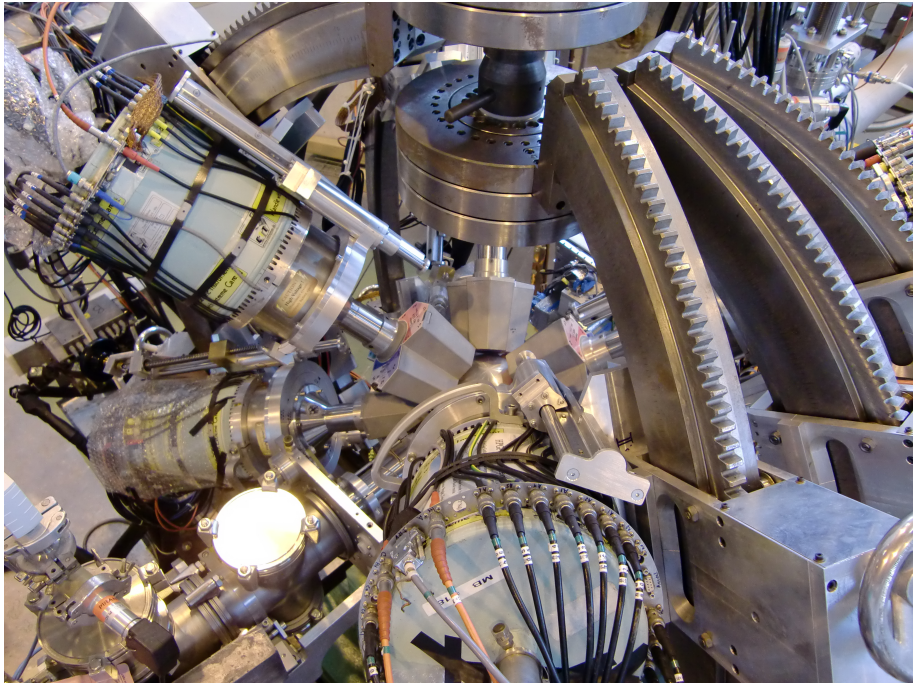


Figure 5.8.: Close-up view of the MINIBALL array from the top. The beam impinges from the left and all clusters are moved closely to the target chamber in the center (running condition).

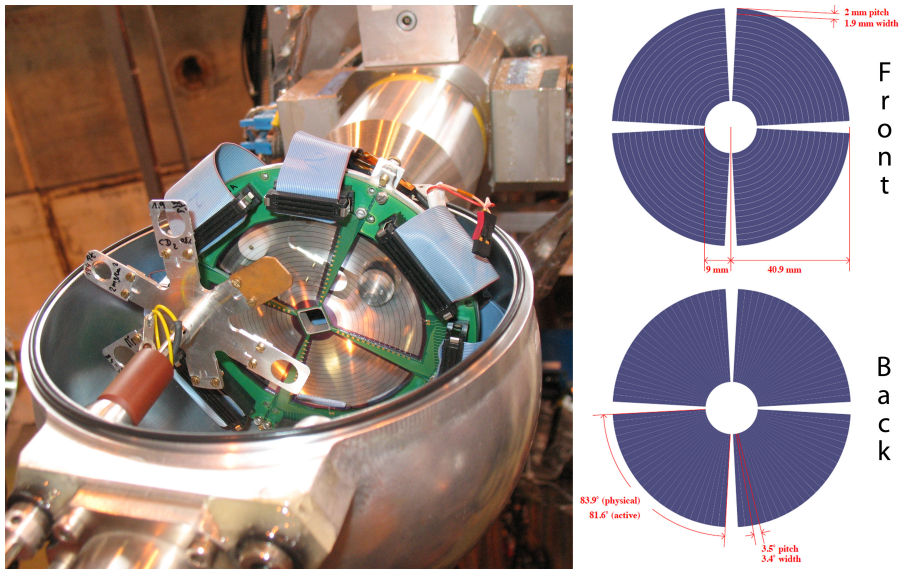


Figure 5.9.: The open target chamber with the mounted double-sided silicon strip detector (DSSD) is shown on the left, the sketch on the right showing the dimensions of the DSSD.

5.3 Conducted experiments

Experimental data was taken at the two described facilities at the Argonne National Lab (Sec. 5.1) and at CERN (Sec. 5.2). Beams of the rare stable isotopes $^{130,132}\text{Ba}$ with a natural abundance of approximately 0.1% were produced by the ATLAS facility at ANL in the week from 9/26/11 to 10/3/11. The measurements with the radioactive isotopes ^{140}Ba ($T_{1/2}=12.75\text{d}$), ^{142}Ba ($T_{1/2}=10.7\text{m}$) and ^{140}Nd ($T_{1/2}=3.37\text{d}$) as well as ^{142}Sm ($T_{1/2}=72.4\text{m}$) took place at the REX-ISOLDE facility at CERN. The experiments with the Barium isotopes were conducted from 7/26/07 to 7/31/07 while Nd was measured from 7/1/11 to 7/4/11 and Sm from 6/28/12 to 6/30/12.

Projectile	Target		Energy [MeV]	Coulomb barrier	Aim
	Isotope	Thickness [mg/cm ²]			
^{130}Ba	^{12}C	0.495	444	82%	MSS
	^{94}Mo	0.462	444	76%	Q moment
	^{94}Mo	0.462	238	41%	Q moment
^{132}Ba	$^{12}\text{C} + \text{Ta}$	0.45 + 29.0	444	82%	complem. DSAM
	^{12}C	0.495	444	81%	MSS
	^{94}Mo	0.462	554	94%	Q moment
^{140}Ba	^{94}Mo	0.462	234	40%	Q moment
	^{96}Mo	0.9	392	66%	B(E2) + Q moment
^{142}Ba	<i>nat</i> Cu	1mm	392	70%	complem. DSAM
	^{96}Mo	0.9	398	67%	Q moment
^{140}Nd	^{48}Ti	1.4	399	68%	B(E2)
	^{64}Zn	1.55	399	64%	B(E2)
^{142}Sm	^{48}Ti	1.4	405	66%	B(E2)
	^{94}Mo	2.0	405	60%	B(E2)

Table 5.3.: The list of conducted experiments covers all Coulomb excitation experiments with participation of the author that are referred to in this work.

For $^{130,132}\text{Ba}$ different measurements were performed. A thin ^{12}C target of 0.495 mg/cm² was chosen to identify high-lying 2^+ states on the quest for mixed-symmetric states [PBL08]. These data sets are analyzed in a different thesis [Mö13] but spectroscopic data from their analysis is used in the analysis of this work. The data sets with a 0.462 mg/cm² thick ^{94}Mo target were taken at two different energies for each of the both isotopes to disentangle the interference effect

on the quadrupole moment. An additional run with the ^{130}Ba beam was performed to measure lifetimes of excited states in the picosecond range, especially of the 2_2^+ state, with the DSAM technique.

The radioactive nuclei $^{140,142}\text{Ba}$ were Coulomb excited on a 0.9 mg/cm^2 thick target of ^{96}Mo , while for ^{140}Ba also a complementary DSAM measurement was performed with a 1 mm thick target of ^{nat}Cu . The aim was to measure the $B(E2; 2_1^+ \rightarrow 0_1^+)$ values and the quadrupole moments $Q(2_1^+)$ of both isotopes. The ^{140}Nd beam was impinging on 2 different targets for Coulomb excitation (^{48}Ti with 1.4 mg/cm^2 and ^{64}Zn with 1.55 mg/cm^2) to determine the transition strength $B(E2; 2_1^+ \rightarrow 0_1^+)$. For the same reason ^{142}Sm was investigated via scattering on ^{48}Ti with 1.4 mg/cm^2 and ^{94}Mo with 2.0 mg/cm^2 .



6 Data analysis and results

The analysis of all the conducted experiments is presented in this chapter. The first three sections about the kinematics, Doppler correction, efficiency calibration and the software APCAD are of general character and relevant for all experiments. In the following sections 6.4 to 6.6 the particular analyses of the individual experiments are presented including the final results.

6.1 Kinematics and Doppler correction

A crucial point in Coulomb excitation experiments with heavy ions is the correct description of the kinematics and the related Doppler correction. Especially in inverse kinematics, which was used in all presented experiments, the twofold solution for the projectile angles has to be considered. The reaction ($^{142}\text{Sm} \rightarrow ^{94}\text{Mo}$) of the last MINIBALL experiment (see sec. 5.2 and sec. 6.6) in 2012 serves as an example in this section to illustrate the kinematics including particle identification as well as the Doppler correction.

The mathematical description of the process is based on the concept of (in)elastic collision of two bodies in classical mechanics [LLZ97]. The collision of two particles is elastic as long as the total kinetic energy is conserved. The presented Coulex experiments cannot be considered as completely elastic collisions because in the excitation process a small amount of the total kinetic energy is transferred to a nucleus as excitation energy ΔE of the Coulomb excited state. This corresponds to a small Q value in the terminology of inelastic collisions and the energy conservation can be written as

$$\frac{1}{2}m_1v_1^2 + \frac{1}{2}m_2v_2^2 = \frac{1}{2}m_1v_1'^2 + \frac{1}{2}m_2v_2'^2 + \Delta E. \quad (6.1)$$

The indices 1 and 2 indicate the variables for projectile and target respectively, the prime denotes the quantities after collision. Obviously the target nuclei are at rest before the collision and therefore the conditions are $v_1 > 0$, $v_2 = 0$ and afterwards $v_1' > 0$, $v_2' > 0$. The restriction $m_1 > m_2$ defines inverse kinematics.

The initial kinetic energy E of the projectiles is equivalent to the beam energy in the laboratory system but the kinetic energy E' of the projectiles after collision is smaller than the total kinetic energy $E - \Delta E$ after collision because substantial kinetic energy is transferred to the (recoiling) target nucleus as well [AW75]:

$$E = \frac{1}{2}m_1v_1^2 \quad (6.2)$$

$$E' = \frac{1}{2}m_1v_1'^2 = \frac{A_2}{A_1 + A_2} (1 + \tau^2 + 2\tau \cos\vartheta) \cdot (E - \Delta E(1 + A_1/A_2)) \quad (6.3)$$

$$\text{with } \tau = \frac{A_1}{A_2} \sqrt{\frac{E}{E - \Delta E(1 + A_1/A_2)}} \quad (6.4)$$

$$\sin \theta_{1,max} = \frac{1}{\tau} \approx \frac{A_2}{A_1} \quad (6.5)$$

The kinetic energy E' after collision is depending unambiguously on the scattering angle ϑ in the center-of-mass system. The calculated energy dependence of projectile and target nuclei on the scattering angles in the laboratory system are shown

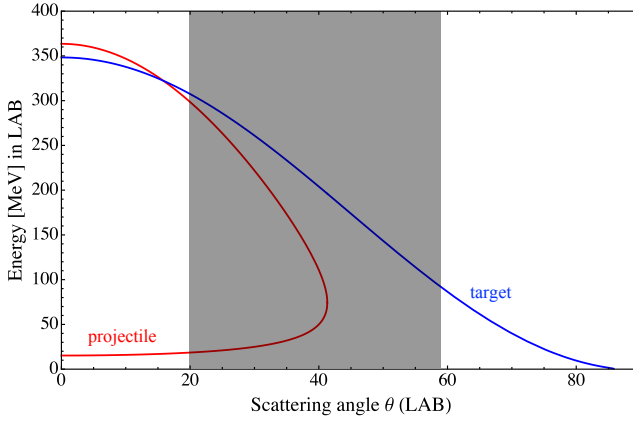


Figure 6.1.: Energy dependence of projectile and target nuclei on the scattering angle θ . The shaded area indicates the coverage of the circular particle detector in experiment IS496 (part 2) as described in sec. 6.6.

in fig. 6.1. The maximum scattering angle $\theta_{1,max}$ of the projectiles in inverse kinematics is given in the endmost formula with the approximation of elastic scattering ($\Delta E = 0$).

For the analysis of experiments one is interested in the kinematical reconstruction of the scattering angles, *e.g.*, if one particle is observed but the collision partner has not been detected. The Coulomb excitation process as well as the energies (velocities) of the particles are strongly depending on the scattering angles and so their determination is important for the Doppler correction to ensure clean spectra. The scattering angles θ_1, θ_2 in the laboratory system are connected with the scattering angle ϑ in the center-of-mass system through the following relations [AW75]. The formulas are given for the elastic case ($\Delta E = 0$) because the effect of the energy loss on the angles is small:

$$\frac{\sin(\vartheta - \theta_1)}{\sin \theta_1} = \frac{A_1}{A_2} \quad (6.6)$$

$$\frac{\sin(\pi - \vartheta - \theta_2)}{\sin \theta_2} = 1 \quad (6.7)$$

To identify the scattered particles on the used circular (CD) detector the kinematics has to be considered. The following mutual dependence of the polar scattering angles $\theta_{1,2}$ can be derived by eliminating ϑ :

$$\tan \theta_1 = \frac{\sin(2\theta_2)}{A_1/A_2 - \cos(2\theta_2)} \quad (6.8)$$

$$\cos \theta_2 = \frac{\cos \theta_1}{A_2} \sqrt{\frac{1}{2}(A_2^2 + A_2(A_1 + A_2)) \tan^2 \theta_1 - \sqrt{A_2^4 + (A_2^4 - A_1^2 A_2^2) \tan^2 \theta_1}} \quad (6.9)$$

The dependence of the target scattering angle θ_2 on the angle of the projectile θ_1 is ambiguous. There are two branches and in eq. 6.9 the "higher branch", corresponding to higher energy and a larger cross-section, is considered. The mutual dependence of the scattering angles θ_1 and θ_2 of projectile and target is shown in fig. 6.2.

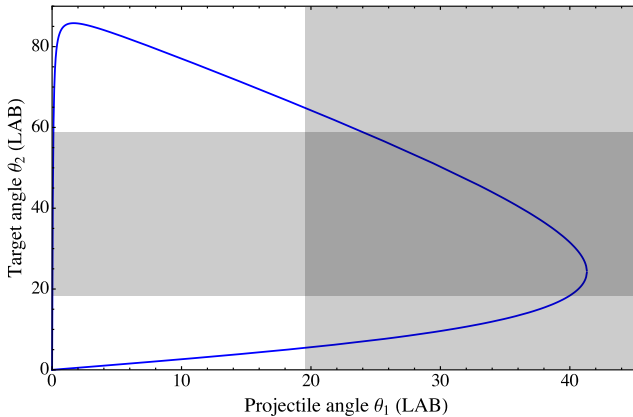


Figure 6.2.: The dependence of the target scattering angle θ_2 on the projectile scattering angle θ_1 is plotted with the shaded areas showing the coverage of the circular particle detector in experiment IS496 (part 2) described in sec. 6.6.

The velocities of projectile and target nuclei after collision in inverse kinematics can be written in a convenient way depending on the target scattering angle θ_2 because the ambiguity vanishes for this case [LLZ97; AW75]:

$$v'_1 = v_1 \sqrt{1 - \frac{4(A_2/A_1)}{(1 + (A_2/A_1))^2} \cos^2 \theta_2} \quad (6.10)$$

$$v'_2 = v_1 \frac{2A_1}{A_1 + A_2} \cos \theta_2 \quad (6.11)$$

$$(6.12)$$

If γ -rays from Coulomb-excited states ought to be measured a Doppler correction is necessary. This is due to the fact that for the used energies the excited particles move with velocities of 5-10% of the speed of light. That causes a shift in the observed γ -ray energies depending on the polar angle θ of the Germanium detectors because the γ radiation is emitted in flight. The velocities can be defined as fractions of the speed of light $\beta = v/c$.

$$E_{unshifted} = f_{corr} \cdot E_{shifted} \quad (6.13)$$

$$f_{corr} = \frac{1 - \beta \cos \vartheta}{\sqrt{1 - \beta^2}} \quad (6.14)$$

$$\beta_{beam} = \bar{\beta} \sqrt{1 - 4 \frac{A_1}{A_2} \frac{\cos^2 \theta_2}{(1 + A_2/A_1)^2}} \quad (6.15)$$

$$\beta_{target} = \bar{\beta} \frac{2A_1}{A_1 + A_2} \cos \theta_2 \quad (6.16)$$

In this case ϑ is the angle between the direction of motion of the emitting nucleus and the γ ray for which the energy correction is calculated. Given the angles of the moving nucleus (θ_n, ϕ_n) and the detected γ ray ($\theta_\gamma, \phi_\gamma$) it is calculated via

$$\cos \vartheta = \cos \theta_n \cos \theta_\gamma + \cos(\phi_n - \phi_\gamma) \sin \theta_n \sin \theta_\gamma. \quad (6.17)$$

The velocity $\bar{\beta}$ indicates an average β for $\theta_1 = 0$ at the beam energy, taking into account the energy loss in the target. The further dependence stemming from the scattering angle and mass numbers of the collision partners is taken into account by the main terms in the above formulas.

6.2 Efficiency calibration

Germanium semiconductor detectors possess an intrinsic efficiency for the detection of γ rays. This energy-dependent property, influenced by the material and geometry of the detector, has to be calibrated in order to be able to compare peaks of γ -ray transitions in size at various energies. Due to the fact that Gammisphere as well as MINIBALL consist of high-purity germanium detectors both spectrometers can be treated together here. For the conducted Coulex experiments spectra of the whole arrays are analyzed and subdivided by the scattering angle of the particles, detected on the CD. That's why an overall efficiency curve of the complete array of detectors is sufficient for the analysis. In the case of the DSAM analysis a curve per ring (Gammisphere) and per crystal (MINIBALL), respectively, is determined to make use of the angular connection between the spectra provided by APCAD [Sta13]. In the analysis of the Coulex experiments the size of peaks is always compared to each other or normalized to a peak of known cross-section. Therefore the determination of a relative efficiency curve is sufficient. The same is true for the DSAM analysis where just the ratio between the spectra of different angle has to be known.

One standard source for calibration is ^{152}Eu because this isotope decays with several γ rays of known relative intensities between 121 and 1408 keV. As can be seen in fig. 6.3 it can be also extrapolated above 2 MeV due to the flat behavior of the efficiency curve at higher energies. This well reproduced energy range covers all relevant γ -ray energies of the experiments with $^{130,132}\text{Ba}$, so it was the only taken calibration measurement. To fit the data points a phenomenological function with 3 parameters a , b and c of the the following form is used:

$$\epsilon(E) = a \cdot \exp(-b \cdot \ln(E - c)) \quad (6.18)$$

The statistical, correlated error of the fit is shown in the graph as a gray shaded area behind the efficiency curve. It lies around 1% or less in the energy range of interest.

At MINIBALL it can be important to describe also the low-energy range between 0 and 100 keV, where the curve bends down, with good precision. There can be X-rays from the isotope of interest or from contaminants what makes it necessary to determine the size of the X-rays to identify the amount of contamination. For $^{140,142}\text{Ba}$ a calibration measurement with ^{152}Eu was performed (similar to the Gammisphere experiments) while in the case of ^{140}Nd and ^{142}Sm a source of ^{152}Eu and ^{133}Ba was placed at target position for the calibration measurement. The advantage of the additional ^{133}Ba source is based on a data point at 81 keV (see fig. 6.4) and more prominent data points between those of the ^{152}Eu source in the interesting region around 1000 keV that can be useful in the analysis as explained above.

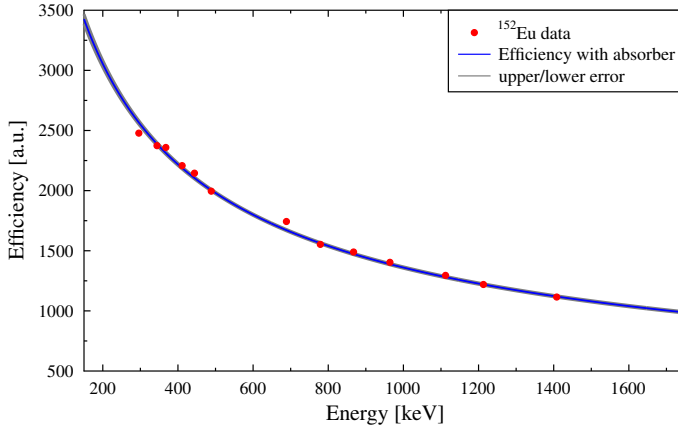


Figure 6.3.: Efficiency curve of the Gammasphere spectrometer, setup for the runs $^{132}\text{Ba} \rightarrow ^{94}\text{Mo}$ at 554 MeV, a thin absorber mounted in front of the CD. The error of the data points is smaller than the size of the points.

For the fit of the data points a more flexible function is needed and defined phenomenologically as a sum of logarithmic functions with 5 parameters:

$$\epsilon(E) = a + b \cdot \ln E + c \cdot (\ln E)^2 + d \cdot (\ln E)^3 + e \cdot (\ln E)^4 \quad (6.19)$$

Again, the statistical, correlated error of the fit is shown in the graph as a gray shaded area behind the efficiency curve. It lies around 1% or less from approximately 300 keV onwards but the fit is less accurate around the bending point. Furthermore the choice of the function also influences the position of the bending point to some extent and thereby the uncertainty for the low-energy range is even larger than the statistical error of the fit indicates.

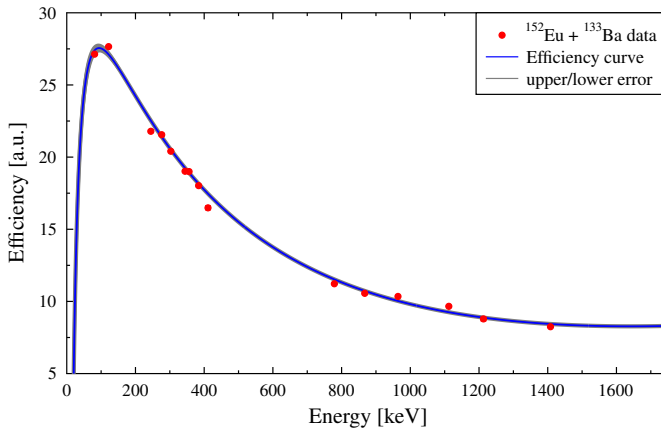


Figure 6.4.: Efficiency curve of the full MINIBALL array, setup of 2011 for the runs with ^{140}Nd on ^{48}Ti and ^{64}Zn at 392 MeV. The error of the data points is smaller than the size of the points. The error increases around the "bending point" of the curve around 100 keV.

6.3 Software APCAD

The data analysis of this work is handled with the software framework ROOT [BR97], that is based on C++ and has been developed at CERN. For the Coulomb-excitation calculations CLX and GOSIA are used as described in sec. 4.4. However, a dedicated software is used for the determination of lifetimes with the Doppler-shift attenuation method (DSAM). The software package APCAD [Sta13] is based on ROOT and provides necessary features for this kind of analysis going beyond the analysis of former DSAM experiments [Sta11].

This new approach for DSAM analyses enhances the sensitivity, effectivity and applicability of the DSA method [Sta11]. It takes advantage of the capabilities of newly developed detector systems for γ radiation like the 4π HPGe arrays AGATA [Akk12] and GRETA [Del99]. The spatial resolution achievable with those devices allows for the exact determination of the polar angle θ_γ of γ quanta in the laboratory system. As a result, spectra of the transition radiation that are almost continuous in energy and polar angle can be obtained. The analysis of these two-dimensional spectra represents an advancement of the established DSA method which is based on the analysis of one-dimensional spectra recorded under discrete detector positions and averaged over the solid angle covered by the detectors. Analysis programs for the conventional method are available and widely in use, like the FORTRAN code LINESHAPE [WJ91] that was developed in the early 90's, for example. Fits of the lineshapes in the energy-angle space, that simultaneously contain information collected under all polar angles covered by the detector array, promise a significant improvement of the accuracy of the lifetimes obtained. Furthermore APCAD provides an extension of the applicability to cases that were not accessible by the conventional analysis due to non-trivial contaminant lineshapes or low statistics. The capability to determine it also from spectra with low statistics is of major interest especially for experiments with weakly intense, radioactive ion beams and/or reactions with low excitations probabilities for the desired states (comp. [Sta11]).

As a major improvement to other DSAM analysis tools in APCAD the influence of uncertainties of the stopping powers on the extracted lifetime is quantified in a consistent way. The stopping matrices describing the Coulomb excitation and slowing-down process of the heavy ions in the target are calculated from a Monte-Carlo simulation based on the GEANT4 framework [Ago03] using the stopping powers from [G4m] and [Icrb; Icra]. For the presented results (see subsecs. 6.4.1 and 6.5.1) the stopping powers have been varied by $\pm 5\%$ for the electronic stopping and $\pm 20\%$ for the nuclear stopping, thus reflecting their increasing uncertainty at low ion velocities.

The γ -ray spectrometers used in the experiments of this work (Gammasphere and MINIBALL, secs. 5.1 and 5.2) belong to the so-called 2nd generation of Germanium detector arrays compared to the 3rd generation device AGATA [Akk12]. Although they don't provide continuous-angle γ -ray spectra they cover a wide range of discrete angles either ordered in rings of polar angles (Gammasphere) or by specific positions of the detector cores (MINIBALL). This allows for the exploitation of the angular information in the APCAD software by not fitting individual spectra separately but connecting them via the angular distribution of the investigated transition. It is used for the analysis of the experimental data in this work (see subsecs. 6.4.1 and 6.5.1).

6.4 Stable isotopes ^{130,132}Ba

The major aim of the analysis presented in this section is the determination of spectroscopic quadrupole moments $Q(2_1^+)$ of ^{130,132}Ba. Ions of both isotopes were Coulomb excited in four subsequent runs on a 0.462 mg/cm² ⁹⁴Mo target at two different energies for each isotope in order to disentangle the interference effect on the quadrupole moment.

The cross-section $\sigma_{2_1^+}$ of the Coulomb excitation of a 2_1^+ state with quadrupole moment $Q = 0$ ($M_{22} = 0$) depends (in a simple picture without higher-lying states) solely on the transitional matrix element M_{20} and $\sigma_{2_1^+} = \sigma_{2_1^+}(M_{20})$. If the 2_1^+ state has an average deformation and therefore a nonzero quadrupole moment, the cross-section also depends on the diagonal matrix element and $\sigma_{2_1^+} = \sigma_{2_1^+}(M_{20}, M_{22})$. This dependence is used in all presented experiments to determine the quadrupole moment as explained in section 4.2. In reality many higher-lying states can feed the 2_1^+ state from above and thereby influence its population. The cross-section $\sigma_{2_1^+}$ becomes $\sigma_{2_1^+}(M_{20}, M_{22}, M_{ij}, M_{ii}, \dots)$. While the most important matrix elements connecting the 4_1^+ and 2_2^+ to the 2_1^+ state are known (or have been measured independently) for ^{130,132}Ba, there is another free variable. The sign of the matrix elements is not fixed and can be chosen. There is no change in the cross-section if one changes the sign of the transitional matrix elements within a band but the sign of the inter-band matrix elements has an effect on $\sigma_{2_1^+}$. This shall be explained in detail for the most important case of the 2_2^+ state. It is helpful to introduce the interference term

$$P_3(2_1^+) = \langle 0_1^+ || M(E2) || 2_1^+ \rangle \langle 2_1^+ || M(E2) || 2_2^+ \rangle \langle 0_1^+ || M(E2) || 2_2^+ \rangle, \quad (6.20)$$

which can be either positive (constructive interference) or negative (destructive interference). This loop of the transitional matrix elements through the 0_1^+ , 2_1^+ , 2_2^+ states as illustrated in fig. 6.5 determines the character of the interference. By convention in the ground band $\langle 0_1^+ || M(E2) || 2_1^+ \rangle$ is chosen to be positive and if one defines $\langle 0_1^+ || M(E2) || 2_2^+ \rangle$ to be positive as well it is decided by the sign of $\langle 2_1^+ || M(E2) || 2_2^+ \rangle$ if the loop becomes positive or negative. The cross-section $\sigma_{2_1^+}$ can now be expressed as $\sigma_{2_1^+}(M_{20}, M_{22}, \text{sgn}(P_3(2_1^+)))$. The transitional matrix elements $\langle 2_1^+ || M(E2) || 2_2^+ \rangle$ and $\langle 0_1^+ || M(E2) || 2_2^+ \rangle$ of the 2_2^+ are important as well, but as long as the magnitude is known a small change doesn't have a big effect on $\sigma_{2_1^+}$.

As already Larsen et al. [Lar72] state, the extraction of $Q(2_1^+)$ in a standard Coulomb excitation experiment is hindered by the unknown sign of the interference term due to Coulomb excitation of the 2_1^+ state via the 2_2^+ state. This is the reason why the latest measurements of electric quadrupole moments for the stable Barium

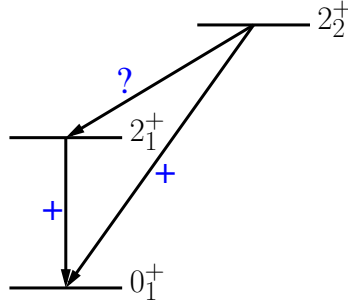


Figure 6.5.: The sign of the product of the transitional matrix elements building the loop through the $0_1^+, 2_1^+, 2_2^+$ states determines the interference.

isotopes $^{130,134,138}\text{Ba}$ by Burnett et al. [Bur89] result in two possible values for the quadrupole moments including even changes in sign and magnitude in the case of $^{134,138}\text{Ba}$ (see fig. 7.1). The ambiguity in the Barium chain becomes most distinct for the case of ^{130}Ba , where $Q(2_1^+) = -1.02(15)$ (constructive interference) or $Q(2_1^+) = -0.09(15)$ (destructive interference) [Bur89]. There was no measurement for ^{132}Ba .

As the calculations show (see fig. 6.6) the effect of changing the interference term $P_3(2_1^+)$ on the cross-section σ of the 2_1^+ state is smaller than the effect of changing the quadrupole moment at lower energy. The shown energy-dependent functions of the cross-sections are expressed as relative changes $R(E)$ of the Coulex cross-sections σ of the 2_1^+ state:

$$R_{interf}(E) = 1 - \frac{\sigma_{2_1^+}(E, P_3(2_1^+) < 0, M_{22} = 0\text{eb})}{\sigma_{2_1^+}(E, P_3(2_1^+) > 0, M_{22} = 0\text{eb})} \quad (6.21)$$

$$R_{sgn(Q)}(E) = 1 - \frac{\sigma_{2_1^+}(E, P_3(2_1^+) > 0, M_{22} = -1.0\text{eb})}{\sigma_{2_1^+}(E, P_3(2_1^+) > 0, M_{22} = +1.0\text{eb})} \quad (6.22)$$

At higher energy, corresponding to approximately 80% of the Coulomb barrier, both effects (change of sign of quadrupole moment $R_{sgn(Q)}(E)$ or interference term $R_{interf}(E)$) are comparable. With the help of the low-energy measurement a single value for the quadrupole moment can be determined with a large uncertainty because here the influence of the interference term is small (not much excitation of 2_2^+) but the statistics will be low. The high-energy measurement will result in two

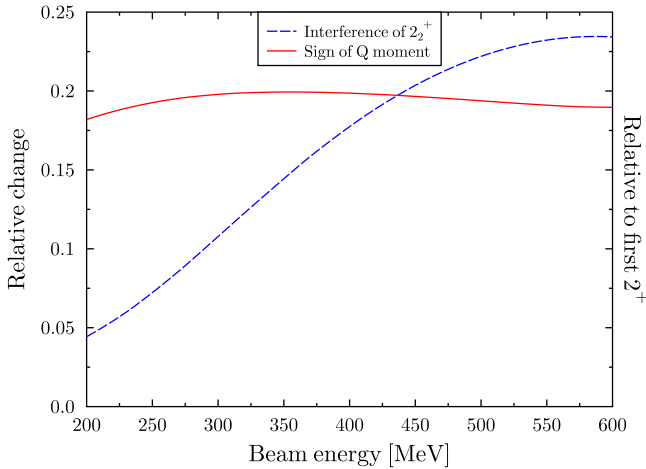


Figure 6.6.: The relative influence of changing the sign of either the interference term $P_3(2_1^+)$ or the quadrupole moment of the 2_1^+ state on $\sigma(2_1^+)$ is calculated with CLX depending on the beam energy. The parameters are chosen for the $^{132}\text{Ba} \rightarrow ^{94}\text{Mo}$ reaction and the cross-sections are integrated over the scattering angles covered by the particle detector.

quadrupole moments depending on the interference term. One of the two results should agree with the measurement at low energy and so the sign of the interference term is fixed by the comparison of both measurements. Furthermore the high-energy data improves the accuracy of the measured value of Q . The analysis showed (see subsec. 6.4.2) that even with the high-energy data exclusively, it is possible to determine the sign of the interference term $P_3(2_1^+)$ due to the different χ^2 values of the fits for a different combination of signs of the matrix elements. With the fixed sign of the interference term it is also possible to interpret the ambiguous data on quadrupole moments for the Barium isotopes (compare [Bur89] and references therein) in a conclusive way.

In a fifth experimental run the missing spectroscopic information of ^{130}Ba , more precisely the lifetime of the 2_2^+ state, was determined employing the DSAM technique (see sec. 4.5). The beam with an energy of 444 MeV was impinging on a target consisting of two layers, a 0.45 mg/cm^2 ^{12}C layer for Coulomb excitation followed by a 29 mg/cm^2 Ta layer to stop the Ba ions of the beam. During the stopping process the measured energies of the de-excitation γ rays of transitions in the Coulomb-excited ^{130}Ba ions are Doppler shifted resulting in a characteris-

tic lineshape of the photopeak. This allows for a lifetime analysis as described in subsection 6.4.1.

The Gammasphere array was used in all runs with exactly 100 of its Compton-shielded single-crystal HPGe detectors for γ -ray detection. They were mounted in their regular setup of 16 rings with different polar angles θ as summarized in tab. 6.1. No detectors were mounted in ring no. 1 due to the prolongation of the beampipe towards the fragment mass analyzer (FMA) although this device was not used in the experiment. The ring-wise order allows to sum up the γ -ray spectra of all detectors belonging to the same ring. This is especially useful for the determination of angular distributions and, therefore, for the DSAM analysis presented in the next subsection.

Ring no.	Polar angle θ	Ring no.	Polar angle θ
2	31.72	10	99.29
3	37.38	11	100.81
4	50.07	12	110.18
5	58.28	13	121.78
6	69.82	14	129.93
7	79.19	15	142.62
8	80.71	16	148.28
9	90.00	17	162.73

Table 6.1.: The available rings of Gammasphere with detectors during the $^{130,132}\text{Ba}$ runs are given with ring numbers and polar angle θ . (taken from [Lau])

In the case of the ^{94}Mo target, the projectile- and target-like recoil ions were detected in forward direction in coincidence with the emitted γ rays on the DSSD with an opening angle of $\theta = 31.9^\circ - 51.3^\circ$ (see fig. 5.3). Preliminary results from these data sets can be found in ref. [Bau12a].

6.4.1 DSAM measurement of ^{130}Ba

The analysis applying the Doppler-shift attenuation method (DSAM) technique allowed to deduce the lifetime of the 2_2^+ state of ^{130}Ba from a simultaneous DSAM fit to the 16 energy spectra (stemming from the 16 rings) using the newly developed program package APCAD [Sta13], introduced in sec. 6.3.

As a first step the stopping matrix is calculated from a Monte Carlo simulation. The stopping powers have been varied by $\pm 5\%$ for the electronic stopping and $\pm 20\%$ for the nuclear stopping as explained in sec. 6.3. The resulting velocity

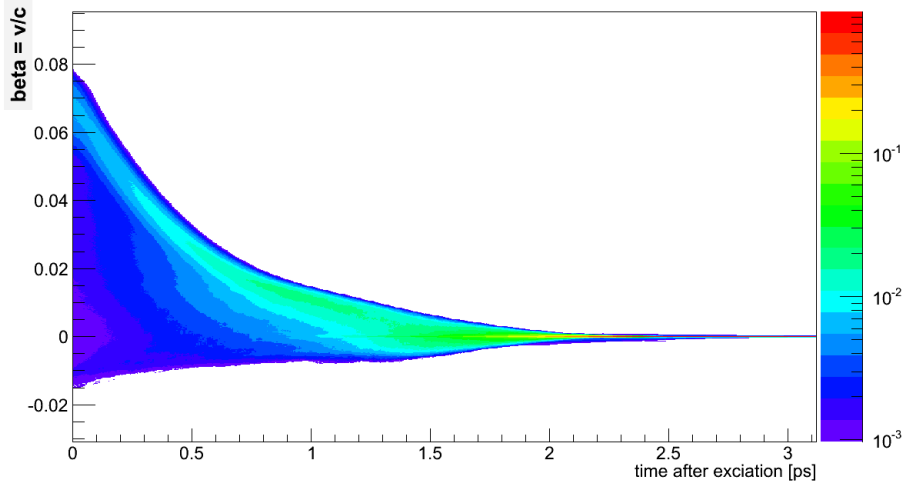


Figure 6.7.: The velocity distribution of the ^{130}Ba ions for $\theta_\gamma = 31.72^\circ$, based on the simulated stopping matrices, is visualized with the help of APCAD.

distribution for ring no. 2 under $\theta_\gamma = 31.72^\circ$ is illustrated in fig. 6.7. The effect of back-scattered beam particles is visible by the appearance of events with negative velocity β . This happens when the ^{130}Ba ions are scattered in the beginning of the 2nd layer, in which the mass number of Ta ($A=181$) is larger than the mass of the beam particles.

Examples for DSAM fits for one ring in forward and one ring in backward direction are shown in fig. 6.8 for the $2_2^+ \rightarrow 0_1^+$ transition. This transition is well-suited for a DSAM fit because it is nicely separated from other peaks in the spectrum. From the global fit the lifetime was obtained:

$$\tau_{2_2^+}(^{130}\text{Ba}) = 6.63 \begin{matrix} (+0.04) \\ (-0.04) \end{matrix}_{\text{stat}} \begin{matrix} (+0.18) \\ (-0.39) \end{matrix}_{\text{sys}} \text{ ps} = 6.63^{+0.18}_{-0.39} \text{ ps} \quad (6.23)$$

The systematic uncertainties stemming from the stopping power uncertainties clearly dominate the uncertainty of the final result. The lifetime corresponds to a transition strength of $2.08^{(+0.13)}_{(-0.06)}$ W.u. This is in fair agreement with the evaluation of the $^{130}\text{Ba} \rightarrow ^{12}\text{C}$ Coulex run of the same experimental campaign, whose analysis [Möl13] gives $3.14^{(+0.48)}_{(-0.66)}$ W.u. With respect to the known statistical and systematic errors the discrepancy may hint to hidden systematic errors, which have not been identified yet. The Coulex analysis translates into a lifetime of 4.44 ps. The corresponding lineshape is drawn in fig. 6.8 for comparison.

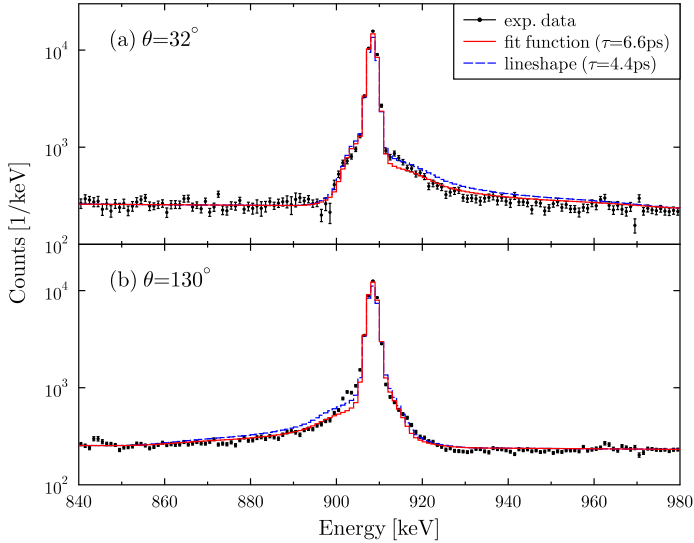


Figure 6.8.: The Doppler-broadened lineshapes of the $2_2^+ \rightarrow 0_1^+$ transition at 908 keV in ^{130}Ba for detector rings of (a) 32° and (b) 130° are shown after background-subtraction. The spectra are shifted by +200 counts per channel for better visibility on the logarithmic scale. The full fits are represented by solid (red) lines, while for comparison the resulting lineshape with an assumed lifetime of 10.3 ps is indicated by a dashed (blue) line.

6.4.2 Reorientation technique

The analysis of Coulex yields of the runs with ^{130}Ba and ^{132}Ba at two different beam energies, always bombarding the thin ^{94}Mo target, allows to determine the quadrupole moment $Q(2_1^+)$ for both isotopes. The idea behind this Coulex reorientation analysis is explained in sec. 4.2 and in more detail at the beginning of this section.

Figures 6.9 and 6.10 show the γ -ray spectra of the complete Gammasphere array with Doppler-correction for the Coulomb-excited $^{130,132}\text{Ba}$ projectiles (top) and ^{94}Mo target recoils (bottom) in coincidence with the particle signals from the DSSD. Both figures display results from the high-energy runs. The distribution of hits on the CD is very similar for both experiments due to the obviously similar kinematics. Unfortunately the particle detector was degrading during the experimental runs, so the condition during the ^{130}Ba runs, which happened later, was worse than during

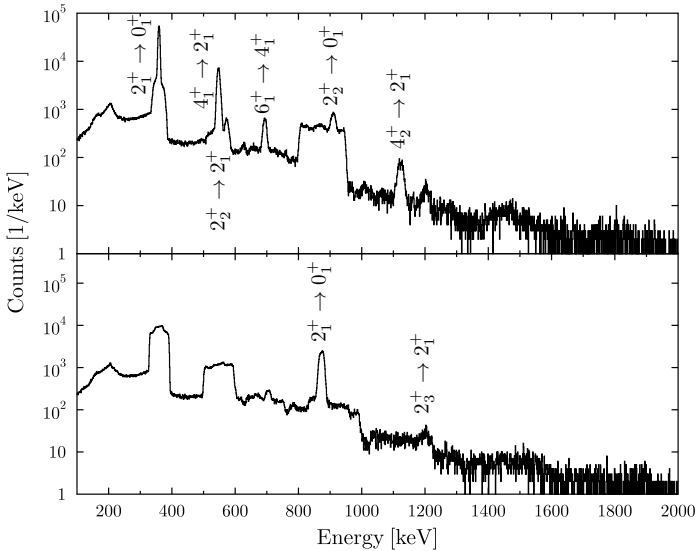


Figure 6.9.: Background-subtracted particle- γ coincidence spectra applying Doppler-correction with respect to the projectile ^{130}Ba (top) or recoiling target nuclei ^{94}Mo (bottom). The strongest transitions are labeled. The spectra show only the statistics from a single run.

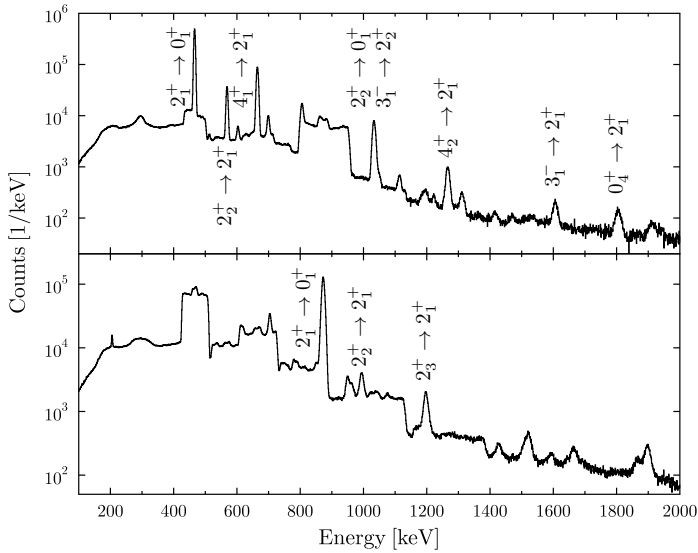


Figure 6.10.: Background-subtracted particle- γ coincidence spectra applying Doppler-correction with respect to the projectile ^{132}Ba (top) or recoiling target nuclei ^{94}Mo (bottom). The strongest transitions are labeled.

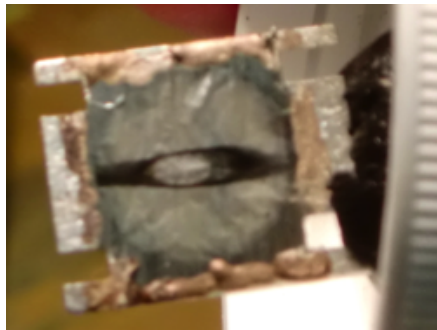


Figure 6.11.: The ^{94}Mo target shows signs of a broad or wobbling beamspot during the high energy ^{132}Ba runs.

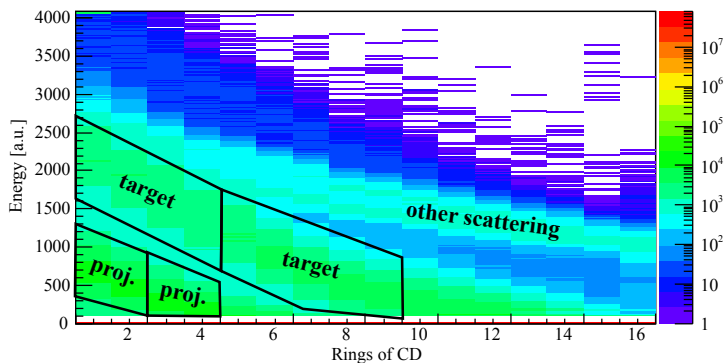


Figure 6.12.: Particle distribution on the DSSD for the ^{132}Ba experiment. The kinematical cuts corresponding to the particle gates of tab. 6.3 are indicated.

the ^{132}Ba runs. Fig. 6.12 of the ^{132}Ba experiment is an example for the particle identification with the help of the kinematics for the well operating DSSD. Beside the solid performance of the DSSD during those runs another disturbing effect becomes visible here. The beam was most probably hitting the frame of the target and thereby lighter nuclei, eventually Al, have been scattered to larger angles. This is indicated by "other scattering" in fig. 6.12. This explanation is supported by a view of the target condition after the experiment in the photograph of fig. 6.11. One can clearly see a very ellipsoidal shape of the beamspot. From the discussion with the operators it was not clear if the beam was really so ellipsoidal or if it was wobbling over the target or maybe a combination of both effects.

From the observed γ -ray energies (figs. 6.9 and 6.10) and their coincidences the level schemes of fig. 6.13 for (a) ^{130}Ba and (b) ^{132}Ba can be deduced. All observed transitions and their ordering are confirmed by the agreement with the literature [Ens]. The experimental γ -ray yields, as documented in tables 6.2 and 6.3, are determined from the spectra by integration, separately for the four kinematical cuts (fig. 6.12, later referred to as sub-experiments), for projectile and target excitation, and for both isotopes.

In the further analysis the multiple Coulomb-excitation code GOSIA2 [CCW83], introduced in subsec. 4.4, is used. It varies all matrix elements for the calculation of the Coulex process in such a way that the experimental γ -ray yields, as documented in tables 6.2 and 6.3, are reproduced. The projectile excitation of $^{130,132}\text{Ba}$ is normalized to the target excitation of ^{94}Mo . In the case of ^{130}Ba 6 matrix elements are

Ring (DSSD)	6+7	8+9	9-12	13-16
detected	projectile	projectile	target	target
θ_{lab} -range	39.29°-41.86°	41.86°-44.25°	43.08°-47.49°	47.49°-51.27°
^{130}Ba				
$2_1^+ \rightarrow 0_1^+$	1000.0(56)	1000.0(51)	1000.0(53)	1000.0(51)
$4_1^+ \rightarrow 2_1^+$	343.2(51)	384.2(18)	226.2(14)	185.8(10)
$2_2^+ \rightarrow 2_1^+$				
$6_1^+ \rightarrow 4_1^+$	37.1(8)	45.3(5)	14.9(4)	10.5(3)
$2_2^+ \rightarrow 0_1^+$	42.3(29)	52.3(7)	30.9(8)	25.0(5)
^{94}Mo				
$2_1^+ \rightarrow 0_1^+$	223.0(19)	240.8(14)	188.6(14)	177.5(11)

Table 6.2.: Summary of the measured yields in the $^{94}\text{Mo}(^{130}\text{Ba},^{130}\text{Ba}^*)^{94}\text{Mo}^*$ reaction for the different ranges of scattering angles (efficiency corrected and normalized to yield of $2_1^+ \rightarrow 0_1^+$ transition of ^{130}Ba). Please note the transitions $4_1^+ \rightarrow 2_1^+$ and $2_2^+ \rightarrow 2_1^+$ could not be resolved in the spectra and are taken into account as a doublet.

Ring (DSSD)	1+2	3+4	1-4	5-9
detected	projectile	projectile	target	target
θ_{lab} -range	31.94°-35.04°	35.04°-37.93°	31.94°-37.93°	37.93°-44.25°
¹³⁰ Ba				
2 ₁ ⁺ → 0 ₁ ⁺	1000.0(206)	1000.0(233)	1000.0(88)	1000.0(80)
2 ₂ ⁺ → 2 ₁ ⁺	83.6(20)	99.8(13)	143.0(11)	111.6(8)
4 ₂ ⁺ → 4 ₁ ⁺	7.25(16)	10.1(5)	17.3(2)	12.6(2)
4 ₁ ⁺ → 2 ₁ ⁺	268.1(135)	307.1(182)	399.4(119)	335.4(140)
4 ₂ ⁺ → 2 ₂ ⁺	17.6(5)	25.1(5)	43.2(5)	28.4(7)
3 ₁ ⁻ → 2 ₂ ⁺	46.4(9)	54.3(23)	79.2(5)	62.0(4)
2 ₂ ⁻ → 0 ₁ ⁺				
4 ₂ ⁻ → 2 ₁ ⁺	6.40(11)	7.69(24)	14.5(2)	9.88(20)
3 ₁ ⁻ → 2 ₁ ⁺	1.76(16)	1.40(16)	1.24(11)	1.54(11)
⁹⁴ Mo				
2 ₁ ⁺ → 0 ₁ ⁺	397.1(198)	408.6(133)	498.6(80)	448.5(49)
4 ₁ ⁺ → 2 ₁ ⁺	32.1(8)	46.6(11)	57.2(10)	47.6(10)
2 ₃ ⁺ → 2 ₁ ⁺	7.79(23)	7.17(22)	9.79(18)	8.16(18)
2 ₃ ⁻ → 0 ₁ ⁺	9.27(47)	1.19(10)	1.37(8)	0.995(76)

Table 6.3.: Summary of the measured yields in the $^{94}\text{Mo}(^{132}\text{Ba},^{132}\text{Ba}^*)^{94}\text{Mo}^*$ reaction for the different ranges of scattering angles (efficiency corrected and normalized to yield of $2_1^+ \rightarrow 0_1^+$ transition of ^{132}Ba). Please note the transitions $3_1^- \rightarrow 2_2^+$ and $2_2^+ \rightarrow 0_1^+$ could not be resolved in the spectra and are taken into account as a doublet.

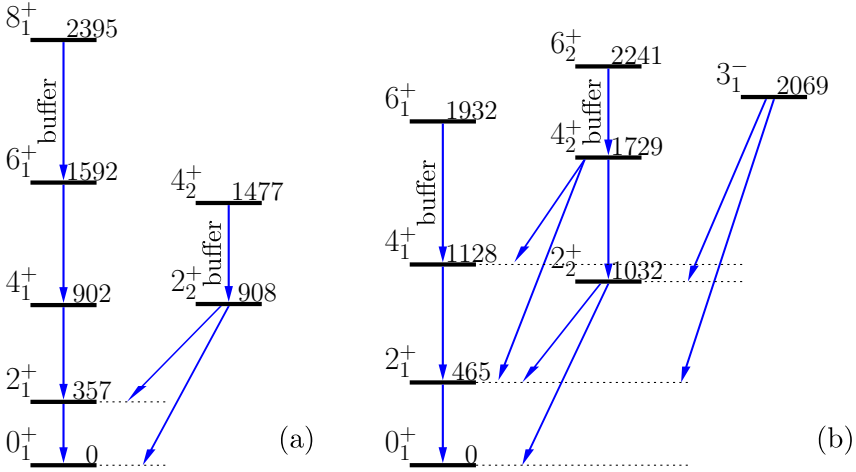


Figure 6.13.: The level schemes of (a) ^{130}Ba and (b) ^{132}Ba with all levels and transitions taken into account in the Coulex analysis.

fitted to 16 measured experimental yields (4 yields in 4 sub-experiments), 1 previously known branching ratio and 4 lifetimes, including the newly measured lifetime of the 2_2^+ state (see subsec. 6.4.1), which is of special importance due to the interference effect. In the case of ^{132}Ba 16 matrix elements are fitted to 32 measured experimental yields (8 yields in 4 sub-experiments), 2 previously known multipole mixing ratios and 1 experimental matrix element. One has to consider that beside all feeding transitions of the complex level schemes (see fig. 6.13) the cross-section σ for the 2_1^+ state is directly influenced by both, the transitional and the diagonal matrix element, M_{20} and M_{22} . Because of the aim to measure $Q(2_1^+)$, which is directly related to M_{22} , it is necessary to investigate the mutual dependence of the projectile's excitation cross-section $\sigma_{2_1^+}$ on M_{20} and M_{22} by a certain GOSIA2 error analysis [Hay]. A fixed set of start parameters for the matrix elements M_{20} and M_{22} is given as input to the GOSIA2 program, which then theoretically computes γ -ray yields while fitting all other matrix elements. The results for an even bigger set of matrix elements of both nuclei can be found in the work of Thomas Möller [Möl13] where the data is combined with the analysis of runs with a light carbon target as introduced in the summary of experiments in sec. 5.3. In the analysis of this work a χ^2 value is extracted for each set of initial start parameters M_{20} and M_{22} and the variation of these start parameters results in a χ^2 surface. The figures 6.14 (a,b)

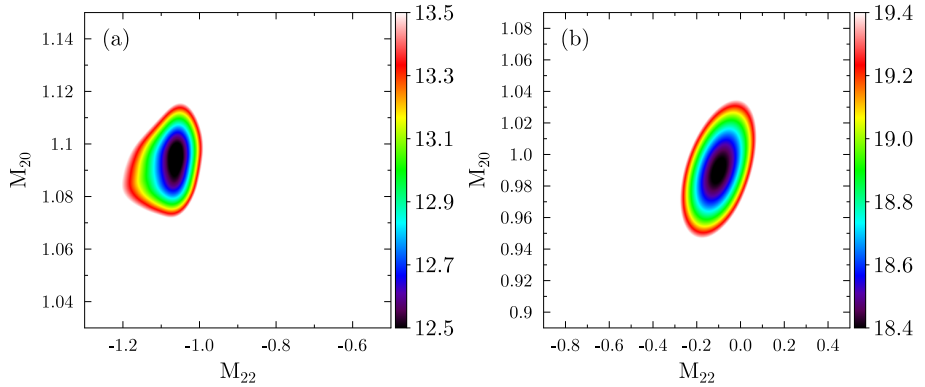


Figure 6.14.: χ^2 surfaces with respect to the diagonal and transitional matrix elements of the 2_1^+ state in (a) ^{130}Ba and (b) ^{132}Ba from the Coulex experiments with a ^{94}Mo target.

represent the χ^2 values for $^{130,132}\text{Ba}$. The 1σ -contour of this surfaces is projected to the respective axes to extract the matrix elements and their uncertainties. The experimental results of the χ^2 surface projections and the deduced observables are summarized in table 6.4. As final results the following spectroscopic quadrupole moments are determined:

$$Q(2_1^+, ^{130}\text{Ba}) = -0.80_{-0.11}^{+0.05}\text{eb}$$

$$Q(2_1^+, ^{132}\text{Ba}) = -0.08(13)\text{eb}$$

The fits of all data clearly indicate constructive interference of the 2_2^+ state in ^{130}Ba and ^{132}Ba , respectively. This result of a positive interference term (constructive interference) is supported by the theoretical work of Jolos and Brentano of ref. [JB96] as well. Nevertheless both options have been chosen in the fit and the results with an interference term, artificially set to a negative value, are presented as well in table 6.4. The smaller χ^2 values of the fits with constructive interference for both isotopes, ^{130}Ba and ^{132}Ba , serves as proof of the constructive interference in both cases.

Nucleus	τ [ps]	Matrix elements M.E.	Experiment			B(E2) \uparrow , Q_s [e ² b ² ₁ , [eb]	B(E2) \downarrow [W.u.]	Literature [e ² b ² ₁ , [eb]
			intert.	χ^2				
¹³⁰ Ba	^a 62.3(7)	$\langle 2^+ E2 0^+ \rangle$	1.093(21)	+	12.5	1.195(46)	61.1(23)	^{a,b} 1.081(12)
		$\langle 2^+ E2 2^+ \rangle$	-1.06 ^{+0.07} _{-0.14}		19.0	-0.80 ^{+0.05} _{-0.11}	-	- ^c 1.02(16)
			-0.48(17)	-		-0.35(13)	-	- ^e 0.09(16)
¹³² Ba	^d 18.8(16)	$\langle 2^+ E2 0^+ \rangle$	0.990(43)	+	18.4	0.98(9)	49.1(43)	^e 0.897(26)
		$\langle 2^+ E2 2^+ \rangle$	-0.10(17)			-0.08(13)	-	n.m.
		$\langle 2^+ E2 2^+ \rangle$	0.86(24)	-	22.2	0.65(18)	-	n.m.

a: from RDDS measurement [Stu01]

b: deduced from lifetime

c: from reorientation measurement [Bur89]

d: deduced from Coulex measurement of this work

e: from Coulex measurement [Bur85]

Table 6.4.: Experimental results for the matrix elements of the transition $2^+ \rightarrow 0^+$ and related observables. Previously measured values are indicated by "Literature" and published in [Bur85; Bur89]. The first line for the quadrupole moments is calculated with constructive interference, the second line with forced negative interference ($\langle 0^+ || M(E2) || 2^+ \rangle < 0$). The lower χ^2 values show in both cases that constructive interference is the right choice.

6.5 Radioactive isotopes ^{140,142}Ba

The Ba ions of both isotopes were Coulomb excited in two subsequent runs on a 0.9 mg/cm² ⁹⁶Mo target and on a 1 mm thick ^{nat}Cu target. The latter was thick enough for continuously slowing down the beam ions until they came to rest within the target. During the stopping process the measured energies of the deexcitation γ rays of the ($2_1^+ \rightarrow 0_1^+$) transition of Coulomb-excited ¹⁴⁰Ba ions are changed under the influence of the Doppler shift resulting in a characteristic lineshape of the photopeak. All excited ions come to rest within 3 ps after their Coulomb excitation. This allows for a lifetime analysis as described in subsection 6.5.1 while the runs with ¹⁴²Ba impinging on the thick ^{nat}Cu target were just used in a recoil-in-vacuum g-factor analysis by the author in ref. [Bau09a]. Here the lifetime was already known and, furthermore, too long for a DSAM analysis similar to ¹⁴⁰Ba.

The 20 working HPGe crystals covered angles θ_γ between 43° and 77° and between 109° and 136°. In case of the ⁹⁶Mo target, the projectile- and target-like recoil ions were detected in forward direction in coincidence with the emitted γ rays in the CD with an opening angle of $\theta = 16.4^\circ - 54.2^\circ$.

The uncertainty of the current literature value of $\tau = 14.0 \pm 5.9$ ps for the 2_1^+ state of ¹⁴⁰Ba [MGM89] does not permit the use of the *reorientation technique* as described in sec. 4.2. Therefore the complementary lifetime measurement was performed and in order to efficiently use the precious beam time for intense radioactive beams and for minimizing systematical errors, both measurements were done using one and the same setting of the radioactive beam. This approach differs from preceding experiments at MINIBALL applying the reorientation method with Coulomb-excitation reactions [Hur07; Eks09], where the lifetime data was taken from a different experiment. The measurement of the sign and magnitude of the spectroscopic quadrupole moment of the 2_1^+ state of ¹⁴⁰Ba represents a unique combination of the reorientation technique and the DSA method for the same setting of the radioactive beam. It was published recently by the author in ref. [Bau12b]. In the case of ¹⁴²Ba the already precisely known lifetime of 95(5) ps [MGM89] could be used for an analogous analysis [Ste11].

6.5.1 DSAM measurement of ¹⁴⁰Ba

The lifetime was determined applying the Doppler-shift attenuation method (DSAM). The lifetime of the 2_1^+ state of ¹⁴⁰Ba was deduced from a simultaneous DSAM fit to 18 energy spectra using the newly developed program package APCAD [Sta13]. Two energy spectra were excluded from the fit due to poor energy resolution. A low-energy tailing in the peak shapes due to neutron damage

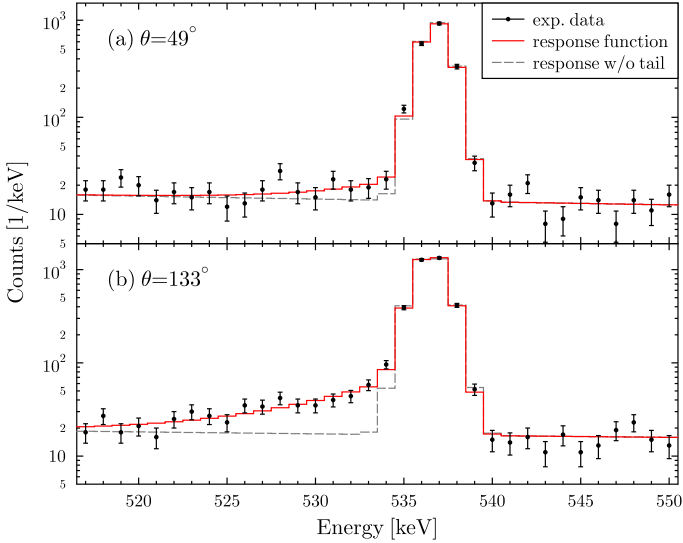


Figure 6.15.: The fully stopped $0_1^- \rightarrow 1_1^-$ transition in ^{140}La following β decay of ^{140}Ba is displayed. Low-energy tails of the γ -ray lines appear due to partial neutron damage of the detectors. Dashed (grey) lines show a symmetric Gaussian peak shape compared to the fitted shape accurately reproducing the described effect (solid, red).

of the MINIBALL detectors was observed. In order to reproduce this behavior the detector response was modeled by a HYPERMET-like function from ref. [HL80] and references therein. The parameters of the response functions have been determined individually for each crystal from a fit to the peak shape of the Doppler-free ($0_1^- \rightarrow 1_1^-$) transition in ^{140}La at 537 keV following the β decay of ^{140}Ba , see fig. 6.15. Examples for DSAM fits for one crystal in forward and one crystal in backward direction are shown in fig. 6.16. From the global fit a lifetime of

$$\tau_{2_1^+}(^{140}\text{Ba}) = 10.4^{+2.2}_{-0.8} \text{ ps}$$

was obtained in good agreement with the literature value but with significantly improved accuracy. With $^{+2.1}_{-0.7}$ ps the systematic uncertainties of the stopping powers clearly dominate the uncertainty of the final result. The statistical significance is demonstrated in fig. 6.16 (e).

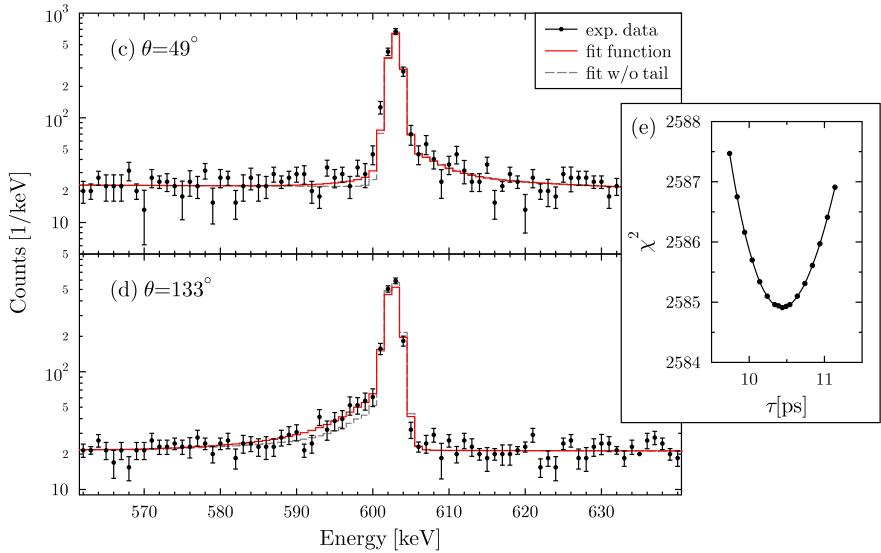


Figure 6.16.: The Doppler-broadened lineshapes of the $2_1^+ \rightarrow 0_1^+$ transition in ^{140}Ba for (c) 49° and (d) 133° are shown after background-subtraction. The spectra are shifted by +20 counts per channel for better visibility on the logarithmic scale. The full fits are represented by solid (red) lines, the corresponding peak shapes without the effect of neutron damage are dashed (grey). At forward angles the Doppler-lineshapes are not significantly disturbed by any low-energy tailing due to partial neutron damage of the Ge detectors. Panel (e) shows the χ^2 values for the combined fit to the lineshapes detected in 18 crystals as a function of the lifetime of the 2_1^+ state ($\chi_{red,min}^2 = 0.92$, NDF = 2812).

6.5.2 Reorientation technique

An analysis of Coulex yields of the runs with ^{140}Ba and ^{142}Ba impinging on the thin ^{96}Mo target finally allows to determine the quadrupole moment $Q(2_1^+)$ for both isotopes. The theory behind this Coulex reorientation analysis is explained in sec. 4.2 and was performed already in 1965 [Boe65].

Fig. 6.17 shows the sum of the γ -ray spectra of all detectors of the MINIBALL array with Doppler-correction for the Coulomb-excited ^{140}Ba projectiles (top) and

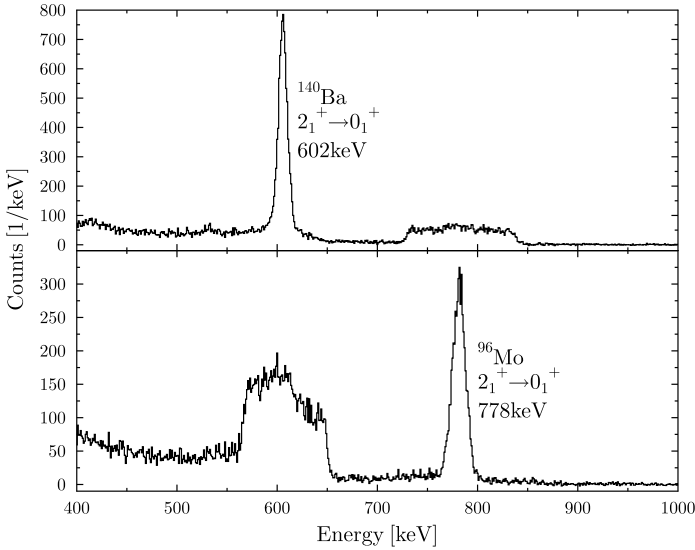


Figure 6.17.: Background-subtracted particle- γ coincidence spectra applying Doppler-correction with respect to the projectile (top) or recoiling target nuclei (bottom) showing the only observed transitions, namely the $2_1^+ \rightarrow 0_1^+$ transitions in ^{140}Ba at 602 keV and in ^{96}Mo at 778 keV.

^{96}Mo target recoils (bottom) in coincidence with the particle signals from the DSSD. No other γ -ray transitions than the de-excitation of the 2_1^+ states to the ground states at 602 keV for ^{140}Ba and at 778 keV for ^{96}Mo were visible. Fig. 6.18 shows the analog picture for ^{142}Ba . The distribution of hits on the DSSD is very similar for both experiments due to the obviously similar kinematics. Fig. 6.19 of the ^{142}Ba experiment serves as an example for the particle identification. The yields stemming from the corresponding cuts on the detected particles are listed in tab. 6.6 as well.

For the 2_1^+ state both the transitional and the diagonal matrix elements, M_{20} and M_{22} , affect the projectiles's Coulomb-excitation cross-section σ^P . Using the multiple Coulomb-excitation codes CLX and DCY [Owe80] these matrix elements are varied such that the experimental γ yields (comp. tab. 6.5 and tab. 6.6) are reproduced. The mutual dependence of σ^P on M_{20} and M_{22} results in a band in the (M_{22}, M_{20}) plane restricted by the required reproduction of the observed Coulomb-excitation cross-section. The projectile excitation is normalized to the

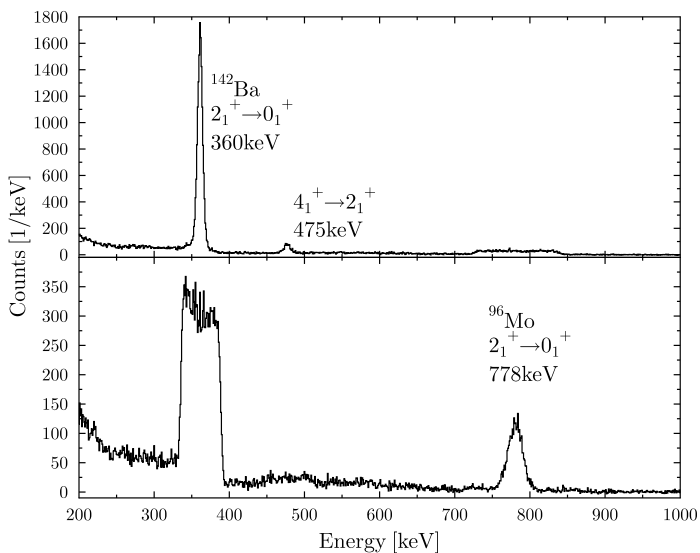


Figure 6.18.: Background-subtracted particle- γ coincidence spectra applying Doppler-correction with respect to the projectile (top) or recoiling target nuclei (bottom) showing the $2_1^+ \rightarrow 0_1^+$ transitions in ^{142}Ba at 360 keV and in ^{96}Mo at 778 keV.

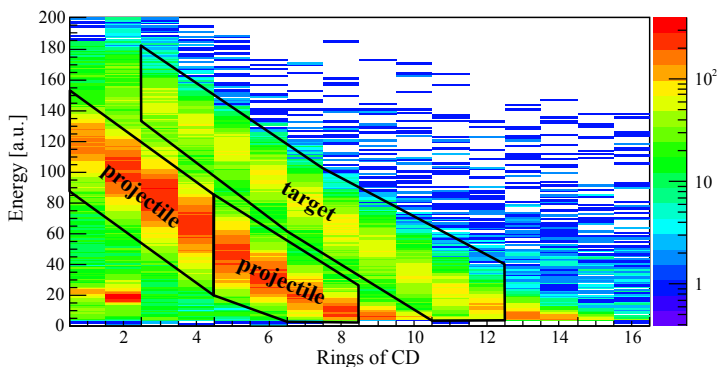


Figure 6.19.: Particle distribution on the DSSD for the ^{142}Ba experiment. The kinematical cuts corresponding to the particle gates of tab. 6.6 are indicated.

ring(CD)	θ -range	detected	^{140}Ba	^{96}Mo
1+2	16.4°-22.9°	proj.	2717(55)	1442(39)
3+4	23.0°-28.9°	proj.	3089(59)	1759(43)
5+6	29.1°-34.3°	proj.	2465(52)	1453(39)

Table 6.5.: Summary of the measured yields of ^{140}Ba and ^{96}Mo ($2_1^+ \rightarrow 0_1^+$ transition) for the different ranges of scattering angles (not efficiency corrected).

ring(CD)	θ -range	detected	^{142}Ba	^{96}Mo
1-4	16.4°-28.9°	proj.	5511(79)	965(32)
5-8	29.1°-39.1°	proj.	4824(73)	941(32)
2-12	23.0°-47.1°	targ.	4300(68)	908(31)

Table 6.6.: Summary of the measured yields of ^{142}Ba and ^{96}Mo ($2_1^+ \rightarrow 0_1^+$ transition) for the different ranges of scattering angles (not efficiency corrected).

excitation σ^T of the 2_1^+ state of ^{96}Mo taking also the angular distribution $W(\theta)$ of the γ rays into account by

$$\sigma^P(M_{20}, M_{22}) = \frac{N_\gamma^P}{N_\gamma^T} \frac{\epsilon^T}{\epsilon^P} \frac{W(\theta)^T}{W(\theta)^P} \sigma^T. \quad (6.24)$$

The main contributions to the uncertainty are the statistical errors of the experimental γ -ray yields N_γ from projectile ($^{140,142}\text{Ba}$) and target (^{96}Mo) excitation, as well as the uncertainty in the matrix elements of ^{96}Mo . The efficiency of the Germanium detectors is denoted by ϵ and has an uncertainty of approx. 1-2%. Fig. 6.20 illustrates by means of ^{140}Ba the increasing impact of the M_{22} matrix element on the differential Coulomb-excitation cross-section as the scattering angle of the projectile-like recoils increases. This is best shown by the relative sensitivity

$$S(\theta_1) = \frac{\sigma^P(\theta_1, M_{22} = +1.2M_{20}) - \sigma^P(\theta_1, M_{22} = -1.2M_{20})}{\sigma^P(\theta_1, M_{22} = 0)} \quad (6.25)$$

defined as the relative variation of the cross-section with the quadrupole moment ranging from prolate to oblate within the rigid rotational limit as a function of scattering angle. In order to maximize the sensitivity to M_{22} , and related to this, to the quadrupole moment Q , different scattering-angle ranges are defined. For ^{140}Ba ions ranges with scattering angles $\theta_{lab} = 16.4^\circ$ - 22.9° , 23.0° - 28.9° , 29.1° - 34.3° have

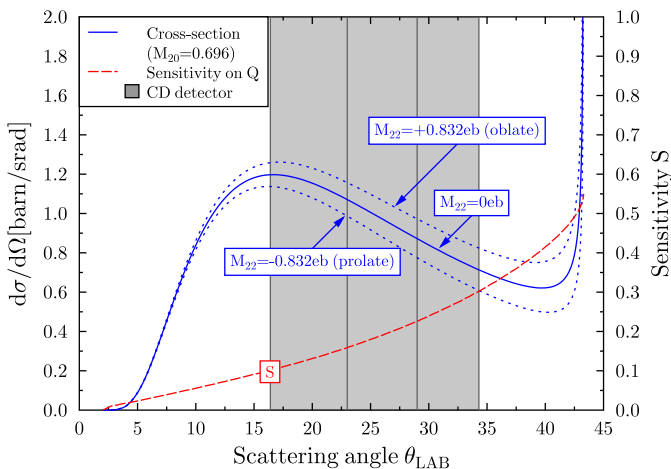


Figure 6.20.: Differential Coulomb-excitation cross-sections for the excitation of the 2_1^+ state in ^{140}Ba as function of the scattering angle in the laboratory frame for diagonal matrix elements $M_{22} = 0\text{eb}$ (solid curve) and for $M_{22} = \pm 0.832\text{eb} = \pm 1.195M_{20}$ which represent the rigid rotational limit [BM69] for the given matrix element $M_{20} = 0.696\text{eb}$ derived from the present lifetime. Each of the vertical bars (gray) illustrates the angular coverage of the corresponding rings of the particle detector. The relative sensitivity on Q is denoted by S as defined in eq. 6.25.

been selected that correspond to two rings of the DSSD in each case. In the case of ^{142}Ba the different ranges are also illustrated in fig. 6.19.

A maximum likelihood analysis [Eks09] finally yields the matrix elements and from M_{22} the spectroscopic quadrupole moments are deduced via eq. 4.27:

$$Q(2_1^+, ^{140}\text{Ba}) = -0.52(34)\text{eb}$$

$$Q(2_1^+, ^{142}\text{Ba}) = -0.39(29)\text{eb}$$

In fig. 6.21 and 6.22 the contour curves in the (M_{22}, M_{20}) plane from the analysis of the experimental Coulomb-excitation yields and the lifetimes are shown. In addition, the results are summarized in table 6.7.

The normalization to the target excitation in eq. 6.24 introduces also a dependence on the matrix element $M_{22} = \langle 2_1^+ || E2 || 2_1^+ \rangle$ of ^{96}Mo from which two different

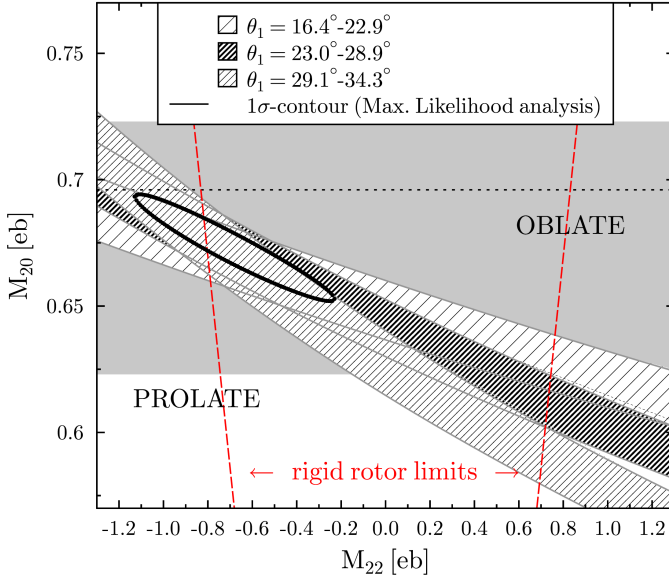


Figure 6.21.: The bands for the different scattering angle ranges of ^{140}Ba show the agreement of the calculations with the experimental yields. The lifetime measurement provides the horizontal band as the allowed region of the transitional matrix element $\langle 2_1^+ || E2 || 0_1^+ \rangle$ (dashed line for the most likely value). Vertical dashed lines give the rotational model values ($M_{22} = \pm 1.195M_{20}$) of a pure prolate or oblate rotor.

values, $M_{22} = +0.05(10)$ eb and $M_{22} = -0.26(11)$ eb, are reported in the literature [Par76]. The usage of the positive but small value of $M_{22} = +0.05(10)$ eb in the analysis of the present work would drive the quadrupole moments of $^{140,142}\text{Ba}$ beyond the limits of the rigid rotor. This finding is supported by a recent measurement of $Q(2^+)$ in ^{96}Mo yielding a negative diagonal matrix element of $-0.44(5)$ eb [Zie11]. Therefore, a weighted average of $-0.41(5)$ eb of the two negative values for M_{22} is used in the analysis.

Due to the low beam energy at ca. 65% of the Coulomb barrier, no other transitions than $2_1^+ \rightarrow 0_1^+$ were observed. In the case of ^{142}Ba the $4_1^+ \rightarrow 2_1^+$ transition is visible in the sum spectrum (fig. 6.18) but cannot be properly treated in the evaluated spectra of the single kinematical cuts due to the lower statistics there.

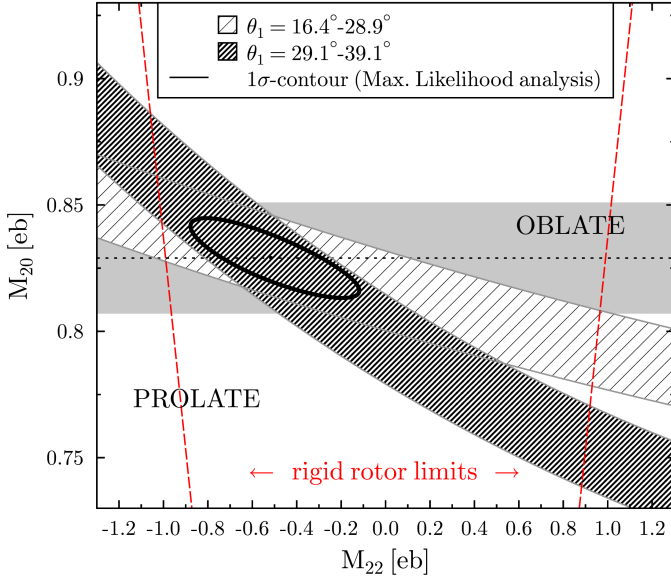


Figure 6.22.: The bands for the different scattering angle ranges of ^{142}Ba show the agreement of the calculations with the experimental yields. The independent lifetime measurement provides the horizontal band as the allowed region of the transitional matrix element $\langle 2_1^+ || E2 || 0_1^+ \rangle$.

However, the influence of higher-lying levels, namely the two-phonon states 2_2^+ and 4_1^+ , has been considered as well in the Coulex calculations for an accurate estimate of experimental uncertainties of the results. To that end the unknown E2 matrix elements of the transitions $4_1^+ \rightarrow 2_1^+$ and $2_2^+ \rightarrow 2_1^+$ have been chosen such that the corresponding photopeaks would just meet the sensitivity limit given by the γ -ray background in the spectrum. Further corrections result from the population of the 2_1^+ state via the 2_2^+ state which gives rise to the interference term $P_3(2_1^+)$ as introduced in sec. 6.4. The influence of this interference is small ($\approx 5\text{-}10\%$) for the used beam energy but was considered in the analysis as well and so for the 2_2^+ state also the sign of the connecting matrix element has been varied (constructive and destructive interference). These effects have been included in the estimate of the experimental uncertainty of the $Q(2_1^+)$ values given above. They do not affect the conclusion on predominant prolate deformations of the 2_1^+ states in $^{140,142}\text{Ba}$.

Nucleus	τ [ps]	Experiment			Literature	
		M.E.	B(E2) \uparrow , Q_s [e^2b^2], [eb]	B(E2) \downarrow [W.u.]		
^{140}Ba	$^{a,d}10.4^{+2.2}_{-0.8}$	$\langle 2^+_{11} E2 0^+_{11} \rangle$	$^{a,b}0.696^{+0.027}_{-0.073}$	$^{a,b}0.484^{+0.038}_{-0.101}$	$^{a,b}22.4^{+1.8}_{-4.7}$	$^{b,c}0.45(19)$
		$\langle 2^+_{11} E2 2^+_{11} \rangle$	$-0.69(45)$	$-0.52(34)$		n.m.
^{142}Ba	$^{e,95(5)}$	$\langle 2^+_{11} E2 0^+_{11} \rangle$	$^{b,c}0.830(22)$	$^{b,c}0.688(36)$	$^{b,c}31.3(16)$	$^{b,c}0.688(36)$
		$\langle 2^+_{11} E2 2^+_{11} \rangle$	$-0.51(38)$	$-0.39(29)$		n.m.

a: from DSAM of this work

c: from electronic timing [MGMR89]

b: deduced from lifetime

Table 6.7.: Experimental results for the matrix elements of the transition $2^+_{11} \rightarrow 0^+_{11}$ and related observables. Previously measured values are indicated by "Literature" and published in [MGMR89]. For ^{142}Ba the lifetime was precise enough for the analysis and M_{20} and B(E2) are deduced.

6.6 Radioactive N=80 isotones ^{140}Nd , ^{142}Sm

Beams of ^{140}Nd and ^{142}Sm with an energy of 2.85 MeV/u, corresponding to kinetic energies of 399 MeV and 405 MeV, respectively, have been produced at ISOLDE with an intensity of $\approx 5 \times 10^5$ ions/s in both cases. The laser ionization source RILIS [Fed08] was used in 2011 (Nd) as well as in 2012 (Sm) to suppress possible isobaric contaminations. The ^{140}Nd beam was contaminated by surface ionized Sm ions of the same mass. In two subsequent runs the beam was impinging on a 1.4 mg/cm² ^{48}Ti target and on a 1.55 mg/cm² ^{64}Zn target for Coulomb excitation measurements. In contrast to the Nd, the ^{142}Sm beam was contaminated by just small amounts of ^{142}Eu and ^{142}Pm . Again two targets could be used for Coulomb excitation, 1.4 mg/cm² ^{48}Ti and 2.0 mg/cm² ^{94}Mo , respectively. The description of the analysis of the Sm experiment is shortened in comparison to the Nd because it is quite similar and was analyzed in cooperation with a Master student [Ste12] under my immediate supervision.

The MINIBALL array (see sec. 5.2) was used in its standard configuration, covering about 2π of the solid angle, for the detection of the de-excitation γ rays, analog to the experiments presented in sec. 6.5. The double-sided silicon-strip detector (DSSD) was covering an opening angle of $\theta_{lab} = 15.6^\circ - 51.8^\circ$ for the Nd runs and due to a different distance to the target $\theta_{lab} = 19.7^\circ - 58.4^\circ$ during the Sm runs. The analysis of the Coulomb excitation yields allows to determine the cross-section for the 2_1^+ state of ^{140}Nd (^{142}Sm) relative to the known cross-sections of the target excitations. Thereby, the transition strength $B(E2; 2_1^+ \rightarrow 0_1^+)$ of the two isotopes is determined.

6.6.1 ^{140}Nd

Figure 6.23 shows the sum of the γ -ray spectra of all detectors of the MINIBALL array with Doppler-correction for mass A=140 projectiles (a) and ^{48}Ti target recoils (b) in coincidence with the particle signals from the DSSD. A random background was subtracted. No other γ -ray transitions than the de-excitation of the 2_1^+ states to the ground states at 531 keV for the ^{140}Sm contamination, at 774 keV for ^{140}Nd and at 984 keV for ^{48}Ti were visible. In the case of the ^{64}Zn target the spectra in fig. 6.23 (c,d) show instead of the ^{48}Ti excitation the de-excitation of the Coulomb-excited 2_1^+ state in ^{64}Zn at almost the same energy (992 keV).

A crucial point in this kind of experiments with a radioactive beam is the determination of the beam contaminants. For the Nd data set it is possible to determine the contribution of the isobaric ^{140}Sm contaminant to the target excitation yield by a comparison of the performed runs with and without laser ionization. Figure 6.23

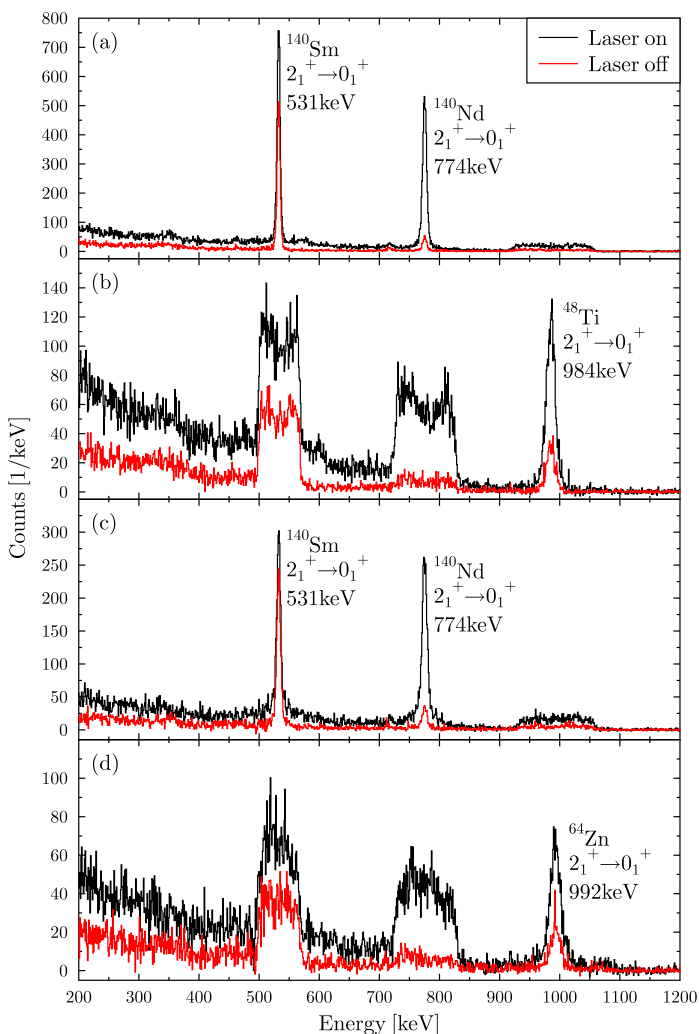


Figure 6.23.: Background-subtracted particle- γ coincidence spectra applying Doppler-correction with respect to the (a,c) projectile or (b,d) recoiling target nuclei showing the only observed transitions, namely the $2_1^+ \rightarrow 0_1^+$ transitions in ^{140}Sm at 531 keV, in ^{140}Nd at 774 keV, in ^{48}Ti at 984 keV, and in ^{64}Zn at 992 keV. The data with laser ionization switched on (black) and off (red) is shown in the same spectra.

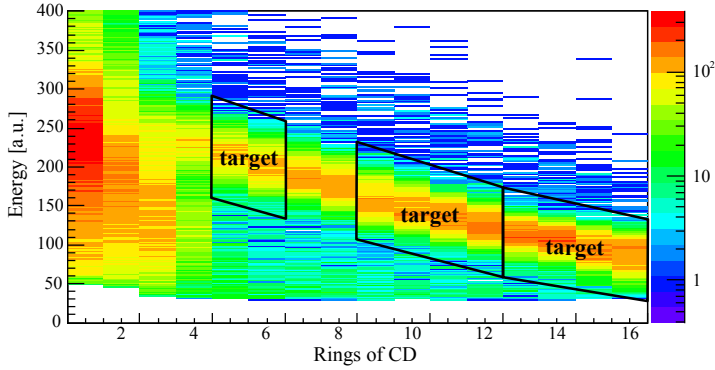


Figure 6.24.: Particle distribution on the CD for the $^{140}\text{Nd} \rightarrow ^{48}\text{Ti}$ experiment. The "banana gates" corresponding to the cuts of tab. 6.8 are indicated.

Ring (DSSD)	detected	θ_{lab} -range	^{140}Nd	^{48}Ti
5-6	target	27.8° - 33.0°	565(24)	217(17)
9-12	target	37.8° - 45.6°	1346(53)	531(27)
13-16	target	45.7° - 51.8°	1221(36)	547(27)

Table 6.8.: Summary of the measured yields in the $^{48}\text{Ti}(^{140}\text{Nd}, ^{140}\text{Nd}^*)^{48}\text{Ti}^*$ reaction for the different ranges of scattering angles (efficiency corrected).

shows both, the γ -ray spectra recorded with the laser switched on (black) and off (red). The laser settings were optimized for ionizing Nd isotopes, such that the Nd excitation is suppressed for runs without laser. The amount of Sm in the beam is not affected by the laser and can thereby serve for normalizing the spectra to the Sm contaminant. By subtracting the normalized laser-off spectrum a pure Coulomb excitation spectrum of Nd on either target (Ti or Zn) is achieved. Through this procedure one assures that the remaining target excitation yield is correlated to the yield of the Nd excitation and not to any other beam components. As an example for the particle identification the distribution of hits on the particle detector is shown in fig. 6.24 for the runs with the ^{48}Ti target. The cuts on the detected particles are listed in the yield table 6.8 as well; the same table is given for the runs with the ^{64}Zn target (tab. 6.9).

As explained in the previous sections, the Coulomb-excitation cross-section σ for the 2_1^+ state is influenced by both, the transitional and the diagonal matrix element, M_{20} and M_{22} . Using the multiple Coulomb-excitation code GOSIA2 [CCW83] these

Ring (DSSD)	detected	θ_{lab} -range	^{140}Nd	^{64}Zn
7-11	target	33.1°-43.8°	464(22)	239(18)
12-16	target	43.9°-51.8°	515(23)	211(17)
1-3	projectile	15.6°-24.8°	1281(36)	492(26)

Table 6.9.: Summary of the measured yields in the $^{64}\text{Zn}(^{140}\text{Nd}, ^{140}\text{Nd}^*)^{64}\text{Zn}^*$ reaction for the different ranges of scattering angles (efficiency corrected).

matrix elements are varied in such a way that the experimental γ -ray yields, as documented in tables 6.8 and 6.9, are reproduced. The mutual dependence of the projectile's excitation cross-section σ^P on M_{20} and M_{22} results in an area in the (M_{22}, M_{20}) plane representing the experimental Coulomb-excitation cross-section. The projectile excitation is normalized to the target excitation σ^T of the 2_1^+ state of ^{48}Ti and ^{64}Zn , respectively, taking also the angular distribution $W(\theta)$ of the γ rays into account:

$$\sigma^P(M_{20}, M_{22}) = \frac{N_\gamma^P}{N_\gamma^T} \frac{\epsilon^T}{\epsilon^P} \frac{W(\theta)^T}{W(\theta)^P} \sigma^T \quad (6.26)$$

The main contributions to the uncertainty are the statistical errors of the experimental γ -ray yields N_γ from projectile (^{140}Nd) and target excitation ($^{48}\text{Ti}/^{64}\text{Zn}$), as well as the uncertainty in the matrix elements of the targets. The efficiency of the Germanium detectors is denoted by ϵ and has an error of approximately 1-2%. In order to maximize the sensitivity and simultaneously keeping the statistical error on a reasonable level, the different scattering angle ranges were defined, corresponding to several rings of the DSSD each (see fig. 6.23 and tab. 6.8). Due to the different kinematics the ranges have been adjusted for the ^{64}Zn target in tab. 6.9.

For the final determination of the matrix elements a fixed set of start parameters for the matrix elements M_{20} and M_{22} is given as input to the GOSIA2 program, which then calculates theoretical γ -ray yields. By comparison to the experimental yields a χ^2 value is extracted for each set of initial start parameters M_{20} and M_{22} . The variation of these start parameters results in a χ^2 surface plotted in fig. 6.25. The 1σ -contour of this surface is projected to the respective axes to extract the matrix elements and their uncertainties. The experimental results of the χ^2 surface projections and the deduced observables are summarized in tab. 6.10 to

$$^{140}\text{Nd} : B(E2; 2_1^+ \rightarrow 0_1^+) = 33(2) \text{ W.u.}$$

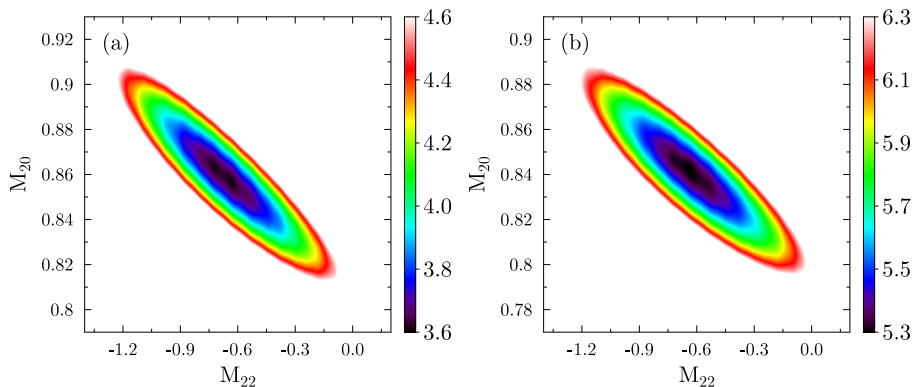


Figure 6.25.: χ^2 surface with respect to the diagonal and transitional matrix elements of the 2_1^+ state in ^{140}Nd from the Coulex experiment with (a) ^{48}Ti and (b) ^{64}Zn target.

	M_{20} [eb]	$B(E2)\uparrow$ [e^2b^2]	M_{22} [eb]	$Q(2_1^+)$ [eb]
^{48}Ti target	0.860(47)	0.74(8)	-0.65(57)	-0.49(43)
^{64}Zn target	0.842(46)	0.71(8)	-0.62(58)	-0.47(44)
weighted average	0.85(3)	0.72(5)	-0.64(41)	-0.48(31)
		= 33(2) W.u.		

Table 6.10.: Summary of the experimental results for ^{140}Nd for the single runs with Ti/Zn target and a weighted average.

6.6.2 ^{142}Sm

The analysis of ^{142}Sm does not differ from the previous one for ^{140}Nd presented in subsec. 6.6.1 in terms of the Coulomb-excitation analysis with the computer code GOSIA2 [CCW83]. The relevant yields are given in tables 6.11 and 6.12 and the summed γ -ray spectra are shown in fig. 6.26. However, beforehand the contamination was determined in a different way. There was no large contamination resulting in a Coulex yield as it was the case for ^{140}Sm in the Nd runs. Therefore mainly runs with lasers on were performed during the experiment and at the end a thick ^{nat}Cu target was irradiated by the beam in order to enable a detailed decay spectroscopy afterwards from a measurement at the end of the experiment.

After stopping the beam the γ -ray lines in the decay spectrum are observed in bins of 3 minutes. The isobaric nuclei ^{142}Pm and ^{142}Eu are suspected contaminant due to the observed lines. The intensity of the ^{142}Pm lines does not change significantly during 30 minutes although this isotope has a short half-life of 40.5s, which leads to the conclusion, that all the ^{142}Pm nuclei stem from the decay of the long-lived beam particles of ^{142}Sm with a half-life of 72.5min. For the determination of the ^{142}Eu fraction of the beam a more sophisticated ansatz has to be chosen. From the observed β -decay lines and the decay law with the known lifetimes a set of differential equations is set up and solved for large times. This results in a contamination from ^{142}Eu of 2.7(2.2)%.

The detailed analysis can be found in ref. [Ste12] and one further restriction had to be done. The Coulex analysis also allowed for an unphysical large deformation of the 2_1^+ state of ^{142}Sm . Therefore the quadrupole moment was restricted to the rigid rotor limits [BM69] and just the transitions strength could be deduced. Due to the introduced restriction no fair statement on the quadrupole moment is possible. The experimental result summarizes in tab. 6.13 to

$$^{142}\text{Sm} : B(E2; 2_1^+ \rightarrow 0_1^+) = 30(2) \text{ W.u.}$$

Ring (DSSD)	detected	θ_{lab} -range	^{142}Sm	^{48}Ti
4-6	target	30.8°-39.7°	1125(34)	342(19)
7-9	target	39.8°-46.9°	1179(35)	411(21)
10-12	target	47.0°-52.6°	1102(34)	435(21)
13-15	target	52.6°-57.1°	932(31)	350(19)

Table 6.11.: Summary of the measured yields in the $^{48}\text{Ti}(^{142}\text{Sm}, ^{142}\text{Sm}^*)^{48}\text{Ti}^*$ reaction for the different ranges of scattering angles (not efficiency corrected).

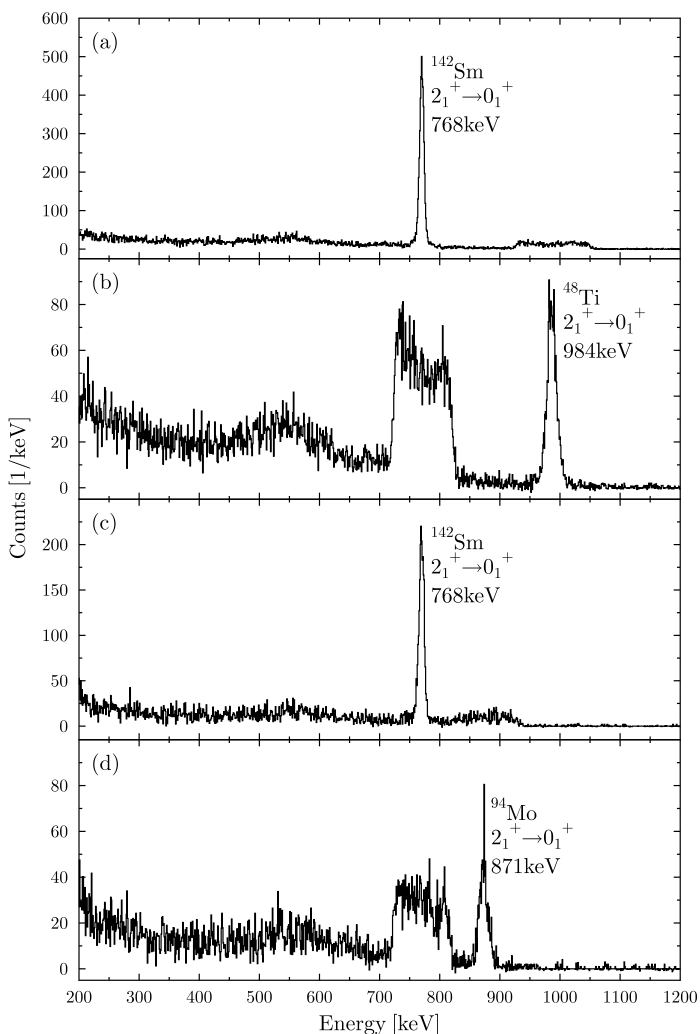


Figure 6.26.: Background-subtracted particle- γ coincidence spectra applying Doppler-correction with respect to the (a,c) projectile or (b,d) recoiling target nuclei showing the only observed transitions, namely the $2_1^+ \rightarrow 0_1^+$ transitions in ^{142}Sm at 768 keV, in ^{48}Ti at 984 keV, and in ^{94}Mo at 871 keV. The data was taken with laser ionization switched on all the time.

Ring (DSSD)	detected	θ_{lab} -range	^{142}Sm	^{94}Mo
4-7	target	30.8°-42.3°	595(25)	208(16)
9-15	target	44.8°-57.1°	593(25)	205(16)
4-6	projectile	30.8°-39.7°	983(32)	347(20)

Table 6.12.: Summary of the measured yields in the $^{94}\text{Mo}(^{142}\text{Sm}, ^{142}\text{Sm}^*)^{94}\text{Mo}^*$ reaction for the different ranges of scattering angles (not efficiency corrected).

	M_{20} [eb]	$B(E2)\uparrow$ [e^2b^2]	M_{22} [eb]	$Q(2_1^+)$ [eb]
^{48}Ti target	0.80(3)	0.64(5)	-	-
^{94}Mo target	0.88(9)	0.78(16)	-	-
weighted average	0.81(3)	0.65(5)	-	-
		= 30(2) W.u.		

Table 6.13.: Summary of the experimental results for ^{142}Sm for the single runs with Ti/Mo target and a weighted average. No statement can be made about the diagonal matrix element and thereby the quadrupole moment because of the general assumption of a limitation by the rigid rotor limits.

7 Discussion

The interpretation of the data is done in comparison with several theoretical predictions. The corresponding nuclear structure models and their mathematical treatment is explained in chapter 3. The discussion is split in two parts, the first one dealing with the phase transitional character of the Barium isotopic chain, the second covering the impact of the subshell structure in the $N=80$ isotones.

7.1 Shape transitions in the Barium isotopic chain

The properties of the ground states and low-lying excited states of many atomic nuclei can be attributed to the competition between the single-particle motion of their nucleons and their correlated or collective motion in terms of surface oscillations or rotation of a permanently deformed spatial distribution, see sec. 2.2. They reflect the structural changes when progressively more particles or holes are added to closed-shell nuclei, at first softening the (spherical) nuclear potential and then resulting in a deformed equilibrium shape. The isotopic chain of the even-N Barium isotopes exhibits rather peculiar patterns of structural evolution. When neutrons are successively removed from the $N = 82$ neutron-shell closure, the collectivity of Ba isotopes increases and drives their shape from spherical towards considerably deformation passing a transitional region with soft triaxiality [Cas00]. In the neutron-rich Ba isotopes with $N \geq 82$ the semi-magic ^{138}Ba is spherical, whereas ^{148}Ba has a $R_{4/2} = E(4_1^+)/E(2_1^+)$ ratio of ~ 2.98 , closer to a deformed axially-symmetric rotor. There is evidence for octupole correlations in the mass region around $A \sim 144$ ($Z = 56$, $N \sim 88$) that may influence the properties of nuclei already at low excitation energies since the resulting gain in binding energy has previously been argued to be sufficient to stabilize permanent octupole deformations [Phi86; BN96]. Still, low-lying energy levels with positive parity and electrical quadrupole transition probabilities of neutron rich Ba isotopes have been successfully described throughout the transitional region in the framework of the Monte Carlo shell model based on a quadrupole-plus-pairing approach [Shi01].

Indeed, in many nuclei deformation is predominantly of quadrupole nature [RS05]. Therefore a key observable to characterize the intrinsic nuclear shape in an even-even nucleus is the static quadrupole moment of the 2_1^+ state used in conjunction with a collective model [CT90]. Together with the E2-transition rates it provides a sensitive tool for the study of spherical-to-deformed shape transitions. Since for lifetimes below ~ 10 ns no direct method is available to determine the static quadrupole moment of excited nuclear states, the reduced electrical transition probabilities and lifetimes have to be used in order to obtain the spectroscopic quadrupole moment and nuclear deformation of these states [Ney03]. In particular, the *reorientation technique* [Boe65] has been used for the measurement of the spectroscopic quadrupole moment, in this thesis as well. The importance of precise lifetime information as a *sine qua non* for the interpretation of data from reorientation experiments has been demonstrated recently when determining the sign of the spectroscopic quadrupole moment of the 2_1^+ state of ^{70}Se [Hur07; Lju08].

Several efforts have been made to investigate experimentally the intrinsic deformation in the 2_1^+ states of the even-N Ba isotopes with $N < 82$ from measurements

Nucleus	τ [ps]	Experiment		Literature		Theory	
		Matrix elements M.E.	Matrix elements [eb]	B(E2) \uparrow ,Q [e^2b^2],[eb]	B(E2) \uparrow ,Q [e^2b^2],[eb]	B(E2) \uparrow ,Q MCSM	EDF
^{130}Ba	$^a 62.3(7)$	$\langle 2_1^+ E2 0_1^+ \rangle$ $\langle 2_1^+ E2 2_1^+ \rangle$	$1.093(21)$ $-1.06^{+0.07}_{-0.14}$	$1.195(46)$ $-0.80^{+0.05}_{-0.11}$	$^{a,b} 1.081(12)$ $^{-c} 1.02(16)$ or $^{-c} 0.09(16)$		-0.94
^{132}Ba	$^d 18.8(16)$	$\langle 2_1^+ E2 0_1^+ \rangle$ $\langle 2_1^+ E2 2_1^+ \rangle$	$0.990(043)$ $-0.10(17)$	$0.98(9)$ $-0.08(13)$	$^e 0.897(26)$ n.m.		-0.38
^{140}Ba	$^f 10.4^{+2.2}_{-0.8}$	$\langle 2_1^+ E2 0_1^+ \rangle$ $\langle 2_1^+ E2 2_1^+ \rangle$	$^{b,f} 0.696^{+0.027}_{-0.073}$ $-0.69(45)$	$^{b,f} 0.484^{+0.038}_{-0.101}$ $-0.52(34)$	$^{b,g} 0.45(19)$ n.m.	0.33	0.594 -0.522
^{142}Ba	$^g 95(5)$	$\langle 2_1^+ E2 0_1^+ \rangle$ $\langle 2_1^+ E2 2_1^+ \rangle$	$^{b,g} 0.830(20)$ $-0.51(38)$	$^{b,g} 0.688(36)$ $-0.39(29)$	$^{b,g} 0.688(36)$ n.m.	0.71	-0.789

a: from RDDS measurement [Stu00]

b: deduced from lifetime

c: from reorientation measurement [Bur89]

d: deduced from Coulex measurement of this work

e: from Coulex measurement [Bur85]

f: from DSAM of this work, see subsec. 6.5.1

g: from electronic timing [MGM89]

Table 7.1.: Comparison of experimental results for the transition $2_1^+ \rightarrow 0_1^+$ in the Barium isotopes with theoretical calculations. The previously measured values are indicated by "Literature" and published in [MGM89]. "Theory" values belong to Monte Carlo shell model calculations [Shi01] and EDF calculations [Rod11] including beyond mean-field effects. The first column lists directly measured lifetimes for ^{132}Ba a deduced value is given for comparison) whereas the sources are given in the footnote.

of the static quadrupole moments [Sim67; KS72; Nei74; BDH84; Bur89]. However, the ambiguity of the results in both, sign and magnitude of the measured $Q(2_1^+)$ moments, made the interpretation most difficult. Whereas a prolate deformation for $^{134,136,138}\text{Ba}$ was indicated by the measurements from Kerns et al. [KS72] and for $^{130,134}\text{Ba}$ from Neimann [Nei74], oblate deformation was suggested for $^{130,134,136}\text{Ba}$ by Towsley et al. [Tow73] and for ^{136}Ba by Bechara et al. [BDH84] as well. In a systematic study for $^{130,134,138}\text{Ba}$ using the reorientation technique in Coulomb excitation it was intended to elucidate the situation [Bur89] but the missing information about the sign of the interference term (see sec. 6.4) lead to an ambiguity in the quadrupole moments. This work finally gives an approach to resolve this ambiguity and first results of unique quadrupole moments are presented.

The experimental results are compared to results from the Monte-Carlo shell model [Shi01] and in the case of ^{140}Ba to predictions from EDF calculations [Rod11] as well. The newly measured lifetime $\tau(2_1^+) = 10.4_{-0.8}^{+2.2}$ ps in ^{140}Ba with significantly improved accuracy over the current literature value [MGM89] corresponds to a $B(E2)\uparrow$ value of $0.484_{-0.101}^{+0.038}e^2b^2$. This is close to the $B(E2;0_1^+ \rightarrow 2_1^+)$ value of $0.412(8)e^2b^2$ in ^{136}Ba , which is the neutron particle-hole partner nucleus to ^{140}Ba with respect to the $N=82$ shell closure. The new result affirms the observation of a distinct mirror symmetry in the electrical transition probabilities of the first excited states in the even- N Ba isotopes with respect to the $N=82$ shell closure when measured in Weisskopf units, see fig. 7.1 (a,e). In particular, the irregular pattern for the $B(E2)\uparrow$ values discovered in the $N=82$ particle-hole partners ^{130}Sn - ^{134}Sn and ^{132}Te - ^{136}Te [Rad02], attributed to a reduced neutron pairing gap in the latter isotopes [Ter02], does not exist in their nearby isotones ^{136}Ba - ^{140}Ba . The electrical transition probabilities in the even-even Ba isotopes exhibit instead an astonishing symmetry around $N=82$. This is in contrast to the evolution of the excitation energies, $E(2_1^+)$, as a function of neutron number. For the latter a considerable asymmetry around $N=82$ is observed. The ratio $E(N = 82 - X_N)/E(82 + X_N)$ deviates from unity by up to 150% (fig. 7.1 (d)). The different structure of Ba isotopes above and below the $N=82$ shell closure is also emphasized by the evolution of the quadrupole moments, $Q(2_1^+)$, as shown in fig. 7.1 (c).

The measured spectroscopic quadrupole moments of the $^{130,132,140,142}\text{Ba}$ isotopes are all negative, representing prolate deformation. The finding of a positive interference term for $^{130,132}\text{Ba}$ (see sec. 6.4) can be most probably extended to the whole chain, which would also solve the ambiguity for $^{134,136,138}\text{Ba}$. For $^{134,138}\text{Ba}$ the small prolate deformation is in agreement with conventional nuclear structure models, that predict spherical shapes around shell closures, and the Monte Carlo Shell Model. The slightly oblate prediction of the MCSM for the 2_1^+ state of ^{136}Ba is very surprising, either the MCSM predicts the wrong deformation or the

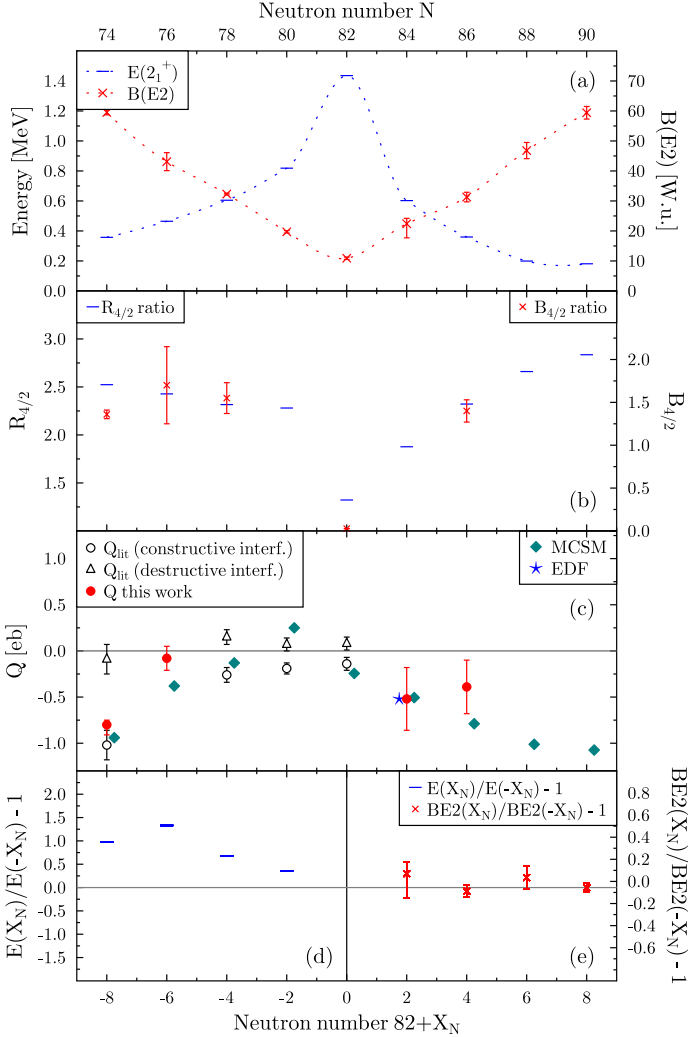


Figure 7.1.: Systematics of excitation energy $E(2_1^+)$ and $B(E2)$ value (a), $R_{4/2}$ and $B_{4/2}$ ratios (b), and $Q(2_1^+)$ moment (c) in the Ba isotopes with $130 \leq A \leq 146$. The ratio $E(2_1^+; 138 - X_N)/E(2_1^+; 138 + X_N) - 1$ is shown (d) and analogously $B(E2; 138 + X_N)/B(E2; 138 - X_N) - 1$ (e) to highlight the specific mirror symmetry of the transition strengths around $N = 82$. All $B(E2)$ values are given in W.u. in order to account for a simple size-effect.

interference term is negative (destructive interference) for this specific nucleus. Unfortunately this isotope could not be measured in the presented campaign.

From the investigation of mixed-symmetry states (MSSs) by T. Möller [Möl13] it is found that the shape transitional point in the Barium ($Z = 56$) isotopic chain below $N = 82$ is situated near $^{130,132}\text{Ba}$. This finding is supported by the measured quadruple moments. There is a strong increase from ^{130}Ba (prolate, near rigid-rotor limit) to ^{132}Ba (just slightly prolate) in the deformation of the 2_1^+ state. This could also be interpreted as another signature of a shape transition beside the $R_{4/2}$ ratio, e.g., supported by the agreement with the MCSM calculations.

On the neutron-rich side with $N \geq 82$ the mid-size prolate deformation of the 2_1^+ state of ^{140}Ba with a spectroscopic quadrupole moment of $Q(2_1^+) = -0.52(34)\text{eb}$ agrees remarkably well to the predictions of Monte-Carlo shell model calculations and the energy density functional (EDF, see below). The neighboring ^{142}Ba with $Q(2_1^+) = -0.39(29)\text{eb}$ supports the trend towards a more prolate deformation although it is a little smaller in magnitude. One has to consider that both measurements have an error larger than 50%. The MCSM, using a two-body effective interaction including monopole and quadrupole pairing, quadrupole-quadrupole interactions and axially-symmetric bases, describes microscopically the evolution of properties of quadrupole collective states throughout the shape transition path from ^{138}Ba to ^{150}Ba [Shi01] with the variation of valence particles only. Although the calculated $B(E2) \uparrow$ value in ^{140}Ba is smaller than the experimental result the spectroscopic quadrupole moments of $^{140,142}\text{Ba}$ are in good agreement, compare tab. 7.1 and fig. 7.1 for this discussion.

A more detailed inspection of ^{140}Ba was done, compare ref. [Bau12b] of the author. The MCSM level scheme in fig. 7.2(c) agrees quite well with the experimental one (b), including the moment of inertia and the inverted order of the 0_2^+ and 2_2^+ states. The agreement of the yrast level schemes is slightly improved in comparison to fig. 1(a) of ref. [Shi01] by including the triaxial degree of freedom. As discussed in sec. 3.3 the two major limitations of the EDF are the conservation of parity and time-reversal symmetries of the intrinsic wave functions. The first one restricts the study to positive-parity states and neglects the influence of the octupole degree of freedom that does play a role in this region. However, axial mean-field calculations with the Gogny interaction show that static octupole deformations are not found in the potential energy surface for ^{140}Ba [ER90; Rob10; MR94]. The second restriction limits the description of the moments of inertia and, therefore, the quantitative precision of the energy levels [Zdu07; LRV04]. In fig. 7.2(a) the results of the calculated spectrum are shown. These levels are sorted in bands according to their $B(E2)$ values. It is observed that the ground-state band corresponds to a sequence of states with positive parity and $\Delta J = 2$. They are almost equally spaced, indicat-

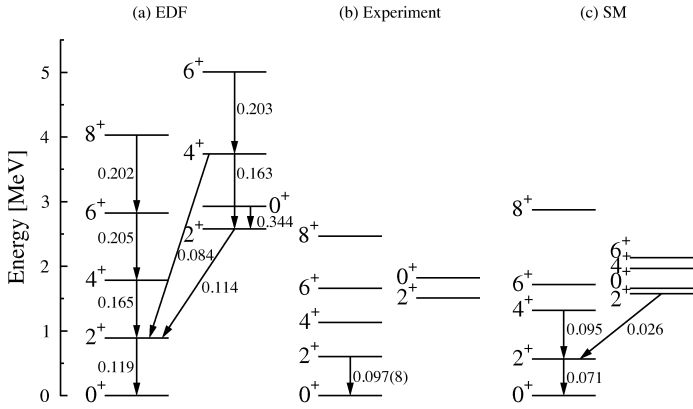


Figure 7.2.: (a) Energy levels of ^{140}Ba calculated with the Gogny D1S density functional including beyond mean-field effects. (b) Experimental level energies taken from [Ens] and $B(E2) \downarrow$ from this work. (c) Exact MCSM calculations using the P+QQ interaction [Shi01].

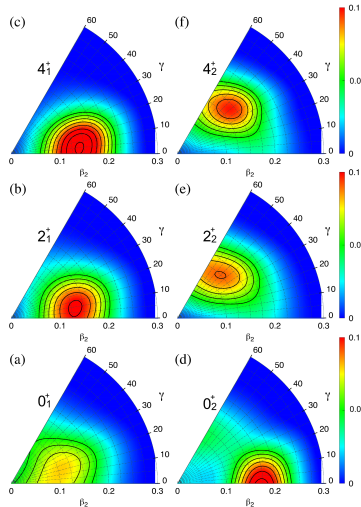


Figure 7.3.: Distribution of probability in the triaxial (β_2, γ) plane for the states belonging to the first two bands of ^{140}Ba , calculated with the Gogny D1S density functional including beyond mean-field effects.

ing a vibrational character. The second band is also compatible with a vibrational band for the levels 2_2^+ , 4_2^+ , 6_2^+ . However, the band head does not correspond to the 0_2^+ state which is higher in excitation energy than the 2_2^+ . It is important to note that the correct ordering of these levels is only reproduced if the triaxial degree of freedom is included. The experimental levels also exhibit a vibrational ground-state band and the 2_2^+ state is situated below the 0_2^+ state. Nevertheless, although a good qualitative description of the data is obtained, the theoretical spectrum appears more stretched. This is a common feature of this kind of method and is due to a poor description of the moments of inertia whenever the time-reversal symmetry is conserved, like in the present case [ER04]. Concerning the reduced transition probabilities, the calculation predicts that the 0_2^+ state decays mainly to the 2_2^+ and the latter one to the 2_1^+ state both possibly indicating pronounced γ -softness. It is also observed that the calculated $B(E2; 2_1^+ \rightarrow 0_1^+)$ value is higher than the experimental value obtained in this work. No effective charges are used in these EDF methods.

To analyze the intrinsic shapes of the states given in the spectrum and to study their corresponding collective wave functions fig. 7.3 shows the distribution of probability of having a given deformation in the (β_2, γ) plane for different states J_σ^+ . In the figure, the vertex corresponds to the spherical point, $\gamma = 0^\circ(60^\circ)$ directions to prolate (oblate) axially symmetric shapes and the rest of the plane to purely triaxial shapes. Here one sees clearly that the ground state presents a slightly deformed, near spherical configuration $\beta_2 \sim 0.1$ with substantial γ -softness and the 2_1^+ and 4_1^+ states belonging to this band have their probabilities peaked at a larger, more prolate deformed shape around $\beta_2 \sim 0.13, \gamma = 5^\circ$ -similar distributions are also obtained for 6_1^+ and 8_1^+ states (not shown). On the other hand, the first excited 0_2^+ state presents a maximum at $(\beta_2 = 0.17, \gamma = 0^\circ)$ while the 2_2^+ and 4_2^+ states show maxima located in the oblate-triaxial part at $(\beta_2 = 0.13, \gamma = 45^\circ)$. The differences and similarities between the corresponding collective wave functions help to understand the values of the transition probabilities given in fig. 7.2. In addition, this result is in agreement with the most probable prolate character of the 2_1^+ found experimentally (fig. 7.1).

7.2 Shell stabilization in the N=80 isotones

The mechanism, which leads to the formation of nuclear collective states out of the individual motion of many nucleons, is one of the major subjects in nuclear structure physics. There are clear relations between the collective properties of even-even nuclei, *e.g.*, the excitation energy of the 2_1^+ state and the $B(E2; 2_1^+ \rightarrow 0_1^+)$ transition strength [RJT01], and the number of nucleons in the valence shell. The global behavior of these quantities between the major shells as a function of the nucleon number is well understood in the frameworks of both collective and microscopic models. One could expect that these general trends in the collective properties between the major shells are modulated by the subshell structure. However, it is usually believed that the pairing correlations with an energy scale of about 2 MeV, smear out and dissolve the subshell structure as long as the separation energies between the subshells are only about few hundred keV.

The recently observed evolution [PBL08] of the isovector quadrupole-collective valence-shell excitations in the N=80 isotones, the so called mixed-symmetry states (MSS) [Iac84], a special class of collective states, suggests that the properties of collective states may be more strongly influenced by the underlying subshell structure than previously thought [Rai06]. In this case there is one single isolated one-phonon $2_{1,ms}^+$ state observed in ^{132}Te [Dan11], ^{134}Xe [Ahn09] and ^{136}Ba [Pie98]. It can be explained by the fact that in these isotones the proton excitations mostly happen in the partially filled $g_{7/2}$ orbital, *i.e.* they are *shell stabilized*. However, once the $\pi(g_{7/2})$ orbital is completely filled the one-phonon MSS fragments in ^{138}Ce [Rai06] and reveals a *lack of shell stabilization* at $Z=58$ (see fig. 7.4).

The question whether this effect is also detectable through the properties of the fully-symmetric states is answered by the presented measurements of the absolute transition strengths $B(E2; 2_1^+ \rightarrow 0_1^+)$ of ^{140}Nd and ^{142}Sm , which complement the row of the N=80 isotones. The obtained experimental results show a clear deviation of the absolute $B(E2; 2_1^+ \rightarrow 0_1^+)$ strength of ^{138}Ce ($Z=58$) from the expected collective behavior, that is more or less continued by the new results. However, microscopic models seem unable to reproduce this deviation, which prompts for a further theoretical development. The experimental results are compared to state-of-the-art microscopic calculations, the quasi-particle phonon model (QPM, sec. 3.2) and large-scale shell-model calculations (LSSM, sec. 3.1.1), compare [Bau13] for the following discussion.

The QPM [Iud12] is capable to describe the anharmonic features of collective modes as well as multiphonon excitations. Since the constituent phonons include two-quasiparticle excitation covering a very large energy spectrum, it is possible to use effective charges very close to the bare values ($e_\pi = 1.05$ and $e_\nu = 0.05$). The

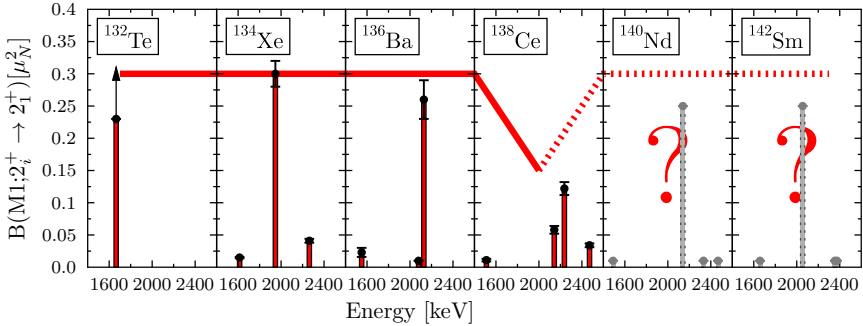


Figure 7.4.: Systematics of the $B(M1; 2_i^+ \rightarrow 2_1^+)$ strength in the $N=80$ isotones. In contrast to the $2_{1,ms}^+$ states in the neighboring isotones the $2_{1,ms}^+$ state of ^{138}Ce is strongly mixed and it is a priori not clear how the trend continues in ^{140}Nd and ^{142}Sm .

Hamiltonian parameters used here are the same ones adopted in a previous calculation [LIST08] to optimize the description of the fully symmetric states (FSS) and MSSs of the $N=80$ chain up to $Z=58$. Therefore, the calculation has a predictive power for ^{140}Nd and ^{142}Sm .

The LSSM adopts a model space in which the valence protons and neutrons, treated respectively as particles and holes external to a $Z=50$ and $N=82$ core (^{132}Sn), are distributed among the shells $\{2d_{5/2}, 1g_{7/2}, 2d_{3/2}, 3s_{1/2}, 1h_{11/2}\}$. The calculations use a realistic two-body Hamiltonian (a renormalized G-matrix derived from the CD-Bonn potential) with the same single-particle (hole) energies adopted for the Xe isotopes [Bia11]. More specifically, the neutron-hole energies were taken from the levels of ^{135}Xe , while the proton energies were the same adopted to study the spectra of ^{108}Sn and ^{133}Xe [AIP03]. Thus, the LSSM calculations are completely parameter free and fully predictive for the whole $N=80$ chain. On the other hand, the shell model space does not include high-energy and core excitations, whose effects are incorporated into the large effective charges $e_\pi = 1.6$ and $e_\nu = 0.7$, the same adopted for the Xe isotopes [Bia11].

In summary, the parameters of both models have been adapted to the description of lighter nuclei than ^{140}Nd for which their results can be considered as predictions. The QPM as well as the shell-model calculations provide a good agreement of the excitation energies for the 2_x^+ states of ^{140}Nd (cf. fig. 7.5) including the suspected 2_{ms}^+ states [Gla10]. The general trend of growing $B(E2; 2_1^+ \rightarrow 0_1^+)$ strength in the $N=80$ isotones moving away from the $Z=50$ shell closure as shown in fig. 7.6 is

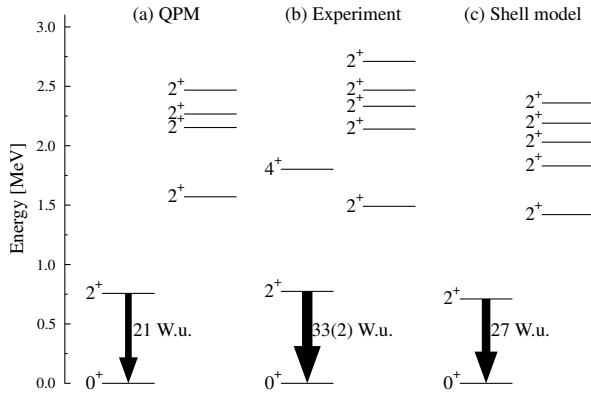


Figure 7.5.: Parts of the experimental level scheme for ^{140}Nd is shown (b) together with the calculated ones from the (a) QPM and (c) shell model [Bia12]. The illustration concentrates on the 2_x^+ states.

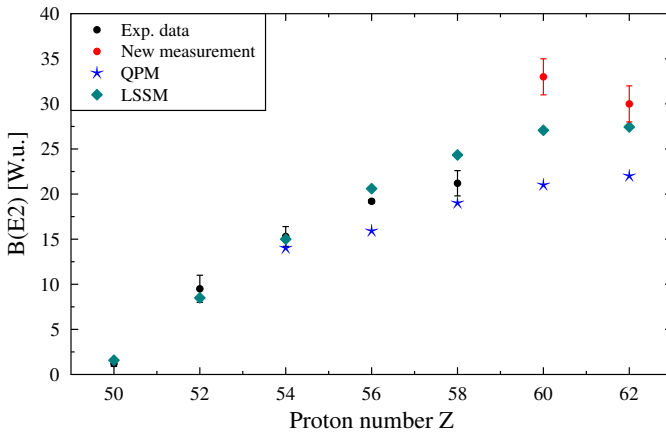


Figure 7.6.: Systematics of $B(E2)$ values for the first excited 2_1^+ states in the even $N=80$ isotones from $Z=50$ (Sn) to $Z=62$ (Sm). The existing experimental data [Sin01; Dan11; Jak02; BDH84; RJT01] is presented including the new values for ^{140}Nd and ^{142}Sm in comparison with large-scale shell-model calculations [Bia12] as well as the quasi-particle phonon model [LIST08].

expected due to the increase in collectivity when adding more and more valence protons N_π . However, the QPM predicts smaller $B(E2; 2_1^+ \rightarrow 0_1^+)$ values of 21 W.u. (22 W.u.) compared to the experimentally found value of 33(2) W.u. (30(2) W.u.) in the case of ^{140}Nd (^{142}Sm). The shell-model calculations predict a strength of ≈ 27 W.u. for both isotopes but still below the measured values. Both calculations describe a smoother increase in agreement with the smaller $B(E2)$ value of ^{138}Ce and do not reproduce the larger values of ^{140}Nd and ^{142}Sm . Ignoring the $B(E2)$ value of ^{138}Ce all other values, including the one for ^{140}Nd , seem to increase linearly up to ^{140}Nd and then saturate with ^{142}Sm .

This linear behavior can be understood as a $N_\pi N_\nu$ dependence. The $N_\pi N_\nu$ valence correlation scheme from ref. [CZ96] describes the linear increase of collectivity with $N_\nu = 2$ (2 valence neutron holes) and $N_\pi = 0, 2, 4, \dots$ for the protons. In that approach nuclear data is parameterized to explicitly emphasize the valence shell proton-neutron (p-n) interaction. It is assumed that the onset of collectivity, configuration mixing and deformation stems solely from the p-n interaction in the valence shell. This interaction is fairly long ranged, orbit independent, and relevant only for the valence protons and neutrons. These extreme assumptions, averaged over many valence nucleons, have proven to be reasonable. By applying this scheme to the $N=80$ isotones a consistent description of the experimental data except for $Z=58$ and $Z=62$ as indicated by the dashed line in fig. 7.7 is obtained. The maximum would be at mid shell ($Z=66$) from where on proton holes have to be counted and the linear trend turns downwards. One accounts for the single particle degrees of freedom only through the number of valence bosons, which is known to be a limited approximation. On the other hand data on the one-phonon mixed-symmetry states strongly suggest that the single-particle degrees of freedom can influence the collective properties dramatically at least for the mixed-symmetry states through the shell stabilization effect [Rai06].

In an extreme shell model scenario, considering the valence protons to occupy only the $(1g_{7/2})$ and $(2d_{5/2})$ orbitals, the $B(E2)$ strength vanishes at $Z=50$, $Z=58$, $Z=64$ and it has a maximum at mid-shell, indicated by the solid curves in fig. 7.7. The experimental data can be interpreted as a convolution of the both presented extreme scenarios. The suppression of the transition strength in ^{138}Ce with respect to the $N_\pi N_\nu$ behavior is explained by the $Z=58$ subshell closure. The slightly decreasing, almost constant strength of ^{142}Sm (in comparison to ^{140}Nd) is explained on the one hand by the same number of valence proton particles (Nd) and holes (Sm), namely 2, with respect to the $\pi(2d_{5/2})$ orbital. On the other hand Sm ($Z=62$) is already quite close to mid-shell ($Z=66$) with respect to the major shell between the magic numbers at $Z=50$ and $Z=82$. This saturation of transition strength near mid-shell, building a distinct plateau, is observed in several isotopic chains.

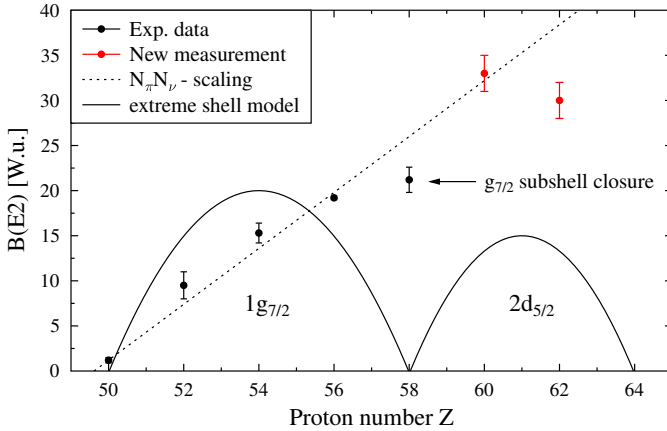


Figure 7.7.: Systematics of $B(E2)$ values in W.u. for the first excited 2_1^+ states in the even $N=80$ isotones covering the range of the $\pi g_{7/2}$ and $\pi d_{5/2}$ orbitals. The existing experimental data is presented as in fig. 7.6 with a schematic illustration of a linear $N_\pi N_\nu$ dependence (dashed) and an extreme shell model case (solid lines).

However, the local suppression of $B(E2)$ strength in ^{138}Ce is not reproduced in the shell model calculations. Such a quenching might be the outcome of a subtle competition between the single-particle energy levels, responsible for the gap between different subshells, and the two-body correlations, especially pairing, which tend to smooth out the effects of the subshell structure. This hypothesis, suggested by the extreme shell model picture, can be tested by fine tuning the single-particle levels used in the LSSM calculations [Bia11] so as to counterbalance the smoothing action of pairing. Alternatively, one may surmise that the core polarization produces smaller effective charges in correspondence of a subshell closure. In order to test such a suggestion, one should compute explicitly the effective $E2$ operators within the linked cluster expansion theory which is known to generate different effective charges for different subshells [IRW74]. However, it was pointed out [Bia12; Bia11] that a calculation in an enlarged shell model space, which includes core excitations, is not feasible.

In summary, the measured $B(E2)$ values of ^{140}Nd and ^{142}Sm are compared to recent large-scale shell model calculations [Bia12] as well as to the quasiparticle phonon model in connection to the systematics of the $N=80$ isotones [Bia12;

LIST08]. In both models, the computed $B(E2)$ strength in the stable $N=80$ isotones increases smoothly with Z . This trend is consistent with the experiments apart from some deviations in the heavier isotones, where the measured data do not have a smooth behavior. In fact, the $E2$ transition is suppressed to some extent in ^{138}Ce and enhanced in ^{140}Nd . This anomalous behavior seems to be ascribed to the filling of the $\pi(g_{7/2})$ subshell for $Z=58$. That shell effect is missing in the QPM, which tends to underestimate systematically the strength, and in the LSSM, which yields a larger $B(E2)$ value as compared to the measurement in ^{138}Ce and a smaller one as compared to the data in ^{140}Nd . While both models predict gradually increasing $B(E2)$ values with proton number, they fail to describe the measured sudden increase of the $B(E2)$ value from $Z=58$ to 60. These discrepancies may be cured within the shell model by a more refined treatment of the single-particle energies capable of inducing a more pronounced subshell structure or by taking explicitly into account the excitations of the core.

A CLX input file

```
392 MeV 140Nd --> 48Ti @REX-Isolde
1110111
6 2 0
0 0 0
60 140
22 48
1
392
73 140 1
1 0 0.000 1 0
2 2 0.773 1 0
3 2 1.490 1
4 2 2.140 1
5 2 2.259 1
6 2 2.399 1

1 2 0.61 2
1 3 0.04 2
1 4 0.27 2
1 5 0.30 2
1 6 0.09 2

2 2 0. 2
2 3 0.72 2
2 4 0.37 2
2 5 0.14 2
2 6 0.28 2

2 3 0.173 -1
2 4 0.387 -1
2 5 1.072 -1
2 6 0.742 -1

3 3 0. 2
4 4 0. 2
5 5 0. 2
6 6 0. 2
```



B Gosia input file

A GOSIA2 calculation requires two similar files, one for projectile and one target excitation. Here the projectile file, indicated by the number 1 in the first line, is shown for the analysis of $^{140}\text{Nd} \rightarrow ^{48}\text{Ti}$. The input file is divided in the following sections, which are partly commented in the file as well:

OP,FILE List of necessary files

OP,TITL Title

OP,GOSI Input section for levels (LEVE), matrix elements (ME), experimental conditions (EXPT), and further control and print commands

OP,YIEL Input of conversion coefficients, detector geometry, and already known spectroscopic data

OP,RAW Definition of detector clusters and efficiency

OP,INTI Integration commands including stopping powers and angular information (has to be replaced with OP,MINI for minimization in a later step)

```
1
OP,FILE
25,3,1 ! input file
140Nd_Ti.inp
22,3,1 ! output file
140Nd_Ti.out
26,3,1 ! -> target (GOSIA2)
48Ti.inp
3,3,1 ! here the raw yields come into play (in this case already efficiency corrected)
140Nd_Ti.yld
4,3,1 ! the corrected yields will reside here
140Nd_Ti.cor
27,3,1 ! -> target (GOSIA2)
48Ti.map
7,3,1 ! q parameter map for m substates
140Nd_Ti.map
8,3,1
MB_Nd.raw
9,3,1 ! gamma detector corrected
MB_Nd.gdt
11,3,2
crf.dat
12,3,1 ! best fit matrix elements
140Nd_Ti.bst
32,3,1 ! -> target (GOSIA2)
48Ti.bst
```

```

13,3,1
cnor.dat
23,3,1
140Nd_Ti.raw
0,0,0
OP,TITL
  140Nd on 48Ti (1.4mg/cm2) at 399 MeV == Projectile Excitation
OP,GOSI
LEVE
  1,1,0.,0.0000
  2,1,2.,0.7737
  3,1,4.,1.8019 ! buffer state
0,0,0,0
ME
  2,0,0,0,0
  1 2 0.81 0 5
  2 2 -0.1 -5 5
  2,3,0.5, 0.01,5.0 ! 4+1->2+1 g.b.
  3,3,0.01,5.0, 5.0 ! fix Q of 4+1
  0,0,0,0,0
EXPT
3,60,140
-22,48,360.,19.585,3,1,0,0,360,0,1
-22,48,360.,19.275,3,1,0,0,360,1,2
-22,48,360.,17.855,3,1,0,0,360,1,3
CONT
SPL,1.
LCK,
0,0
PRT,
3,0
4,0
8,1 ! comparison of calculated and experimental yield
10,0 ! kinematics for each integration mesh-point
11,0 ! gamma-yields for each integration mesh-point
12,0 ! q parameter map
13,1 ! normalization constants
14,1 ! deorientation effect
15,1 ! mean lifetimes
16,1 ! all possible calculated yields
18,0 ! interpolated internal conversion coefficients
20,1 ! raw yields -> tape 23
0,0
END,

OP,YIEL
1
7,1
0.050,0.070,0.100,0.200,0.500,1.000,1.500
2
30.4,8.13,2.19,0.196,0.01177,0.00224,0.001065
22,22,22
1,2,3,4,5,6,7,8,9,10,11,12,13,14,15,16,17,18,19,20,21,22
123.5,147.8, 50.7, 76.8, 71.4, 45.4, 71.4, 54.2,116.6,135.3,141.5,115.7,143.3,124.6, 50.0, 75.7, 56.7,...
160.4,141.2, 49.0, 56.4, 28.9,142.1,131.9,107.9, 47.3, 72.8, 31.8,262.4,260.8,232.0,244.4,233.0,210.9,...
1,2,3,4,5,6,7,8,9,10,11,12,13,14,15,16,17,18,19,20,21,22
123.5,147.8, 50.7, 76.8, 71.4, 45.4, 71.4, 54.2,116.6,135.3,141.5,115.7,143.3,124.6, 50.0, 75.7, 56.7,...
160.4,141.2, 49.0, 56.4, 28.9,142.1,131.9,107.9, 47.3, 72.8, 31.8,262.4,260.8,232.0,244.4,233.0,210.9,...
1,2,3,4,5,6,7,8,9,10,11,12,13,14,15,16,17,18,19,20,21,22
123.5,147.8, 50.7, 76.8, 71.4, 45.4, 71.4, 54.2,116.6,135.3,141.5,115.7,143.3,124.6, 50.0, 75.7, 56.7,...
160.4,141.2, 49.0, 56.4, 28.9,142.1,131.9,107.9, 47.3, 72.8, 31.8,262.4,260.8,232.0,244.4,233.0,210.9,...
2,1 ! normalisation transition
1 ! data sets
100 ! upper limit as a fraction of above transition
1 ! Normalisation of experiment
1 ! data sets
100 ! upper limit as a fraction of above transition
1 ! Normalisation of experiment

```




C C++ program for calculating correlated errors with Gosia2

```
/*
This piece of software is designed to calculate the error for a certain matrix element in a Gosia2
calculation by the "Brute force total correlated error estimation" as described here:
http://www-user.pas.rochester.edu/~gosia/mediawiki/index.php/Error\_estimation#
Correlated\_errors\_using\_gosia2

The Gosia2 input file of the projectile, we are interested in, is handed over to the program just
after the last regular MINI fit procedure, just OP,REST removed but with OP,MINI. The rest is then
all changed by the program. The target input file must have the OP,REST and OP,MINI command in place.
*/

#include <iostream> // IO
#include <sstream>
#include <fstream> // ifstream and ofstream
#include <cstdio>
#include <iomanip>
#include <cmath>
#include <cstring>
#include <string> // use strings and some IO with them
#include <cstdlib>

using namespace std;
using std::istringstream;

int main(int argc, char **argv)
{
    if (argc != 2)
    {
        cout << "Usage: " << argv[0] << " input_filename" << endl;
        return 1;
    }

    istringstream filenamein(argv[1]);
    string filename, outfilename, targetfilename, targetoutfilename;
    string best, errorfile;
    filenamein >> filename;
    cout << "Calculate the error from file: " << filename << endl;

    ifstream in, in2, inb;
    ofstream out;

    ifstream inPO, inTO; // look in output files for chisq
    ofstream outchi; // write-out the chisq values

    in.open(filename.c_str(), ios::in); // now look at that Gosia input file

    int no;
    string line;

    in >> no;
    cout << endl;
    cout << "Number of file:          " << no << endl;

    while (!in.eof())
```

```

{
    getline(in, line);
    if(line.find("22,3,1")!=string::npos) in>>outfile;
    if(line.find("26,3,1")!=string::npos) in>>targetfilename;
    if(line.find("12,3,1")!=string::npos) in>>best;
}
in.close();
in2.open(targetfilename.c_str(), ios::in);
while (!in2.eof())
{
    getline(in2, line);
    if(line.find("22,3,1")!=string::npos) in2>>targetoutfile;
}
in2.close();

errorfile=filename;
size_t sz=errorfile.size();
errorfile.replace(sz-4,4,"_error.dat");
system((string("rm")+errorfile).c_str());
cout << "Old chi-sq table " << errorfile.c_str() << " was cleaned." << endl;

cout << "Output file: " << outfile << endl;
cout << "Input file target exc.: " << targetfilename << endl;
cout << "Output file target exc.: " << targetoutfile << endl;
cout << "Chi-sq table stored in: " << errorfile << endl;
cout << endl;

double m20start;
double step=0.01;
double step2=0.1;
int iter=19;

inb.open(best.c_str(), ios::in);
inb>>m20start;
inb.close();

cout << "Starting matrix element: " << m20start << endl;
cout << "Will use stepwidth of: " << step << endl;

int s1, s2;
double m20, m22, l1, ul;
double m20i, m22j;

for (int i=0; i<iter; i++) // m20 loop
{
    m20i=m20start+step*(iter-1)/2-i*step;

    for (int j=0; j<iter; j++) // m22 loop
    {
        m22j=-(iter-1)*step2/2+j*step2-1.0;

        in.open(filename.c_str(), ios::in); // now manipulate Gosia input file
        out.open("temp.inp", ios::out);

        while (!in.eof())
        {
            getline(in, line);
            if(line.find("ME")!=string::npos)
            {
                out << line << endl;
                getline(in, line);
                out << line << endl;
                in >> s1 >> s2 >> m20 >> l1 >> ul;
                out << " " << s1 << " " << s2 << " " << m20i << " " << ul << " " << ul << endl;
                in >> s1 >> s2 >> m22 >> l1 >> ul;
                out << " " << s1 << " " << s2 << " " << m22j << " " << ul << " " << ul << endl;
                getline(in, line);
                getline(in, line);
            }
        }
    }
}

```

```

}
if (line.find("NTAP")!=string::npos)
{
    out << " 3   ! NTAP" << endl;
    getline(in, line);
}
if (line.find("OP,MINI")!=string::npos)
{
    getline(in, line);
    break;
}
else
{
    out << line << endl;
}
}
}

out.close();
in.close();

system("cat temp.inp INTI.txt > temp2.inp");
system((string("mv temp2.inp ") + filename).c_str());
system((string("gosia2 < ") + filename + string("2>&1 1>/dev/null")).c_str()); // here calculate
the corrected yields, keeping the M.E. constant

in.open(filename.c_str(), ios::in); // now manipulate Gosia input file
out.open("temp.inp", ios::out);

while(!in.eof())
{
    getline(in, line);
    if (line.find("NTAP")!=string::npos)
    {
        out << " 4   ! NTAP" << endl;
        getline(in, line);
    }
    if (line.find("OP,INTI")!=string::npos)
    {
        getline(in, line);
        break;
    }
    else
    {
        out << line << endl;
    }
}

system("cat temp.inp MINI.txt > temp2.inp");
system((string("mv temp2.inp ") + filename).c_str());
system((string("gosia2 < ") + filename + string("2>&1 1>/dev/null")).c_str()); // here doing the
minimization, keeping the M.E. constant

out.close();
in.close();

char chiP[20], chiT[20];

inPO.open(outfilename.c_str(), ios::in);
inTO.open(targetoutfilename.c_str(), ios::in);

outchi.open(errorfile.c_str(), ios::app);

while(!inPO.eof())
{
    getline(inPO, line);
    if (line.find("CHISQ=")!=string::npos)
    {
        line.copy(chiP, 12, 17);
    }
}

```

```

        chiP[12]='\0';
        break;
    }
}

while(!inTO.eof())
{
    getline(inTO, line);
    if(line.find("CHISQ")!=string::npos)
    {
        line.copy(chiT,12,17);
        chiT[12]='\0';
        break;
    }
}

inPO.close();
inTO.close();

outchi << m20i << " " << m22j << " " << chiP << " " << chiT << endl;
outchi.close();

cout << "Status: Iteration " << i*iter+j+1 << " out of " << iter*iter << " was done." << endl;
} // end of m22 loop

outchi.open(errorfile.c_str(),ios::app);
outchi << endl; // gnuplot likes an empty line after each block
outchi.close();

cout << "After step " << (i+1)*iter << " the error data looks the following:" << endl;
system((string("cat ") + errorfile).c_str());

} // end of m20 loop

cout << "The error file " << errorfile.c_str() << " was successfully calculated." << endl;
}

```

D Formalism of electromagnetic transitions strengths

$$\text{Width: } \Gamma = \frac{\hbar}{\tau} = \sum_i \Gamma_i \quad \text{Lifetime: } \frac{1}{\tau} = \sum_i \frac{1}{\tau_i} = \sum_i \frac{\Gamma_i}{\hbar} \quad (\text{D.1})$$

For unipolar transitions:

$$\frac{1}{\tau} = \frac{\Gamma}{\hbar} = \frac{8\pi}{\hbar} \frac{\lambda + 1}{\lambda [(2\lambda + 1)!!]^2} \cdot \left(\frac{E_\gamma}{\hbar c} \right)^{2\lambda+1} \cdot B(\pi\lambda; I_i \rightarrow I_f) \quad (\text{D.2})$$

$$\Gamma = c_{\pi\lambda} \left(\frac{E_\gamma}{\text{MeV}} \right)^{2\lambda+1} \cdot B(\pi\lambda; J_i \rightarrow J_f) \quad (\text{D.3})$$

with

$$c_{E1} = 1.0466609 \frac{\text{meV}}{10^{-3} e^2 \text{fm}^2}$$

$$c_{M1} = 11.574 \frac{\text{meV}}{\mu_N^2}$$

$$c_{E2} = 8.0638146 \frac{\text{meV}}{e^2 \text{b}^2}$$

$$c_{M2} = 8.9167 \cdot 10^{-4} \frac{\text{meV}}{\mu_N^2 \text{b}}$$

$$c_{E3} = 3.7566888 \cdot 10^{-4} \frac{\text{meV}}{e^2 \text{b}^3}$$

$$c_{M3} = 1.0385 \cdot 10^{-8} \frac{\text{meV}}{\mu_N^2 \text{b}^2}$$

$$c_{E4} = 1.1166183 \cdot 10^{-8} \frac{\text{meV}}{e^2 \text{b}^4}$$

Quite often transition strengths are expressed in Weisskopf units (W.u.). Those are a measure how many nucleons take part in a transition. The transformation can be done with the following table:

$$B(E1; I_i \rightarrow I_f) = 6.446 \cdot 10^{-4} A^{\frac{2}{3}} e^2 \text{b}$$

$$B(E2; I_i \rightarrow I_f) = 5.940 \cdot 10^{-6} A^{\frac{4}{3}} e^2 \text{b}^2$$

$$B(E3; I_i \rightarrow I_f) = 5.940 \cdot 10^{-8} A^2 e^2 \text{b}^3$$

$$B(E4; I_i \rightarrow I_f) = 6.285 \cdot 10^{-10} A^{\frac{8}{3}} e^2 \text{b}^4$$

$$B(M1; I_i \rightarrow I_f) = 1.790 \mu_N^2$$

The experiments presented in this work deal with the $2_1^+ \rightarrow 0_1^+$ transition and the quadrupole moment of the 2_1^+ state. The formalism for that results in the following set of equations:

$$\frac{1}{\tau} = 8.1 \cdot 10^{13} \left(\frac{E_\gamma}{\text{keV}} \right)^5 B(E2; 2_1^+ \rightarrow 0_1^+) \cdot (1 + \alpha) \quad (\text{D.4})$$

$$B(E2; 2_1^+ \rightarrow 0_1^+) = \frac{1}{5} |\langle 0_1^+ || E2 || 2_1^+ \rangle|^2 \quad (\text{D.5})$$

$$B(E2; 0_1^+ \rightarrow 2_1^+) = |\langle 2_1^+ || E2 || 0_1^+ \rangle|^2 = 5 \cdot B(E2; 2_1^+ \rightarrow 0_1^+) \quad (\text{D.6})$$

$$M_{20} = \langle 0_1^+ || E2 || 2_1^+ \rangle = M_{02} = \langle 2_1^+ || E2 || 0_1^+ \rangle = \sqrt{B(E2; 0_1^+ \rightarrow 2_1^+)} \quad (\text{D.7})$$

Assuming a rigid, quadrupole-deformed, axially-symmetric rotor with transitional, intrinsic quadrupole moment Q_0 one can write

$$M_{20} = \sqrt{\frac{5}{16\pi}} Q_0, \quad (\text{D.8})$$

$$M_{22} = \pm \sqrt{\frac{10}{7}} M_{20}, \quad (\text{D.9})$$

where $-$ indicates a prolate and $+$ an oblate rotor.

The spectroscopic quadrupole moment Q is derived from the diagonal matrix element:

$$M_{22} = 1.319Q \quad (\text{D.10})$$

$$Q = -\frac{2}{7} Q_0 \quad (\text{D.11})$$

Bibliography

- [AF79] T. K. Alexander and J. S. Foster. “Lifetime Measurements of excited nuclear Levels by Doppler-shift Methods”. In: *Nuclear Physics A* 10.1 (1979), pp. 197–331.
- [Ago03] S. Agostinelli et al. “Geant4 - a simulation toolkit”. In: *Nuclear Instruments and Methods in Physics Research Section A: Accelerators, Spectrometers, Detectors and Associated Equipment* 506.3 (2003), pp. 250–303.
- [Ahn09] T. Ahn et al. “Evolution of the one-phonon mixed-symmetry state in isotones as a local measure for the proton-neutron quadrupole interaction”. In: *Physics Letters B* 679.1 (2009), pp. 19–24.
- [AIP03] F. Andreozzi, N. Lo Iudice, and A. Porrino. “An importance sampling algorithm for generating exact eigenstates of the nuclear Hamiltonian”. In: *J. of Phys. G: Nucl. Part. Phys.* 29.10 (2003), p. 2319.
- [Akk12] S. Akkoyun et al. “AGATA - Advanced GAMMA Tracking Array”. In: *Nuclear Instruments and Methods in Physics Research Section A: Accelerators, Spectrometers, Detectors and Associated Equipment* 668.0 (2012), pp. 26–58.
- [Ald56] K. Alder et al. “Study of Nuclear Structure by Electromagnetic Excitation with Accelerated Ions”. In: *Rev. Mod. Phys.* 28 (4 Oct. 1956), pp. 432–542.
- [AW66] K. Alder and A. Winther. *Coulomb excitation: a collection of reprints*. Perspectives in physics. Academic Press, 1966.
- [AW75] K. Alder and A. Winther. *Electromagnetic excitation: theory of Coulomb excitation with heavy ions*. North-Holland Pub. Co., 1975.
- [BB30] W. Bothe and H. Becker. “Künstliche Erregung von Kern- γ -Strahlen”. German. In: *Zeitschrift für Physik* 66 (5-6 1930), pp. 289–306.
- [BDH84] M. J. Bechara, O. Dietzsch, and J. H. Hirata. “Quadrupole moment of the first 2^+ excited state in ^{136}Ba through the reorientation effect”. In: *Phys. Rev. C* 29 (5 May 1984), pp. 1672–1677.

-
- [BHR03] M. Bender, P.-H. Heenen, and P.-G. Reinhard. “Self-consistent mean-field models for nuclear structure”. In: *Rev. Mod. Phys.* 75 (1 Jan. 2003), pp. 121–180.
- [Bia11] D. Bianco et al. “Matrix diagonalization algorithm and its applicability to the nuclear shell model”. In: *Phys. Rev. C* 84 (2 Aug. 2011), p. 024310.
- [Bia12] D. Bianco et al. “Importance-sampling diagonalization algorithm for large-scale shell model calculations on $N = 80$ isotones”. In: *Phys. Rev. C* 85 (3 Mar. 2012), p. 034332.
- [BM69] A. Bohr and B.R. Mottelson. *Nuclear Structure: Nuclear deformations*. Nuclear Structure. W. A. Benjamin, 1969.
- [BN96] P. A. Butler and W. Nazarewicz. “Intrinsic reflection asymmetry in atomic nuclei”. In: *Rev. Mod. Phys.* 68 (2 Apr. 1996), pp. 349–421.
- [Boe65] J. de Boer et al. “Reorientation Effect in ^{114}Cd ”. In: *Phys. Rev. Lett.* 14 (14 Apr. 1965), pp. 564–567.
- [BR97] Rene Brun and Fons Rademakers. “ROOT - An object oriented data analysis framework”. In: *Nuclear Instruments and Methods in Physics Research Section A: Accelerators, Spectrometers, Detectors and Associated Equipment* 389 (1997), pp. 81–86.
- [Bre77] R. Brenn et al. “Nuclear deorientation for heavy ions recoiling in vacuum and low pressure gas”. English. In: *Zeitschrift für Physik A Atoms and Nuclei* 281.3 (1977), pp. 219–227.
- [BS77] F. Bosch and H. Spehl. “Asymptotic attenuation coefficients in random perturbations of Angular Correlations”. English. In: *Zeitschrift für Physik A Atoms and Nuclei* 280.4 (1977), pp. 329–339.
- [Bur85] S.M. Burnett et al. “A measurement of $B(E3; 0^+ \rightarrow 3_1^-)$ and some E2 transition probabilities in $^{132,134,136,138}\text{Ba}$ using Coulomb excitation”. In: *Nuclear Physics A* 432.2 (1985), pp. 514–524.
- [Bur89] S.M. Burnett et al. “Electric quadrupole moments of the first excited states of $^{130,134,138}\text{Ba}$ ”. In: *Nuclear Physics A* 494.1 (1989), pp. 102–122.
- [Cas00] R. Casten. *Nuclear Structure from a Simple Perspective*. Oxford Studies in Nuclear Physics. Oxford University Press, 2000.
- [CCW83] T. Czosnyka, D. Cline, and C. Wu. “GOSIA, A Semiclassical Coulomb-Excitation Least-Squares Search Code”. In: *Bull. Am. Phys. Soc.* 28 (1983), p. 745.

-
- [Cli12] D. Cline et al. *Gosia user manual for simulation and analysis of Coulomb excitation experiments*. 2012.
- [CT90] B. Castel and I.S. Towner. *Modern theories of nuclear moments*. Oxford studies in nuclear physics. Clarendon Press, 1990.
- [CZ96] R. F. Casten and N. V. Zamfir. “The evolution of nuclear structure: the $N_p N_n$ scheme and related correlations”. In: *Journal of Physics G: Nuclear and Particle Physics* 22.11 (1996), p. 1521.
- [Dan11] M. Danchev et al. “One-phonon isovector $2_{1,MS}^+$ state in the neutron-rich nucleus ^{132}Te ”. In: *Phys. Rev. C* 84 (6 Dec. 2011), p. 061306.
- [Dar90] D. Darquennes et al. “Production of intense radioactive ion beams using two accelerators”. In: *Phys. Rev. C* 42 (3 1990), R804–R806.
- [Del99] M.A. Deleplanque et al. “GRETA: utilizing new concepts in γ -ray detection”. In: *Nuclear Instruments and Methods in Physics Research Section A: Accelerators, Spectrometers, Detectors and Associated Equipment* 430 (1999), pp. 292–310.
- [DG80] J. Dechargé and D. Gogny. “Hartree-Fock-Bogolyubov calculations with the $D1$ effective interaction on spherical nuclei”. In: *Phys. Rev. C* 21 (4 Apr. 1980), pp. 1568–1593.
- [EG70] J.M. Eisenberg and W. Greiner. *Nuclear models: collective and single-particle phenomena*. Nuclear Theory Bd. 1-2. North-Holland, 1970.
- [EJB99] L. Esser, R.V. Jolos, and P. von Brentano. “Shell model calculations for ^{146}Gd and ^{147}Tb ”. In: *Nuclear Physics A* 650.2 (1999), pp. 157–175.
- [Eks09] A. Ekström et al. “Electric quadrupole moments of the 2_1^+ states in $^{100,102,104}\text{Cd}$ ”. In: *Phys. Rev. C* 80 (5 Nov. 2009), p. 054302.
- [Ens] *Evaluated Nuclear Structure Data File*. URL: <http://www.nndc.bnl.gov/ensdf/>.
- [ER04] J. L. Egido and L. M. Robledo. “Angular Momentum Projection and Quadrupole Correlations Effects in Atomic Nuclei”. In: *Extended Density Functionals in Nuclear Structure Physics*. Ed. by G. A. Lalazissis, P. Ring, and D. Vretenar. Vol. 641. Lecture Notes in Physics, Berlin Springer Verlag. 2004, pp. 269–302. eprint: arXiv:nucl-th/0311106.
- [ER90] J.L. Egido and L.M. Robledo. “A self-consistent approach to the ground state and lowest-lying negative-parity state in the barium isotopes”. In: *Nuclear Physics A* 518.3 (1990), pp. 475–495.

-
- [Fed08] V.N. Fedosseev et al. “ISOLDE RILIS: New beams, new facilities”. In: *Nuclear Instruments and Methods in Physics Research Section B: Beam Interactions with Materials and Atoms* 266 (2008), pp. 4378–4382.
- [Fer34] E. Fermi. “Versuch einer Theorie der β -Strahlen. I”. German. In: *Zeitschrift für Physik* 88 (3-4 1934), pp. 161–177.
- [G4m] *Physics Reference Manual, Version: geant4.9.4*. URL: <http://geant4.web.cern.ch/geant4/support/userdocuments.shtml>.
- [Gla10] K. A. Gladnishki et al. “Search for one-phonon mixed-symmetry states in the radioactive nucleus ^{140}Nd ”. In: *Phys. Rev. C* 82 (3 Sept. 2010), p. 037302.
- [Hay] Adam Hayes. *Gosia Forum*. URL: http://www-user.pas.rochester.edu/~gosia/mediawiki/index.php/Error_estimation.
- [Hei32a] W. Heisenberg. “Über den Bau der Atomkerne. I”. German. In: *Zeitschrift für Physik* 77 (1-2 1932), pp. 1–11.
- [Hei32b] W. Heisenberg. “Über den Bau der Atomkerne. II”. German. In: *Zeitschrift für Physik* 78 (3-4 1932), pp. 156–164.
- [Hei33] W. Heisenberg. “Über den Bau der Atomkerne. III”. German. In: *Zeitschrift für Physik* 80 (9-10 1933), pp. 587–596.
- [HL80] R.G. Helmer and M.A. Lee. “Analytical functions for fitting peaks from Ge semiconductor detectors”. In: *Nuclear Instruments and Methods* 178 (1980), pp. 499–512.
- [HMO95] M. Honma, T. Mizusaki, and T. Otsuka. “Diagonalization of Hamiltonians for Many-Body Systems by Auxiliary Field Quantum Monte Carlo Technique”. In: *Phys. Rev. Lett.* 75 (7 Aug. 1995), pp. 1284–1287.
- [Hur07] A. M. Hurst et al. “Measurement of the Sign of the Spectroscopic Quadrupole Moment for the 2_1^+ State in ^{70}Se : No Evidence for Oblate Shape”. In: *Phys. Rev. Lett.* 98 (7 Feb. 2007), p. 072501.
- [IA06] F. Iachello and A. Arima. *The Interacting Boson Model*. Cambridge Monographs on Mathematical Physics. Cambridge University Press, 2006.
- [Iac84] F. Iachello. “New Class of Low-Lying Collective Modes in Nuclei”. In: *Phys. Rev. Lett.* 53 (15 Oct. 1984), pp. 1427–1429.
- [Icra] “ICRU Report 49”. In: *Journal of the ICRU* (1993).

-
- [Icrb] “ICRU Report 73: Stopping of ions heavier than Helium”. In: *Journal of the ICRU* (2005). eprint: <http://jicru.oxfordjournals.org/content/5/1/0.full.pdf+html>.
- [IRW74] N. Lo Iudice, D.J. Rowe, and S.S.M. Wong. ““Exact” shell model calculations in $A = 17$ and $A = 18$ nuclei and effective operators in the $(2s, 1d)$ shell”. In: *Nucl. Phys. A* 219.1 (1974), pp. 171–189.
- [Iso] *ISOLDE webpage*. URL: <http://isolde.web.cern.ch/ISOLDE/>.
- [Iud12] N. Lo Iudice et al. “Low-energy nuclear spectroscopy in a microscopic multiphonon approach”. In: *Journal of Physics G: Nuclear and Particle Physics* 39.4 (2012), p. 043101.
- [Jak02] G. Jakob et al. “Evidence for proton excitations in $^{130,132,134,136}\text{Xe}$ isotopes from measurements of g factors of 2_1^+ and 4_1^+ states”. In: *Phys. Rev. C* 65 (2 Jan. 2002), p. 024316.
- [JB96] R.V. Jolos and P. von Brentano. “The absolute value of the static quadrupole moment $Q(2_1^+)$ expressed by $B(E2)$ values”. In: *Physics Letters B* 381 (1996), pp. 7–11.
- [Kes03] O. Kester et al. “Accelerated radioactive beams from REX-ISOLDE”. In: *Nuclear Instruments and Methods in Physics Research Section B: Beam Interactions with Materials and Atoms* 204.0 (2003), pp. 20–30.
- [KH87] K.S. Krane and D. Halliday. *Introductory nuclear physics*. Wiley, 1987.
- [KS72] J. R. Kerns and J. X. Saladin. “Reorientation Effect Measurements on $^{134,136,138}\text{Ba}$ ”. In: *Physical Review C* 6.3 (1972), pp. 1016–1023.
- [Lar72] R.D. Larsen et al. “The sign of the multiple Coulomb excitation interference term and the static quadrupole moment of the first 2^+ state of ^{114}Cd ”. In: *Nuclear Physics A* 195.1 (1972), pp. 119–128.
- [Lau] T. Lauritsen. *Gammasphere webpage*. URL: <http://www.phy.anl.gov/gammasphere/doc/index.html> (visited on 06/21/2012).
- [Lee90] I-Yang Lee. “The GAMMASPHERE”. In: *Nuclear Physics A* 520.0 (1990), pp. 641–655.
- [LIST08] N. Lo Iudice, Ch. Stoyanov, and D. Tarpanov. “Fine structure of proton-neutron mixed symmetry states in some $N = 80$ isotones”. In: *Phys. Rev. C* 77 (4 Apr. 2008), p. 044310.
- [LIST11] N. Lo Iudice, Ch. Stoyanov, and D. Tarpanov. “ $E2$ transitions in Sn isotopes within the quasiparticle-phonon model”. In: *Phys. Rev. C* 84 (4 Oct. 2011), p. 044314.

-
- [Lju08] J. Ljungvall et al. “Shape Coexistence in Light Se Isotopes: Evidence for Oblate Shapes”. In: *Phys. Rev. Lett.* 100 (10 Mar. 2008), p. 102502.
- [LLZ97] L.D. Landau, E.M. Lifschitz, and P. Ziesche. *Mechanik*. Lehrbuch der theoretischen Physik. Deutsch Harri GmbH, 1997.
- [LRV04] G.A. Lalazissis, P. Ring, and D. Vretenar. *Extended Density Functionals in Nuclear Structure Physics*. Lecture Notes in Physics. Springer, 2004.
- [MGM89] H. Mach, R.L. Gill, and M. Moszynski. “A method for picosecond lifetime measurements for neutron-rich nuclei: (1) Outline of the method”. In: *Nuclear Instruments and Methods in Physics Research Section A: Accelerators, Spectrometers, Detectors and Associated Equipment* 280.1 (1989), pp. 49–72.
- [MJ55] M.G. Mayer and J.H.D. Jensen. *Elementary theory of nuclear shell structure*. Structure of matter series. Wiley, 1955.
- [MR94] V. Martín and L. M. Robledo. “Theoretical description of octupole correlations in the $^{138-148}\text{Xe}$ nuclei”. In: *Phys. Rev. C* 49 (1 Jan. 1994), pp. 188–193.
- [Möl13] T. Möller. “Systematics of MSS around $A=130$ ”. to be finished in 2013. PhD thesis. TU Darmstadt, 2013.
- [Mün90] W.D. Myers, M. Nitschke, and E.B. Norman, eds. *Proceedings of the First International Conference on Radioactive Nuclear Beams: 16-18 October 1989, University of California at Berkeley, Lawrence Berkeley Laboratory, Berkeley, California*. Proceedings of the international conference on radioactive nuclear beams. World Scientific, 1990.
- [Nei74] M. Neiman et al. “Measurement of the quadrupole moments of the first 2^+ states of ^{130}Ba and ^{134}Ba ”. In: *Physics Letters B* 52.2 (1974), pp. 189–191.
- [Ney03] G. Neyens. “Nuclear magnetic and quadrupole moments for nuclear structure research on exotic nuclei”. In: *Reports on Progress in Physics* 66.4 (2003), p. 633.
- [Ost02] A.N Ostrowski et al. “CD: A double sided silicon strip detector for radioactive nuclear beam experiments”. In: *Nuclear Instruments and Methods in Physics Research Section A: Accelerators, Spectrometers, Detectors and Associated Equipment* 480 (2002), pp. 448–455.
- [Ots01a] T. Otsuka. “Monte Carlo shell model”. In: *Nuclear Physics A* 693 (2001), pp. 383–393.

-
- [Ots01b] T. Otsuka et al. “Monte Carlo shell model for atomic nuclei”. In: *Progress in Particle and Nuclear Physics* 47.1 (2001), pp. 319–400.
- [Owe80] H. Ower. *User manual for computer code CLX and DCY*. 1980.
- [Par76] P. Paradis et al. “Measurement of the static quadrupole moments of the first 2^+ states in ^{94}Mo , ^{96}Mo , ^{98}Mo , and ^{100}Mo ”. In: *Phys. Rev. C* 14 (3 Sept. 1976), pp. 835–841.
- [PBL08] N. Pietralla, P. von Brentano, and A.F. Lisetskiy. “Experiments on multiphonon states with proton-neutron mixed symmetry in vibrational nuclei”. In: *Progress in Particle and Nuclear Physics* 60.1 (2008), pp. 225–282.
- [PG04] N. Pietralla and O. M. Gorbachenko. “Evolution of the β excitation in axially symmetric transitional nuclei”. In: *Phys. Rev. C* 70 (1 2004), p. 011304.
- [Phi86] W. R. Phillips et al. “Octupole deformation in neutron-rich barium isotopes”. In: *Phys. Rev. Lett.* 57 (26 Dec. 1986), pp. 3257–3260.
- [Pie98] N. Pietralla et al. “Isovector quadrupole excitations in the valence shell of the vibrator nucleus ^{136}Ba : Evidence from photon scattering experiments”. In: *Phys. Rev. C* 58 (2 Aug. 1998), pp. 796–800.
- [Rad02] D. C. Radford et al. “Coulomb Excitation of Radioactive $^{132,134,136}\text{Te}$ Beams and the Low $B(E2)$ of ^{136}Te ”. In: *Phys. Rev. Lett.* 88 (22 May 2002), p. 222501.
- [Rai06] G. Rainovski et al. “Stabilization of Nuclear Isovector Valence-Shell Excitations”. In: *Phys. Rev. Lett.* 96 (12 Mar. 2006), p. 122501.
- [RE10] T.R. Rodríguez and J.L. Egido. “Triaxial angular momentum projection and configuration mixing calculations with the Gogny force”. In: *Phys. Rev. C* 81 (6 June 2010), p. 064323.
- [RJT01] S. Raman, C.W. Nestor JR., and P. Tikkanen. “Transition probability from the ground to the first-excited 2^+ state of even-even nuclides”. In: *Atomic Data and Nuclear Data Tables* 78.1 (2001), pp. 1–128.
- [Rob10] L. M. Robledo et al. “Octupole deformation properties of the Barcelona-Catania-Paris energy density functionals”. In: *Phys. Rev. C* 81 (3 Mar. 2010), p. 034315.
- [Rod11] T.R. Rodríguez. “Energy density functional calculations”. private communication. 2011.

-
- [Row10] D.J. Rowe. *Nuclear Collective Motion: Models and Theory*. World Scientific, 2010.
- [RS05] P Ring and P Schuck. *The Nuclear Many-Body Problem*. Texts and Monographs in Physics. Springer, 2005.
- [Sav] G. Savard. *ATLAS webpage*. URL: <http://www.phy.anl.gov/atlas/index.html> (visited on 06/21/2012).
- [Shi01] N. Shimizu et al. “Transition from Spherical to Deformed Shapes of Nuclei in the Monte Carlo Shell Model”. In: *Phys. Rev. Lett.* 86 (7 Feb. 2001), pp. 1171–1174.
- [Sie09] K. Sieja et al. “Description of proton-neutron mixed-symmetry states near ^{132}Sn within a realistic large scale shell model”. In: *Phys. Rev. C* 80 (5 Nov. 2009), p. 054311.
- [Sim67] J.J. Simpson et al. “A determination of quadrupole moments in ^{114}Cd , ^{130}Ba , ^{148}Sm and ^{150}Sm ”. In: *Nuclear Physics A* 94.1 (1967), pp. 177–191.
- [Sin01] B. Singh. “Nuclear Data Sheets for $A = 130$ ”. In: *Nuclear Data Sheets* 93.1 (2001), pp. 33–242.
- [Sol92] V.G. Solov’ev. *Theory of Atomic Nuclei: Quasiparticles and Phonons*. Inst. of Physics Publ., 1992.
- [Sta11] C. Stahl. “Continuous-Angle DSAM: A new quality of lifetime measurements”. MA thesis. TU Darmstadt, 2011.
- [Sta13] C. Stahl. “Software package APCAD”. to be published. PhD thesis. TU Darmstadt, 2013.
- [Ste11] R. Stegmann. “Investigation of the first 2^+ state and its deformation in radioactive ^{142}Ba by Coulomb excitation”. BA thesis. TU Darmstadt, 2011.
- [Ste12] R. Stegmann. “Investigation of the 2_1^+ state in radioactive ^{142}Sm by Coulomb excitation”. MA thesis proposal. TU Darmstadt, Dec. 2012.
- [Sto12] Ch. Stoyanov. “QPM calculations for ^{140}Nd ”. private communication. 2012.
- [Stu00] O. Stuch et al. “Coincidence recoil-distance Doppler-shift lifetime measurements in $^{129,130}\text{Ba}$ with EUROBALL Ge cluster detectors”. In: *Phys. Rev. C* 61 (4 2000), p. 044325.
- [SV88] S. Salém-Vasconcelos et al. “Quadrupole moment of the first 2^+ excited state in ^{64}Zn ”. In: *Phys. Rev. C* 38 (5 Nov. 1988), pp. 2439–2442.

-
- [Tal93] I.T. Talmi. *Simple Models of Complex Nuclei: The Shell Model and Interacting Boson Model*. Contemporary Concepts in Physics Series. Taylor & Francis Group, 1993.
- [Ter02] J. Terasaki et al. “Anomalous behavior of 2^+ excitations around ^{132}Sn ”. In: *Phys. Rev. C* 66 (5 Nov. 2002), p. 054313.
- [Tow73] C.W. Towsley et al. “Measurements of the shapes of $^{130,134,136}\text{Ba}$ ”. In: *Proceedings of the International Conference on Nuclear Moments and Nuclear Structure, Journ. of the Physics Society of Japan* 34 (1973), p. 442.
- [WJ91] J. C. Wells and N. R. Johnson. *LINESHAPE: A Computer Program for Doppler-Broadened Lineshape Analysis*. Tech. rep. ORNL Physics Division Progress Report for Period Ending September 30, 1991.
- [YUK35] Hideki YUKAWA. “On the Interaction of Elementary Particles. I”. In: *Proceedings of the Physico-Mathematical Society of Japan. 3rd Series* 17 (1935), pp. 48–57.
- [Zdu07] H. Zduńczuk et al. “Angular momentum projection of cranked Hartree-Fock states: Application to terminating bands in $A=44$ nuclei”. In: *Phys. Rev. C* 76 (4 Oct. 2007), p. 044304.
- [Zie11] Magdalena Zielinska. “Coulex evaluation of ^{96}Mo ”. private communication. 2011.



List of publications

- [Alb12] M. Albers et al. “Evidence for a Smooth Onset of Deformation in the Neutron-Rich Kr Isotopes”. In: *Phys. Rev. Lett.* 108 (6 Feb. 2012), p. 062701.
- [Alb13] M. Albers et al. “Shape dynamics in neutron-rich Kr isotopes: Coulomb excitation of ^{92}Kr , ^{94}Kr and ^{96}Kr ”. In: *Nuclear Physics A* 899.0 (2013), pp. 1–28.
- [Bau07] C. Bauer. “Anwendung der "Recoil-in-Vacuum"-Methode zur Berechnung der g-Faktoren von Kernen in der Massenregion um $A=130$ ”. BA thesis. TU Darmstadt, 2007.
- [Bau09a] C. Bauer. “Der g-Faktor im Radionuklid ^{140}Ba - Erste Anwendung der "Recoil-in-Vacuum" Technik an REX-ISOLDE”. MA thesis. TU Darmstadt, 2009.
- [Bau09b] C. Bauer et al. “REX-ISOLDE Facility and the Importance of Beam Time Structure to Data Acquisition and Processing—the Experimentalist’s View”. In: *Proc. of PAC. REX-ISOLDE and MINIBALL collaborations.* 2009.
- [Bau12a] C. Bauer et al. “Level lifetimes and quadrupole moments from Coulomb excitation in the Ba chain and the $N = 80$ isotones”. In: *EPJ Web of Conferences* 38 (Dec. 2012), p. 10003.
- [Bau12b] C. Bauer et al. “Prolate shape of ^{140}Ba from a first combined Doppler-shift and Coulomb-excitation measurement at the REX-ISOLDE facility”. In: *Phys. Rev. C* 86 (3 Sept. 2012), p. 034310.
- [Bau13] C. Bauer. “Local suppression of collectivity in the $N=80$ isotones at the $Z=58$ subshell closure”. submitted to *Phys. Rev. C.* 2013.
- [Ber09] Z. Berant et al. “g factor of the 2_1^+ state of ^{172}Hf ”. In: *Phys. Rev. C* 80 (5 Nov. 2009), p. 057303.
- [Coo12] N. Cooper et al. “Photoresponse of ^{76}Se below 9 MeV”. In: *Phys. Rev. C* 86 (3 Sept. 2012), p. 034313.
- [Gaf13] L. P. Gaffney et al. “Studies of pear-shaped nuclei using accelerated radioactive beams”. In: *Nature* 497.7448 (May 2013), pp. 199–204.

-
- [Mos10] K. Moschner et al. “New measurement of the $^{68}\text{Zn}(4_1^+)$ g factor combined with a reanalysis of previous data”. In: *Phys. Rev. C* 82 (1 July 2010), p. 014301.
- [Möll12] T. Möller et al. “Absolute β -to-ground band transition strengths in ^{154}Sm ”. In: *Phys. Rev. C* 86 (3 Sept. 2012), p. 031305.
- [Pie10] N. Pietralla et al. “Symmetries of Quadrupole-Collective Vibrational Motion in Transitional Even-Even 124-134 Xenon Nuclei”. In: *Proceedings of the 12th International Conference on Nuclear Reaction Mechanisms* (2010).
- [Rai10] G. Rainovski et al. “Experimental studies of proton-neutron mixed symmetry states in the mass $A \approx 130$ region”. In: *Journal of Physics: Conference Series* 205.1 (2010), p. 012039.
- [War13] N. Warr et al. “The Miniball spectrometer”. English. In: *The European Physical Journal A* 49.3 (2013), pp. 1–32.

List of symbols

A_1	mass number of the projectile
A_2	mass number of the target nucleus
a_{if}	excitation amplitude $i \rightarrow f$
β	velocity as fraction of c
β_λ	deformation with multipole order λ
c	speed of light in vacuum
E	beam energy (laboratory system)
η	Sommerfeld parameter
G_k	attenuation coefficient due to the deorientation effect
M_{if}	reduced matrix element connecting state i and f
ϕ_1	azimuthal scattering angle of the projectile (laboratory system)
ϕ_2	azimuthal scattering angle of the target nucleus (laboratory system)
ϕ_γ	azimuthal angle of emitted γ (laboratory system)
P_{if}	excitation probability
Q	spectroscopic quadrupole moment
Q_0	intrinsic quadrupole moment
Q_k	attenuation coefficient due to finite detector size
σ^P	cross-section for projectile excitation
σ^T	cross-section for target excitation
ϑ	polar scattering angle (center-of-mass system)
θ_1	polar scattering angle of the projectile (laboratory system)
θ_2	polar scattering of the target nucleus (laboratory system)
θ_γ	polar angle of emitted γ (laboratory system)

ξ	adiabaticity parameter
Z_1	charge number of the projectile
Z_2	charge number of the target nucleus

Acronyms

APCAD	Analysis Program for Continuous Angle DSAM
CBS	confined β -soft
CMS	center-of-mass system
Coulex	Coulomb excitation
DSAM	Doppler-shift attenuation method
EDF	energy density functionals
IBM	interacting boson model
LAB	laboratory system
MCSM	Monte Carlo Shell Model
MSSs	mixed-symmetry states
QMCD	Quantum Monte Carlo Diagonalization
QPM	quasiparticle-phonon model
RDDS	Recoil-distance Doppler-shift
RPA	random-phase approximation
SCMF	self-consistent mean-field
SMMC	Shell Model Monte Carlo



List of Figures

1.1. Chart of the nuclides	7
1.2. Part of the chart of the nuclides	9
2.1. Nuclear deformation from prolate to oblate	13
2.2. Schematic vibrational level scheme	17
2.3. Schematic rotational level scheme	18
3.1. Nuclear shell model	22
3.2. Hamiltonian matrices in the Monte Carlo shell model	25
4.1. Coulomb excitation process	35
4.2. Coulomb excitation mechanisms in a 3-state system	40
4.3. Dependence of the Coulex cross-section	41
4.4. Illustration of the DSAM principle	50
5.1. Floorplan of the ATLAS accelerator complex	55
5.2. Gammasphere array	56
5.3. Gammasphere target chamber	57
5.4. Beam infrastructure of the ISOLDE facility	58
5.5. ISOLDE surface ion source	60
5.6. RILIS ion source	61
5.7. Overview of the complete REX-ISOLDE setup	62
5.8. MINIBALL array from the top	64
5.9. MINIBALL target chamber	65
6.1. Energy dependence of projectile/target nuclei on scattering angle θ .	71
6.2. Kinematics of $^{142}\text{Sm} \rightarrow ^{94}\text{Mo}$	72
6.3. Efficiency curve of Gammasphere	75
6.4. Efficiency curve of MINIBALL	76
6.5. Interference term	80
6.6. Influence of interference term and quadrupole moment	81
6.7. Velocity distribution of the ^{130}Ba ions	83
6.8. DSAM fit $2_2^+ \rightarrow 0_1^+$ at 908 keV in ^{130}Ba	84

6.9. γ -ray spectra for ^{130}Ba	85
6.10. γ -ray spectra for ^{132}Ba	86
6.11. Target after ^{132}Ba experiment	86
6.12. DSSD for ^{132}Ba experiment	87
6.13. Level schemes of $^{130,132}\text{Ba}$	90
6.14. χ^2 surface for $^{130,132}\text{Ba}$	91
6.15. Stopped transition in ^{140}Ba for detector response	94
6.16. DSAM fit $2_1^+ \rightarrow 0_1^+$ at 602 keV in ^{140}Ba	95
6.17. γ -ray spectra for ^{140}Ba	96
6.18. γ -ray spectra for ^{142}Ba	97
6.19. DSSD for ^{142}Ba experiment	97
6.20. Differential Coulex cross-sections and sensitivity on Q	99
6.21. Maximum-Likelihood analysis for ^{140}Ba	100
6.22. Maximum-Likelihood analysis for ^{142}Ba	101
6.23. γ -ray spectra for ^{140}Nd	104
6.24. γ -ray spectra for ^{140}Nd	105
6.25. χ^2 surface for ^{140}Nd	107
6.26. γ -ray spectra for ^{142}Sm	109
7.1. Systematics in the Barium isotopic chain	115
7.2. Theoretical and experimental energy levels of ^{140}Ba	117
7.3. Distribution of probability in the triaxial (β_2, γ) for ^{140}Ba	117
7.4. Systematics of $B(M1; 2_i^+ \rightarrow 2_1^+)$ strength in N=80 isotones	120
7.5. Level scheme for ^{140}Nd in comparison	121
7.6. Systematics of B(E2) values in the even N=80 isotones	121
7.7. Interpreted systematics of B(E2) values in the even N=80 isotones	123

List of Tables

5.1. Gammasphere detector ring angles θ	55
5.2. List of produced isotopes at the REX-ISOLDE facility	59
5.3. List of conducted experiments	66
6.1. Rings of Gammasphere with detectors during the $^{130,132}\text{Ba}$ runs . . .	82
6.2. Measured yields in the $^{94}\text{Mo}(^{130}\text{Ba}, ^{130}\text{Ba}^*)^{94}\text{Mo}^*$ reaction	88
6.3. Measured yields in the $^{94}\text{Mo}(^{132}\text{Ba}, ^{132}\text{Ba}^*)^{94}\text{Mo}^*$ reaction	89
6.4. Experimental results for $^{130,132}\text{Ba}$	92
6.5. Measured yields in the $^{96}\text{Mo}(^{140}\text{Ba}, ^{140}\text{Ba}^*)^{96}\text{Mo}^*$ reaction	98
6.6. Measured yields in the $^{96}\text{Mo}(^{142}\text{Ba}, ^{142}\text{Ba}^*)^{96}\text{Mo}^*$ reaction	98
6.7. Experimental results for $^{140,142}\text{Ba}$	102
6.8. Measured yields in the $^{48}\text{Ti}(^{140}\text{Nd}, ^{140}\text{Nd}^*)^{48}\text{Ti}^*$ reaction	105
6.9. Measured yields in the $^{64}\text{Zn}(^{140}\text{Nd}, ^{140}\text{Nd}^*)^{64}\text{Zn}^*$ reaction	106
6.10. Experimental results for ^{140}Nd	107
6.11. Measured yields in the $^{48}\text{Ti}(^{142}\text{Sm}, ^{142}\text{Sm}^*)^{48}\text{Ti}^*$ reaction	108
6.12. Measured yields in the $^{94}\text{Mo}(^{142}\text{Sm}, ^{142}\text{Sm}^*)^{94}\text{Mo}^*$ reaction	110
6.13. Experimental results for ^{142}Sm	110
7.1. Experimental results for $^{130,132,140,142}\text{Ba}$	113



Acknowledgments

Beside the various funding agencies that financed the experiments and least not last paid my salary it is a great pleasure for me to acknowledge the help and support of many people during the last years, some of them helping directly related to the thesis, others caring about my well-being on a more private basis, but still creating the atmosphere that made my continuing work on this project possible:

My girlfriend **Anita**, who I will marry this year and to whom this thesis is dedicated to, for just being her.

My mother **Petra**.

My father **Gerhard** and grandfather **Helmut** Bauer, who passed away even before they could see me starting this project.

My brother and sisters **Benedikt**, **Barbara** and **Magdalena**.

Professor Dr. **Norbert Pietralla** for giving me the opportunity to work on the presented topic, and especially for his trust placing so much responsibility upon me by letting me write and defend proposals, give talks etc. on my own.

Dr. **Jörg Leske** and Dr. **Oliver Möller** for teaching me the secrets of Coulomb excitation, correcting my first scientific drafts and being there already during my Bachelor and Master thesis.

My office mates **Thomas Möller** and **Timo Bloch**, beside many fruitful discussions also for introducing me to our common friend Jack. My student **Robert Stegmann** for doing such a nice Bachelor and Master thesis under my supervision as well as the other students **Johannes Wiederhold** and **Udo Gayer**.

The room 35 crew: **Christopher**, **Markus**, **Jacob** and especially **Johann "Yogi" Isaak** for his company in countless Krone table soccer matches.

Last but not least: **Georgi Rainovski** and **Marcus Scheck** for many discussions, correcting my writings, many fights about shell stabilization and their sense of humor.

Experiments of the size presented in this thesis would be impossible without the financial support of various federal agencies. This work has been supported by the BMBF (06DA9041I, 06DA7046, 05P12RDCIB), RII3-EURONS, ENSAR, HIC for FAIR funded by the State of Hesse in the framework of the LOEWE program, the DAAD German-Bulgarian exchange program under Grant Nos. PPP 50751591 and DNTS/01/2/2011, the DFG (Pi393/2-2), and the MINIBALL and ISOLDE collaborations. I also want to gratefully acknowledge the support of all the staff members at ANL and CERN during the experimental runs, and Adam Hayes for his help regarding the Gosia computer code. Special thanks goes to Thorsten Kröll on behalf of the IS411 collaboration for providing the data sets on $^{140,142}\text{Ba}$.

Lebenslauf

Persönliche Daten

Name Christopher Bauer
Mollerstr. 28
64289 Darmstadt
Geb. am 30. Oktober 1983 in Hanau
Ledig, deutsch

Eltern Dr. Gerhard Bauer (†29.05.2009)
Petra Bauer, geb. Raithel

Schulausbildung

1990 - 1994 Friedrich-Ebert-Schule, Klein-Auheim (Grundschule)
1994 - 2003 Franziskanergymnasium Kreuzburg, Großkrotzenburg
Juni 2003 Abitur (Durchschnittsnote: 1,2)

Zivildienst

2003 - 2004 Ökumenische Wohnungslosenhilfe Franziskus-Haus, Hanau

Hochschulstudium

2004 - 2007 TU Darmstadt
B.Sc. Physik (Note: 1,7)
Application of the Recoil-in-Vacuum technique for the calculation of g-factors in the mass region around A=130

2007 - 2009 TU Darmstadt
M.Sc. Physik (Note: 1,0)
The g-factor in radioactive ^{140}Ba - First "Recoil-in-Vacuum" measurement at REX-ISOLDE

seit 2009 TU Darmstadt, Promotionsstudium
Wissenschaftlicher Mitarbeiter



Erklärung zur Dissertation

Hiermit versichere ich, die vorliegende Dissertation ohne Hilfe Dritter nur mit den angegebenen Quellen und Hilfsmitteln angefertigt zu haben. Alle Stellen, die aus Quellen entnommen wurden, sind als solche kenntlich gemacht. Diese Arbeit hat in gleicher oder ähnlicher Form noch keiner Prüfungsbehörde vorgelegen.

Darmstadt, den 17.05.2013

(Christopher Bauer)